JÜLICH Forschungszentrum

BERGISCHE UNIVERSITÄT WUPPERTAL

Horizontal gradients of nitrous oxide in Lagrangian chemical transport induced by ICON-NWP model

Dissertation

zur Erlangung des Grades
Doktor der Naturwissenschaften (Dr. rer. nat.)

von
Jonas Sonnabend

vorgelegt am 19. Februar 2024 an der

Bergischen Universität Wuppertal
Fakultät für Mathematik und Naturwissenschaften
Institut für Atmosphären und Umweltforschung

Abstract

Representing atmospheric transport of constituents accurately in a chemistry climate model is a challenge. This is true in particular for a realistic representation of atmospheric transport barriers, such as those at the edge of the polar vortices or at the tropopause. When transport is represented employing Lagrangian methods, numerical problems representing transport barriers may be obviated. A first implementation of a Lagrangian transport model (the Chemical Lagrangian Model of the Stratosphere, CLaMS) driven by horizontal winds and vertical velocities of the icosahedral nonhydrostatic model (ICON) using the Modular Earth Submodel System (MESSy) is presented in this study. The diabatic heating rates deduced from the temperature tendencies in the (free-running) ICON model allow vertical velocities to be determined and transport calculations in isentropic (diabatic) coordinates. The deduced diabatic heating rates agree qualitatively well with ERA5 reanalysis values in the zonal annual mean, but some discrepancies remain. The chemical transport is analyzed by zonal mean climatologies of nitrous oxide and compared with climatologies obtained from MLS observations. There is an overall agreement between the simulation and N_2O observations by the Microwave Limb Sounder (MLS) satellite instrument. This is especially true for the N_2O gradients at the edge of the polar vortex. The representation of the Antarctic vortex in the model is analyzed by calculations of horizontal gradients in the distribution of nitrous oxide. Overall, the Antarctic vortex and the associated transport barrier at its edge are well represented in the simulation, although the simulated polar vortex is larger than observed. Some differences between the observations and the Lagrangian simulation may be caused by the underlying ICON winds. The coupled ICON/MESSy-CLaMS transport scheme allows tracer distributions in the free troposphere and in the stratosphere to be better simulated than by classical Eulerian schemes.

Publication: An overview of the results of this thesis are submitted and revised (January 3, 2024): Sonnabend, J., Grooß, J.-U., Ploeger, F., Hoffmann, L., Jöckel, P., Kern, B. and Müller, R.: Lagrangian transport based on the winds of the icosahedral nonhydrostatic model (ICON), Metereologische Zeitschrift, PrePub DOI 10.1127/metz/20xx/xxxx

Contents

Chapter 1

Introduction

The climate system consists of four major compartments Ocean, Cryosphere, Biosphere and Atmosphere. Each compartment is subject to gradual changes in the last decades compared to the one hundred year time period from 1850 to 1950. Ocean heat content, glacier mass loss, precipitation and greenhouse gas concentrations are objectives to quantify and document the state of the climate system compartments. The IPCC report 2022 summarizes the connection of each compartment and how the objectives are drastically changing (Fig. 1.1 by *Chen et al.* (2021)). All quantities have an effect on global surface temperature or are affected by it.

Within the past years, many studies of extreme weather events, including hot temperature extremes and heavy precipitation (*Alexander*, 2016; *Fischer and Knutti*, 2016; *Dunn et al.*, 2020; *Di Luca et al.*, 2020) as well as greenhouse gas concentrations (*Prinn et al.*, 2018) contributed to determining the current state of the climate and therefore its impact on life on Earth. These studies include observations (*Hollmann et al.*, 2013; *Bodeker et al.*, 2016), climate models (*Roberts et al.*, 2019; *Wehner et al.*, 2020; *Li et al.*, 2021), and reanalyses (*Hoffmann et al.*, 2019; *Hersbach et al.*, 2020). The IPCC divides the inhabited land mass into various subregions and concludes that hot extremes have been increasing with a high confidence in human contribution. Large parts of Europe and Central Asia have experienced increased heavy precipitation events. Central and West Africa are affected by agricultural and ecological drought (*IPCC*, 2021).

Numerical models can help to understand chemical and physical processes in the climate system compartments and their interactions throughout the individual components. The de-

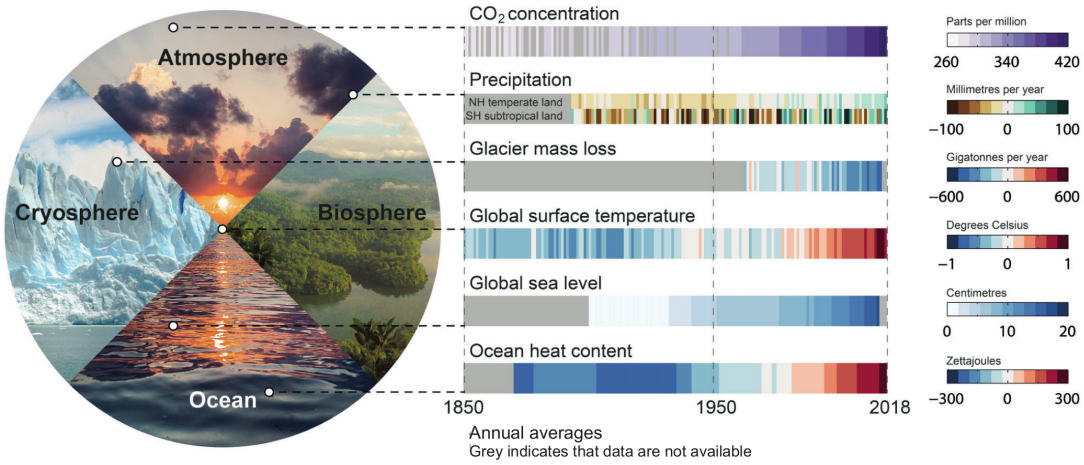

Figure 1.1: Earth system compartments. Objectives and their changes during the time period of 1850 to 2018. Figure by *Chen et al.* (2021).

velopment of climate models is an ongoing process, and many relevant processes have been incorporated into the assessment of climate change (*Le Treut et al.*, 2007). Those numerical models which include all compartments are considered Earth System Models. One of the main objectives of earth system modeling is to improve the understanding of the climate system and therefore the prediction and understanding of changing climate (*Morgenstern et al.*, 2010). Ongoing developments in high-performance computing enables earth system models to include increasingly more complex physical and chemical processes in each compartment. The models can resolve processes on higher resolution and on shorter time scales. An important aspect is the development of highly scalable models and the improvement of established models. The present study focuses on one of the major compartments; the atmosphere. More specifically, on the circulation, chemical distribution of trace gases and the transport processes of the stratosphere.

An important transport process of air masses in the middle atmosphere is the Brewer-Dobson circulation (*Brewer*, 1949; *Dobson*, 1956). The Brewer-Dobson circulation (BDC) is a meridional circulation of air masses with rising motion in the tropics and descent over the polar regions (*Butchart*, 2014). The circulation can be separated into a shallow branch and a deep branch (*Birner and Bönisch*, 2011). Air masses enter the stratosphere in the tropics and are then further uplifted in the leaky tropical pipe (*Plumb*, 1996). In the region of upper troposphere

and lower stratoshpere (UTLS) the shallow branch of the BDC transports air masses polewards to both hemispheres induced by synoptic wave breaking (see Symbol S in Figure 1.2). In the deep branch of the BDC air masses are transported to the middle and upper stratosphere, where vertical advective transport and diffusive transport processes are superimposed (*Plumb*, 2007). The winter hemisphere can be separated into three regions of transport; tropics, mid-latitude surf zone and polar vortex region (cf. Figure 1.2). On the winter hemisphere in the mid latitudes air masses from the tropical stratosphere are transported to high latitudes along a region were dominant planetary wave breaking occurs, see P in Figure 1.2. This wave breaking induces horizontal mixing. The surf zone is embedded at tropical latitudes and extra topics by strong dynamical gradients often named transport barriers (*McIntyre and Palmer*, 1984). Downwelling of air masses to lower stratospheric altitudes is the dominant transport process in the polar vortex region due to strong diabatic descent. In the tropics and polar latitudes strong diabatic transport dominates horizontal mixing processes, while horizontal mixing processes are more dominant in the mid latitude surf zone. Due to the transport barrier between the mid-latitude surf zone and the polar vortex region as well as strong descent of upper stratospheric air into lower stratosphere, air masses of long-lived trace species in the lower and middle stratospheric polar vortex are chemically distinct from mid-latitude air masses.

Chemical composition of the atmosphere is a key climate indicator. Well mixed Greenhouse gases like carbon dioxide (CO_2), methane (CH_4) and nitrous oxide (N_2O) contribute to the Earth radiative warming. The radiative forcing of nitrous oxide is determined to be the third most strongest contributing to Earth radiative budget; the effective radiative forcing in 2019 (relative to the year 1750) for CO_2 was 2.16 Wm^{-2}, for CH_4 was 0.54 Wm^{-2} and for N_2O 0.21 Wm^{-2} (*Arias et al.*, 2021). The global annual mean surface abundance of these species is steadily increasing within the last decades (*Hartmann et al.* (2013); *Gulev et al.* (2021)). The gradual increase for nitrous oxide in the last decades is shown in Figure (1.3).

Nitrous oxide is essentially chemically inert in the troposphere and has no significant sinks at the surface of the earth (*Vogel et al.*, 2023); as a long-lived species, N_2O has a well mixed uniform distribution in the troposphere with decreasing abundance on higher altitudes (*Baldwin*

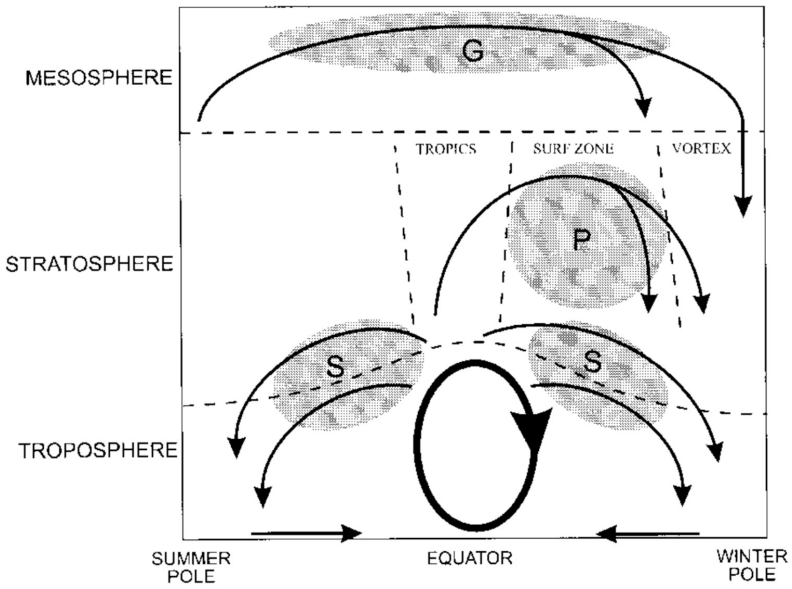

Figure 1.2: Brewer-Dobson circulation. Figure by *Plumb* (2002).

et al., 2019). Atmospheric loss of N_2O occurs in the stratosphere mainly through photolysis. A process of secondary importance for N_2O loss is its reaction with O(1 D) (*Müller*, 2021). Nitrous oxide is the main source of stratospheric reactive nitrogen and thus an important driver of catalytic ozone loss cycles in the stratosphere (*Crutzen*, 1970). Because of the property of N_2O as a tracer of air mass motion N_2O is frequently applied in validation of model transport and transport barriers (*Hoppe et al.*, 2014; *Pommrich et al.*, 2014).

In earlier work *Hoppe et al.* (2014) analyzing long-lived tracers and age of air in the polar vortex regions showed that the Lagrangian transport scheme of the Chemical Lagrangian Model of the Stratosphere (CLaMS) produces a stronger, more realistic transport barrier at the edge of the polar vortex than the classic Eulerian transport scheme of the underlying ECHAM/MESSy Atmospheric Chemistry general circulation model (EMAC). Differences in simulated age of air ranged up to 1 year in the Arctic polar vortex in late winter/early spring and the diabatic vertical velocities, which are used in the Lagrangian transport scheme, showed higher absolute values both in the upwelling branch in the inner tropics and in the downwelling regions in the polar vortices (*Hoppe et al.*, 2014, 2016). More recently, *Charlesworth et al.* (2020) coupled the CLaMS transport to EMAC demonstrating that stratospheric transport barriers are significantly stronger for Lagrangian EMAC-CLaMS transport because of

reduced numerical diffusion; in particular, stronger tracer gradients developed when using CLaMS transport around the polar vortex, at the subtropical jets, and at the edge of the tropical pipe.

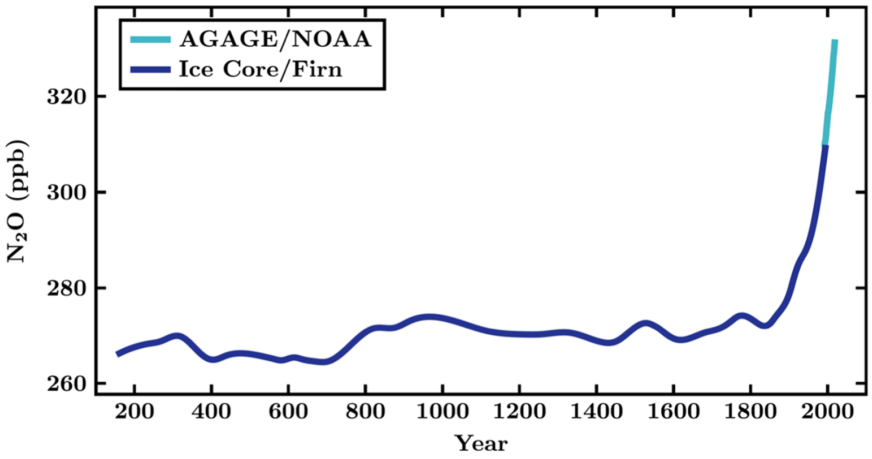

Figure 1.3: Mean abundance of N_2O within the last 2000 years deduced by ice core and firn air measurements. More recent data show global mean data from the atmospheric monitoring networks AGAGE and NOAA. Figure by *Müller* (2021).

The present study is intended as a first step to demonstrate the transport of nitrous oxide in the model development based on the atmospheric circulation of the ICON model using chemical Lagrangian transport models such as CLaMS. In section (2) the model and the simulated setup is described. In section (3) zonal mean climatologies of the meteorology are calculated and compared to climatologies of ERA-Interim Reanalysis. In addition climatologies of nitrous oxide are calculated and compared to climatologies obtained from Microwave Limb Sounder observations. In the following section (4) a statistical perspective describes the separation of mid-latitude from polar region air masses and as a first indication the strength of the transport barrier. In chapter (5) the transport barrier is quantified with zonal monthly mean distribution of nitrous oxide as well as a maximum strength within a short time period of three days.

Chapter 2

Model Description

Describing the physical state and the chemical composition of the atmosphere globally or locally by means of a numerical model requires a multitude of components to be considered. The underlying physical and chemical processes become relevant on different spatial and temporal scales. In the following, the individual components necessary for a chemistry climate model (CCM) (e.g.: *Tilmes et al.* (2016); *Walters et al.* (2014); *Joeckel et al.* (2010)) are presented. A CCM includes a model for the calculation of chemical transport (CTM) (*Chipperfield*, 2006; *McKenna et al*., 2002b) and an underlying atmospheric circulation model (ACM). The general circulation model, in turn, may include the circulation of the ocean. The relevant quantities of Sea Surface Temperature and Sea Ice Content for the atmospheric circulation can be prescribed by analysis data and do not have necessarily to be calculated by a model. In this study the development of a new Chemistry Climate Model is presented. The CCM consists of different individual models presented in this chapter (2). In the following, the individual components of CTM and ACM are presented in detail and how they interact.

2.1 Icosahedral Nonhydrostatic Model (ICON)

The atmospheric motion is simulated by the ICOsahedral Non-hydrostatic model. ICON is a joint development, where the climate projection application is developed at MPI-M Hamburg and the operational numerical weather prediction application is developed at DWD. The physics package including the parametrization for climate projection is referred to ICON-

A (*Giorgetta et al.*, 2018), where the operational numerical weather prediction is referred to ICON-NWP (*Zängl et al.*, 2015). Both models use the same dynamical core, which is designed to provide a numerically accurate, robust, and computationally efficient algorithm to solve the resolved-scale fluid dynamics equations that govern the atmospheric motions (*Wan et al.*, 2013). In this study the ICON-NWP version is used. Hereafter ICON refers to the atmospheric circulation with numerical weather prediction parametrization (ICON-NWP).

The dynamical core is resolved on the underlying grid structure. The state of the atmosphere at a given time step $X_{t+\delta t}$ is calculated by the previous state X_t and applying operators for dynamics, tracer advection and physics. Physics forcing changes the dynamics of the atmospheric state and vice versa. The atmospheric state constitutes the information on meteorology needed for tracer transport. ICON allows governing equations to be used in non-hydrostatic form. Increase in supercomputing performance over the last decades enables spatial resolutions in global circulation models which refrain from the hydrostatic approximation (*Satoh et al.*, 2008).

2.1.1 Grid Structure

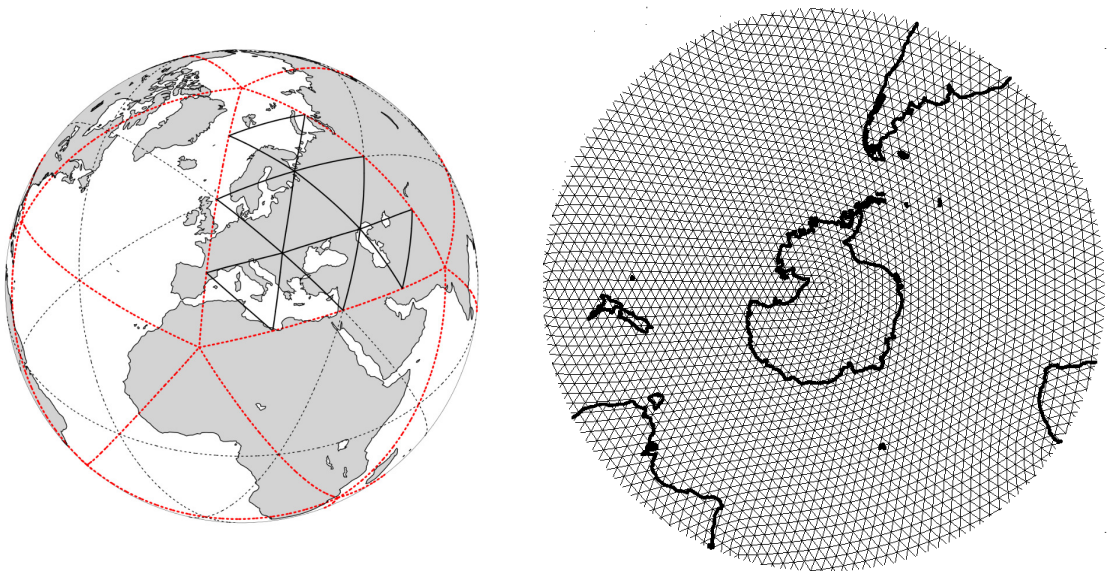

Figure 2.1: ICON grid structure: Left panel: Illustration of R1B0 bisection of a regular icosahedron projected onto the sphere. Right panel: Representation of Antarctic polar region of the ICON R2B4 grid used in the present simulation setup.

The horizontal grid structure of ICON is based on the projection of a regular icosahedron onto the sphere. The basic icosahedron with 20 triangles faces are refined by root division and consecutively by bisection in such a way that the triangles stay equilateral (*Zängl et al.*, 2015). The ICON grid used in this study is defined by the notation R2B4. This grid contains 20480 grid cells and has a horizontal resolution Δx of approximately 158 km (*Giorgetta et al.*, 2018). The discretization of the basic operators on this icosahedral grid is performed with the C-grid staggered discretizations, i.e. the set of dynamical variables are defined in such a way that mass points are in the center of triangular cells, where the normal wind components are perpendicular to the triangular edges (*Giorgetta et al.*, 2018). On staggered grids, the variables of velocity are not located at the mass and temperature points which avoids a spurious mode for the pressure (checkerboard pattern) (*Harlow and Welch*, 1965; *Perić et al.*, 1988; *Rauwoens et al.*, 2007).

The chosen grid structure and discretization scheme are crucial in atmospheric modeling in order to have sufficiently accurate representation of wave propagation (*Thuburn*, 2011). Temporal discretization is explicit two time level predictor-corrector scheme except for vertical wave propagation. For details of the spatial and temporal discretization the reader is referred to *Bonaventura and Ringler* (2005) and on the application with corresponding test cases in ICON to *Wan et al.* (2013) or *Zängl et al.* (2015). The vertical levels are defined according to a generalization of the SLEVE vertical coordinate presented by *Leuenberger et al.* (2010). The SLEVE coordinate is terrain following hybrid sigma height coordinate. The vertical grid structure can be defined by various parameters which are height of the model top, layer thickness of lowermost layer, height above which the coordinate surfaces are flat, decay scale of small and large-scale topography, stretching factor to vary distribution of model levels. The simulations in the present study are performed on a vertical grid with 90 levels; 32 levels in the troposphere and 34 level in the stratosphere and the remaining 24 levels up to the model top of 80 km.

2.1.2 Physics Dynamics Coupling

Physical and dynamical processes which are not resolved in the spatial resolution of the numerical models need to be parameterized. These processes are combined in the physics forcing of the dynamical state of the atmosphere. The implementation of ICON allows to choose between variety of parametrizations within the physics package. This include physical package for numerical weather prediction and ECHAM (*Roeckner et al.*, 2003) physics package for climate simulations. The relevant physical processes in the atmosphere cover a range of time scales. The user can define individual time intervals at which the forcing of certain processes are recalculated and the variables of the dynamics are updated. The distinctive processes are parameterized in the model individually. The numerical stability and conservation properties are influenced by the numerical scheme chosen for coupling and updating the dynamics by physics forcing of all parameterized physical processes (*Williamson*, 2002; *Dubal et al.*, 2004, 2005). In the present study the ICON-NWP physics package is used with the default setup for the physics parameterizations. The convection scheme is used by *Bechtold et al.* (2008), RRTM radiation by *Mlawer et al.* (1997), Subgrid-Scale Orography by *Lott and Miller* (1997) and gravity wave drag surface scheme by *Orr et al.* (2010). Fast physics processes are treated as a combined process and include turbulence, microphysics, surface, saturation and shortwave and longwave heating rates. The described physics packages are developed and evaluated in last decades partly for the operational numerical weather prediction models IFS at ECMWF (*ECMWF*, 2009) and COSMO at DWD (*Doms et al.*, 2011).

2.2 Chemical Lagrangian Model of the Stratosphere (CLaMS)

The Chemical Lagrangian Module of the Stratosphere (CLaMS) describes the composition of the atmosphere as a finite ensemble of air parcels, which are transported according to the atmospheric motions with a fully Lagrangian transport scheme (*McKenna et al.*, 2002b). The transport and chemistry of air parcels in the atmosphere are simulated with a modular chemical transport model (*McKenna et al.*, 2002a; *Grooß et al.*, 2002). The modular structure of CLaMS enables the ensemble of air parcels to be subject of different physical and chemical processes.

The different submodels that constitute CLaMS and their interconnection are described in the following section.

2.2.1 Trajectory calculation

Advective transport is applied to an ensemble of air parcels. For this purpose, the horizontal advection is calculated individually for each air parcel from the Lagrangian point of view using a Runge Kutte scheme (*McKenna et al.*, 2002b). The Lagrangian implementation allows the transport to be calculated without diffusion.

In the integration time step of the CLaMS trajectory module, the horizontal wind field and diabatic heating rates are interpolated onto the positions of the air parcels. There are two ways to run the trajectory calculation in CLaMS. First, the trajectories of the air parcels can be driven by meteorological reanalysis. Reanalysis are data products who provide data sets of meteorological variables generated by a global numerical weather prediction model combined with a data assimilation system of atmospheric observations from the past to present. The advection scheme of CLaMS reads the meteorological variables offline from data files and runs the integration time step afterwards. The trajectory calculation, and advection time step within, is limited to the temporal data resolution of the reanalysis. For the SPARC Reanalysis Intercomparison Project, CLaMS and other Lagrangian transport models, have been used to validate Reanalysis products and determine differences and robust features in the Reanalysis products (*Ploeger et al.*, 2019).

The second method to use the CLaMS trajectory module is by the use of a chemistry climate model. The meteorological variables of the chemistry climate model are provided during the advection time step of the model during online integration. The trajectory advection can be deduced on the same temporal resolution as the chemistry climate model is performed. The Lagrangian transport can calculate the species distribution (one way coupling) (*Hoppe et al.*, 2014) or in addition can be used to calculate the feedback of tracer distribution to the atmospheric circulation (feedback coupling) (*Charlesworth et al.*, 2023).

The velocity calculation for the vertical motion depends on the choice of the vertical coordinate. For the description of transport processes in the stratosphere the choice of ζ as vertical

coordinate within CLaMS has proven to be advantageous. The vertical coordinate proposed by *Mahowald et al.* (2002) is described in the following section and the contributing diabatic heating rates as vertical velocities used in the present study.

2.2.2 Vertical Coordinate and Net Diabatic Heating

The vertical transport in CLaMS is described as deviations from isentropic surfaces (*Konopka et al.*, 2007a; *Ploeger et al.*, 2010). A hybrid coordinate ζ is used as vertical coordinate (*Konopka et al.*, 2007a), as proposed by *Mahowald et al.* (2002). The ζ-coordinate combines the terrain-following σ-coordinate for the troposphere and the Θ-coordinate for the radiation-dominated stratosphere (*Hoppe et al.*, 2014). The potential temperature Θ is defined as:

$$\Theta = T \left(\frac{p_s}{p} \right)^{R/c_p} \quad , \tag{2.1}$$

where p is pressure, p_s is surface pressure, R is gas constant, C_p specific heat capacity at constant pressure. The terrain-following σ -coordinate is defined as:

$$\sigma = p/p_s \quad , \tag{2.2}$$

The hybrid vertical coordinate ζ is then defined by:

$$\zeta = \Theta \cdot f(\sigma), \tag{2.3}$$

with

$$f(\sigma) = \begin{cases} \sin\left(\frac{\pi}{2} \frac{1-\sigma}{1-\sigma_r}\right) & \sigma > \sigma_r \\ 1 & \sigma \leq \sigma_r \end{cases} \quad . \tag{2.4}$$

Below a reference pressure of $p_r = 300$ hPa ($\sigma_r = p_r/p_s$) the vertical coordinate smoothly converts into a terrain following coordinate (*Mahowald et al.*, 2002; *Pommrich et al.*, 2014). Hence the vertical velocity in ζ coordinates is defined as

$$\frac{d\zeta}{dt} = \dot{\zeta} = \dot{f}\Theta + f\dot{\Theta} \quad , \tag{2.5}$$

$$\frac{d\Theta}{dt} = \dot{\Theta} = \Theta\frac{Q}{T} = \frac{J}{C_p}\frac{\Theta}{T} \quad , \tag{2.6}$$

where J is the diabatic heating rate per unit mass. Above the pressure reference, the vertical velocity can be interpreted approximately as the kinematic velocity respective the pressure gradient. A detailed derivation of the equation (2.6) can be read in Appendix B (6, eq. 2.14). Additionally, a summary of the relation between the thermodynamic energy equation to temperature tendencies is given.

The diabatic heating rate $\frac{J}{C_p}$ is needed for the calculation of $\dot{\Theta}$. The diabatic hating rate can be derived from diabatic temperature tendencies. From the first law of thermodynamics one can derive the thermodynamic energy equation which can be expressed as a sum of temperature tendencies with a dynamical term and a diabatic term:

$$\frac{dT}{dt} = \frac{R}{C_p}\frac{T}{p}\frac{dp}{dt} + \frac{J}{C_p} \quad . \tag{2.7}$$

$$\left(\frac{dT}{dt}\right)_{\text{total}} = \left(\frac{dT}{dt}\right)_{\text{dynamical}} + \left(\frac{dT}{dt}\right)_{\text{diabatic}} \quad . \tag{2.8}$$

Following that,

$$\frac{J}{C_p} = \left(\frac{\partial T}{\partial t}\right)_{\text{diabatic}} \quad . \tag{2.9}$$

Above the reference level the vertical velocity is dominated by $\dot{\zeta} \approx \dot{\Theta}$. Transport across an isentropic vertical surface can take place only through diabatic processes (*Kasahara*, 1974); the vertical velocity $\dot{\Theta} = d\Theta/dt$ for transport across potential temperature levels is therefore only deduced from the temperature tendencies caused by diabatic processes.

The dynamical core of ICON calculates total air density ρ as one of the prognostic variables, whereas pressure is only diagnosed for parameterizations. Therefore the coupling of dynamics and physics is performed at constant density (volume) rather than at constant pressure. This is different to many existing atmospheric models. Temperature tendencies derived from heating rates are converted within the ICON physics packages by using specific heat capacity at constant volume C_v (*Zängl et al.*, 2015). The difference of temperature tendencies and vertical velocities derived at constant volume compared to constant pressure is shown in the following.

Consider the definition of specific heat at constant pressure and at constant volume:

$$C_i = \left(\frac{dq}{dT}\right)_{i=const} \quad , \tag{2.10}$$

with $i = p, V$

$$(dq = C_i dT)_{i=const} \quad , \tag{2.11}$$

Because $dq = Jdt$:

$$(Jdt = C_i dT)_{i=const} \quad . \tag{2.12}$$

Divide by dt

$$\left(J = C_i \frac{dT}{dt}\right)_{i=const} \quad . \tag{2.13}$$

$$\frac{J}{C_i} = \left[\left(\frac{dT}{dt}\right)_{i=const}\right]_{diabatic} \quad . \tag{2.14}$$

Therefore, diabatic temperature tendencies are equal to diabatic heating rates divided by the respective specific heat. As it was stated above only diabatic heating processes are contributing to $\dot{\Theta}$. We combine equation (2.6) and equation (2.14):

$$\dot{\Theta} = \frac{\Theta}{T}\frac{J}{C_p} \quad . \tag{2.15}$$

$$\dot{\Theta} = \frac{1}{C_p}\frac{\Theta}{T}\frac{C_i}{C_i}J \quad . \tag{2.16}$$

$$\dot{\Theta} = \frac{C_i}{C_p}\frac{\Theta}{T}\frac{J}{C_i} \quad . \tag{2.17}$$

Case $i = p$

$$\dot{\Theta} = \frac{C_p}{C_p}\frac{\Theta}{T}\frac{J}{C_p} \quad . \tag{2.18}$$

Insert (2.14)

$$\dot{\Theta} = \frac{\Theta}{T}\left[\left(\frac{dT}{dt}\right)_{p=const}\right]_{diabatic} \quad . \tag{2.19}$$

Case $i = V$

$$\dot{\Theta} = \frac{C_V}{C_p}\frac{\Theta}{T}\frac{J}{C_V} \quad . \tag{2.20}$$

Insert (2.14)

$$\dot{\Theta} = \frac{C_V}{C_p}\frac{\Theta}{T}\left[\left(\frac{dT}{dt}\right)_{V=const}\right]_{diabatic} \quad . \tag{2.21}$$

The temperature tendencies ΔT_i from all processes that cause diabatic heating are added up:

$$\Delta T = \Delta T_{radsw} + \Delta T_{radlw} + \Delta T_{turb} + \Delta T_{drag} + \Delta T_{pconv} \quad , \tag{2.22}$$

which are temperature tendencies from short- and longwave radiation, turbulence, subgrid-scale and gravity wave drag and convective plumes.

2.2.3 Mixing

The mixing procedure of the ensemble of air parcels is performed in CLaMS with the module mix. The user can specify a mixing time step when the mixing event occurs. Between two mixing time steps the air parcels are transported by the trajectory module. Flow deformations caused by horizontal strain and vertical shear of the large-scale atmospheric flow induce the regions where mixing predominantly occurs (*Konopka et al.*, 2004, 2007a; *Riese et al.*, 2012).

At an initial state the modeled air parcels in CLaMS at a given specific isentropic level can be considered as quasi-uniform distributed grid points. In a first approximation, a grid point is surrounded by a circle with a mean distance r_0. A mean resolution distance r_0 is initially parameterized by the user for each isentropic model level individually. The mean distance r_0 increases with altitude, corresponding to the decreasing density of the atmosphere. At the initial state the distances to the nearest neighbors are approximately constant.

After one advection time step, air parcels follow the fluid flow and the grid is deformed. The deformation of the circle around one grid point can be described geometrically by an ellipse. *Geist et al.* (1990) showed that geometrically the logarithmic expansion rates of the deformation of ellipsoids from original circles are equivalent to the Lyapunov exponent λ. In CLaMS the critical distances in CLaMS are calculated with the critical Lyapunov exponent λ_c:

$$\frac{r_\pm}{r_0} = \exp\left(\pm\lambda_c \Delta t\right) \tag{2.23}$$

At the mixing time step, the modeled air parcels are projected onto the model levels. A Delaunay triangulation is performed on this projected plane to determine a network of nearest neighbors. Within this network of neighbors, the air parcel distances are calculated. Once, the critical distances are evaluated, the air parcels are either mixed or not mixed. For the mixing process there are two options, merging or insertion. If the distance between two air parcels is less than the minimum critical distance, the two air parcels are merged to form a new air parcel which is located at the mid-point of the two original air parcels. If the maximum distance is exceeded, a new air parcel is added in the center between the two air parcels without deleting the original air parcels. Further details on the implementation of the mixing algorithm and the linkage to the integral deformation of the flow are discussed in (*McKenna et al.*, 2002b; *Konopka et al.*, 2003).

The chemical mixing ratio of the air parcels which are subject to mixing is calculated from the average of the two previous air parcels. Every other mixing time step, a secondary set of vertical layers is mixed. The secondary set of vertical levels consists of those vertical distances ranging from the middle height of two consecutive original levels.

The mixing procedure implemented in this way induces strong mixing where deformation rates are stronger. In regions where deformation rates are lower, the mixing criteria is less frequently valid and mixing is scarce. The mixing process and the parameter tuning in CLaMS, where flow deformation is the basis for physical mixing, is validated in several studies (*Riese et al.*, 2012; *Konopka et al.*, 2003). Vertical shear induced mixing contributes to the vertical transport in the tropical troposphere layer in the vicinity of the sub tropical jet where increased horizontal strain and vertical shear rates are present (*Konopka et al.*, 2007b). Lagrangian transport including the physically deformation induced mixing reduces cross-tropopause diffusion enables to capture the hemispheric difference pattern in mean age of air (*Hoppe et al.*, 2016).

2.2.4 Chemistry

In CLaMS, a full stratospheric chemistry scheme can be employed, including heterogeneous reactions for polar chemistry (*McKenna et al.*, 2002a; *Grooß et al.*, 2005; *Müller et al.*, 2018).

Here we use the simplified chemistry scheme explained in detail by *Pommrich et al.* (2014). The simplified chemistry scheme calculates the reactions of the following species: CH_4, CO, CO_2, O_3, N_2O, CCl_3F, CCl_2F_2, H_2O; where the chemical loss in the lower stratosphere is calculated in a first order for the long lived species. About 90 percent of the chemical loss of N_2O is due to photolysis and 10 percent is oxidation by O(1 D) (*Minschwaner et al.*, 1993). The loss by photolysis and chemical reaction with radical species like OH and O(1 D) is calculated using diurnal average photolysis rates and tabulated OH and O(1 D) mixing ratios from a different model run. The main chemical stratospheric loss processes of N_2O read (*WMO*, 1982; *Thompson et al.*, 2014):

$$N_2O \xrightarrow{h\nu} N_2 + O(^1D). \tag{2.24}$$

$$N_2O + O(^1D) \longrightarrow 2\,NO. \tag{2.25}$$

$$N_2O + O(^1D) \longrightarrow N_2 + O_2. \tag{2.26}$$

Diurnally averaged loss rates determined by stratospheric temperature conditions in the laboratory are highest at altitude of 30 kilometers in the tropics. In latitudes of 60 degrees at 30 kilometers and at tropical UTLS region, the loss rates determined this way are 10 percent of the vales found in the tropics at 30 kilometer (*Minschwaner et al.*, 1993). The rate reactions coefficients are taken from the recommendations by *Sander et al.* (2011). Analysis in the upper TTL and lower stratosphere region showed that this simplified chemistry schemes captures the O_3-budget reasonably well (*Ploeger et al.*, 2011, 2012). Boundary conditions for long-lived tracers are prescribed at the lower model boundary (i.e. at the ground). For the lower boundary of N_2O groundbased baseline observations are used; the prescribed N_2O boundary is zonally symmetric but varies with the season (*Pommrich et al.*, 2014). Like in earlier work by *Pommrich et al.* (2014), the photolysis rates were calculated as diurnal averages using the CLaMS photolysis code in spherical geometry (*Becker et al.*, 2000), which is also implemented as the MESSy submodel DISSOC (*Sander et al.*, 2019).

2.3 Modular Earth Submodel System (MESSy)

The Modular Earth Submodel System (MESSy) provides an interface for different numerical models of the earth system to interact. Since the successful implementation of the climate model ECHAM within the MESSy framework (*Joeckel et al.*, 2010), many studies assessing the impact of anthropogenic emissions and biomass burning on the atmosphere (*Pozzer et al.*, 2012; *Rosanka et al.*, 2021) or analysis of stratospheric transport patterns (*Brinkop and Jöckel*, 2019; *Charlesworth et al.*, 2020, 2023) are conducted. The model framework is subdivided into base models and submodels. On the one hand, there is a large variety of submodels ranging from diagnostic models to process models, e.g. sampling in 4 dimensions (S4D) which interpolates model data to the trajectory of a moving observatory platform or calculation of cloud optical properties (CLOUDOPT). On the other hand, one of the key features of MESSy is the implementation of an atmospheric circulation model as a base model and the sub model interface layer. With the help of the sub model interface layer chemical tracer transport, online diagnostic tools, and many other models can interact with the base model. ICON, as an atmospheric circulation model, is implemented as base model in MESSy by *Kern and Jöckel* (2016). The MESSy version used in this study is d2.54.0.3 including ICON version 2.4.

2.4 The coupled model system ICON/MESSy-CLaMS

In the present study, the ICON/MESSy model is used to study Lagrangian transport processes in the stratosphere using advection and mixing from CLaMS. For this purpose, the sub model CLaMS is edited in such a way, that data exchange with the base model ICON, and any other MESSy sub models, are possible. The data exchange is organized with generic submodel CHANNEL. The sub model CHANNEL enables access to a set of prognostic and diagnostic variables of the basemodel, i.e. ICON, at every integration time step, for all other submodels. In addition to that, data exchange between all submodels, not just the base model, is possible.

2.4.1 GRid AGGregation (GRAGG)

In this study GRid AGGregation (GRAGG) is used as an intermediate step to interpolate the ICON variables from the ICON horizontal grid structure to a globally regular longitude latitude grid. GRAGG is developed as a diagnostic sub model within the MESSy framework to calculate variables of interest online during ICON integration time step (*Kern and Jöckel*, 2016). The user can define a spatial area by coordinates of longitude and latitude and a grid spacing within this region. The diagnosis within this region allows to reduce I/O due to two main features of grid aggregation. First, arithmetic operations over ICON native grid cells reduce the amount of grid points in output files. Second, the I/O operations are reduced to the region of interest defined by the user. After the integration time step, the updated prognostic and diagnostic variables of the base model are aggregated by GRAGG to the chosen regular longitude latitude grid at every vertical ICON level. In this study, a global longitude latitude grid of 2°×2° is defined. The meteorological information for CLaMS trajectory calculation is required globally. ICON prognostic wind components, temperature and pressure, surface pressure, and temperature tendencies described in section (2.2.2) are diagnosed on the aggregated grid by an arithmetic average of the native ICON grid points. After the grid aggregation by GRAGG the meteorological information is in a format readable for CLaMS input. With the so diagnosed meteorological fields, the CLaMS vertical levels are calculated according to the vertical coordinate. Furthermore, the operational call of the GRAGG diagnostics is required during each iteration step, as the updated variables are needed for the CLaMS advection calculation at every time step. The calculation of dynamical climatologies in section (3) are equal to the variable fields grid aggregated by GRAGG in the intermediate step between ICON prognostic variables and input wind fields for the transport calculated in CLaMS.

2.5 Simulation Setup

The ICON/MESSy-CLaMS simulation, performed in this study, is a 10-year time slice simulation with chemical boundary conditions of the year 2005. Monthly means for 2005 as well as

sea-surface temperatures and sea ice concentrations are repeating every year. The sea surface temperature and sea ice concentration are taken from the AMIP II simulations (*Taylor et al.*, 2000) and interpolated from the original grid structure to the ICON grid structure used. The horizontal grid structure contains 20480 grid cells and has a horizontal resolution of approximately 158 km. The ICON grid notation defines this grid as R2B4. ICON model top is set at 80 km. The simulation is performed on a vertical grid with 90 levels of which 32 levels are entirely in the troposphere and 34 levels are entirely in the stratosphere. The general circulation of the ICON atmosphere is free running. Boundary conditions for long-lived tracers are prescribed at the lower model boundary (i.e. at the ground). In the simulations reported here, the focus is on nitrous oxide (N_2O). For the lower boundary of N_2O ground based baseline observations are used; the prescribed N_2O boundary is zonally symmetric (*Pommrich et al.*, 2014). CLaMS is initialized with approximately 1.5 Million air parcels with a model top of 2500 K. The time step in ICON used here is 900 s; the CLaMS transport is called after each ICON time step, it is thus 900 s as well. The mixing with a Lyapunov exponent of 1.5 and chemical routines of CLaMS submodels are called every 24 hours.

2.6 Measurements of N_2O by the Microwave Limb Sounder

The Earth Observing System (EOS) Microwave Limb Sounder (MLS, (*Waters et al.*, 2006)) is an instrument onboard the EOS Aura satellite. Aura was launched on 15 July 2004 and takes measurements since August 2004 until today. The MLS scans the Earths limb from the surface to 95 km altitude every 26 s allowing MLS to take atmospheric observations from 82°S to 82°N. MLS gives daily global coverage. From the microwave radiance measurement a large number of profiles of the vertical abundance of trace species are deduced (e.g. *Livesey et al.* (2021)), here MLS measurements of N_2O are of particular importance. We use MLS v4 data (*Livesey et al.*, 2017); as we focus here on seasonal to annual changes (and not on long-term variability and trends) our use of MLS N_2O will therefore not be affected by the drift detected in this data set (*Livesey et al.*, 2021). For constructing the MLS climatologies of nitrous oxide the measurements were interpolated on isentropic levels for each vertical profile. The vertically interpolated profiles are binned horizontally to a regular 2°x 2°longitude-latitude

grid. The accumulation in bins is done for each month individually for the time period of 2005-2017 and averaged for each month afterwards.

2.7 The ERA-Interim and ERA-5 Reanalysis

A reanalysis combines model data with observations into a globally complete and consistent dataset employing a model (*Fujiwara et al.*, 2017). This combination, referred to as data assimilation, is similar to estimating the (initial) state of the atmosphere for numerical weather prediction. The ERA-Interim reanalysis (*Dee et al.*, 2011) is used here as a reference to assess the quality of wind and transport patterns simulated by the model presented here (ICON/MESSy-CLaMS). In ERA-Interim, both the residual circulation in the stratosphere and the structure and magnitude of radiative heating are reasonably realistic (*Fueglistaler et al.*, 2009). In addition ERA5 Reanalysis, a new-generation data set of ECMWF Reanalysis is used (*Hersbach et al.*, 2020), for the zonal mean zonal wind climatologies discussed in chapter (3). The data set of ERA5 reanalysis used in the present study is a downscaled version of ERA5 to the temporal and horizontal resolution of ERA-Interim. Hence, the data from ERA-Interim and ERA-5 Reanalysis were retrieved on all model levels and interpolated to a longitude and latitude resolution of 1°x 1°latitude–longitude grid with 137 vertical levels for ERA5 and 60 vertical levels for ERA-Interim Reanalysis.

Chapter 3

Zonal Mean Climatologies

In the following chapter, the mean state of the model stratospheric dynamics and chemical distribution of nitrous oxide are assessed. The horizontal wind patterns and the vertical velocity derived by diabatic heating rates are compared to climatological zonal mean measures of the same time period of ERA-Interim and ERA5 reanalysis. The diagnostics relevant for the stratospheric transport and the circulation of air masses into the polar vortex region are discussed. The dynamical processes governing the chemical Lagrangian transport in CLaMS are evaluated, and the processes and quantities considered are those relevant for modeling the long-term behavior of stratospheric nitrous oxide. The climatological chemical distribution of nitrous oxide (N_{20}) are discussed later in that chapter by comparison to climatologies of Microwave Limb Saunder observations. Brief glimpses of the annual zonal mean distribution in the model representation of water vapor (H_2O), methane (CH_4), Trichlorofluoromethane (CFC_{11}) and ozone (O_3) are provided.

3.1 Model dynamics

3.1.1 Zonal mean zonal wind

The characteristic feature of the stratospheric vortex is a strong westerly wind. The vortex forms in the northern hemisphere in boreal autumn and extend vertically from the lower stratosphere to the upper stratosphere lower mesosphere (*Waugh and Randel*, 1999; *Waugh and*

Polvani, 2010; *Waugh et al.*, 2017). There is a strong temperature gradient between the equator and the North Pole due to the lack of sunlight at the North Pole in autumn. Wind speeds peak in boreal winter and then decrease again in boreal spring with the return of sunlight. Similarly, the stratospheric vortex evolves in the southern hemisphere in aural autumn, winter and spring. The persistence and variability of the polar vortices is investigated in a study by *Waugh et al.* (1999) in order to determine the date of the vortex breakup in spring. The stratospheric vortices of the hemispheres are different. Due to the different distribution of land masses of the southern and northern hemispheres the equilibrium of the vortex is disturbed differently. This is caused by the varying amount and strength of planetary-scale Rossby waves. Fewer and weaker wave disturbances in the southern hemisphere, leads to a stronger more persistent polar vortex. The center of the westerly jet is considered approximately to be the edge of the polar vortex (*Waugh and Polvani*, 2010; *Waugh et al.*, 2017; *Baldwin et al.*, 2019). The strong gradients surrounding the stratospheric polar vortex isolate the polar vortex air and act as transport barrier (*McIntyre*, 1989; *Waugh and Polvani*, 2010; *Baldwin et al.*, 2019). The structure and characteristics of the stratospheric polar vortex help to estimate the transport of chemical species across the barrier.

A climatological analysis of the zonal mean zonal winds provides a first insight into the structure and the conditions of the stratospheric polar vortices. To validate the representation of the basic dynamical state of an atmospheric circulation model, the zonal mean zonal wind field is used with the focus on the stratopsheric vortices (*Waugh and Polvani* (2010); *Hegglin et al.* (2010)). For the zonal mean zonal wind climatologies, zonal u and meridional v wind fields are calculated to the absolute velocity of the wind x_{vel} with the norm of both vector components for each timestep individually, i.e.: $x_{vel} = \sqrt{u^2 + v^2}$. In the next step monthly averages of the absolute velocity fields are calculated, followed by zonal mean averages. The grid aggregation is performed with a horizontal resolution of 2°x 2°degrees. For comparison, the zonal mean zonal wind structures of ERA-Interim and ERA5 reanalysis are calculated in the same way. The data from ERA-Interim and ERA5 reanalysis were retrieved on all model levels and interpolated to a longitude and latitude resolution of 1°x 1°latitude–longitude grid. A comparison of the zonal mean zonal wind speeds in a latitudinal potential temperature cross

section for different seasons are shown in Figures 3.1 and 3.2. The potential temperature is used as vertical coordinate. In the left panel the horizontal wind structure of ERA-Interim (ERA5) is shown and on the middle panel for ICON/MESSy-CLaMS. The right panel shows the percentage difference with respect to ERA-Interim (ERA5), i.e.: negative percentage values mean ICON/MESSy-CLaMS has lower wind speed than ERA-Interim (ERA5).

In boreal winter in the northern hemisphere (see top Figure 3.1), in the upper stratosphere, the horizontal wind velocities are comparable in strength and structure with only a percentage difference up to 10 %. The maximum wind speeds 40 m/s and 50 m/s in ICON/MESSy-CLaMS at 58.8°N are vertically more extended down to isentropic levels of 750 K and 1100 K (28 km - 35 km). The velocities are shifted vertically downwards by 400 K compared to ERA-Interim (61.8°N). This leads to stronger winds in ICON/MESSy-CLaMS in the middle stratosphere by 40 %. In the lower stratosphere, the intermediate velocities (20 m/s - 30 m/s) modeled in ICON/MESSy are more extended to the troposphere and gradually decrease stronger in the vertical direction. In the ERA5 reanalysis (see bottom Figure 3.1) the differences are quite similar to those found in ERA-Interim. The velocity contours of 20 m/s to 30 m/s of the northern hemisphere polar vortex are vertically more extended down in the middle stratosphere. This leads to differences of 30 %, whereas in ERA-Interim the difference is 40 %. The strong velocities in the southern hemisphere upper stratosphere with up to 60 m/s - 70 m/s in ICON/MESSy-CLaMS are not captured in the ERA5 reanalysis, although the 55 m/s contour is more elongated in ERA5 reanalysis as to ERA-Interim, leading to smaller differences.

In boreal summer in the southern hemisphere (see top Figure 3.2), in the upper stratosphere, the horizontal wind velocities are comparable in strength and structure with the largest difference up to 40 % in a small region around the isentropic level of 2300 K. The maximum wind speeds of 90 m/s are measured in ERA-Interim at isentropic level reaching down to 1850 K, where in ICON/MESSy-CLaMS the wind speeds are shifted vertically beginning at 2300 K reaching down to 1250 K. In the middle stratosphere the 70 m/s horizontal wind speed contour at 58.8°S at 730 K in ERA-Interim. In ICON/MESSy-CLaMS the 70 m/s contour is modeled at 52.9°S at 800 K. The maximum wind speeds in ERA5 of 90 m/s in the southern hemisphere

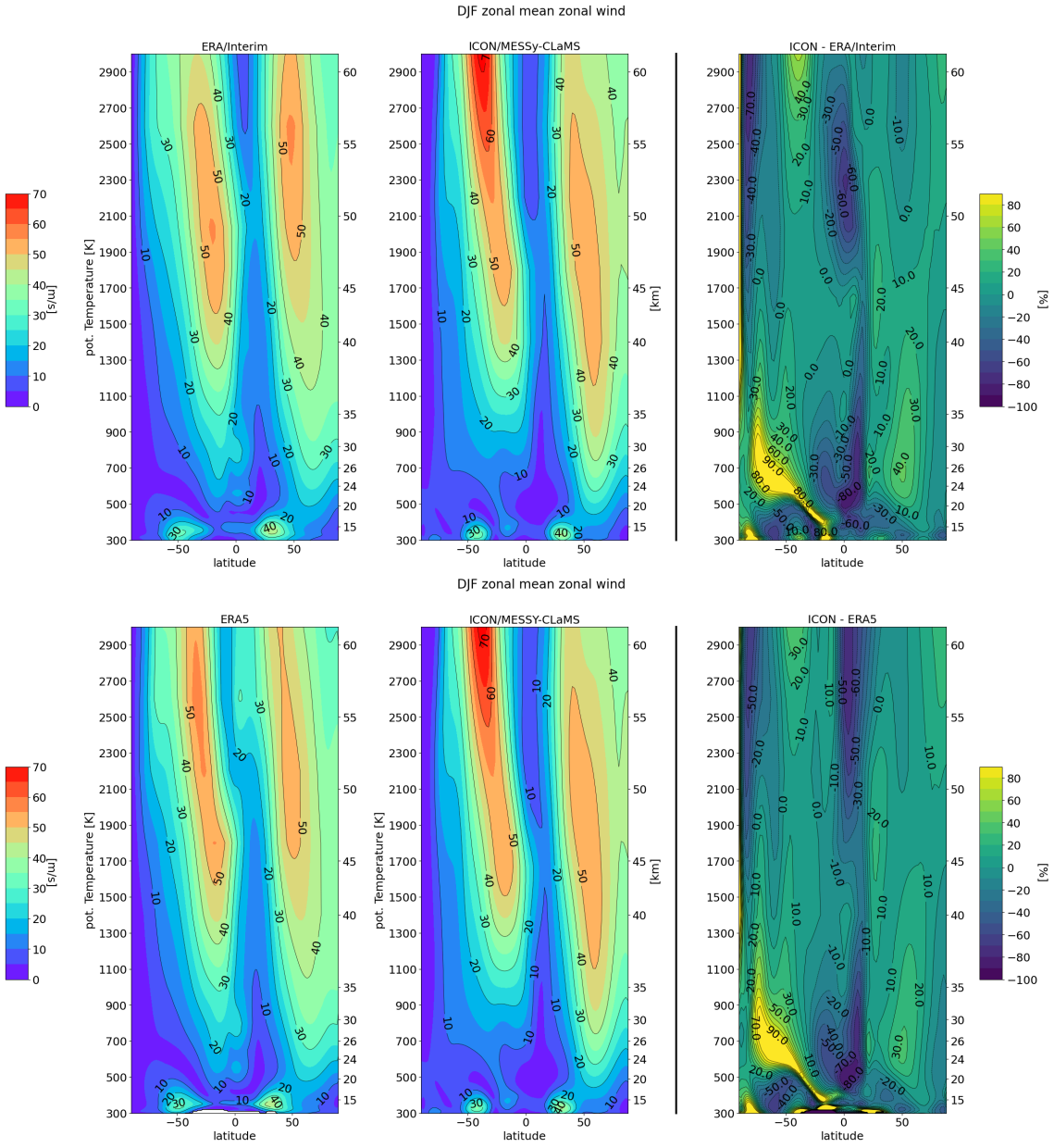

Figure 3.1: Zonal mean of horizontal wind speed from ERA-Interim and ERA5 2005-2014 climatology (top left and bottom left column) and ICON/MESSy ten year climatology (middle column). Percentage difference, ICON/MESSy minus Reanalysis divided by Reanalysis (right panel): December to February (DJF) season.

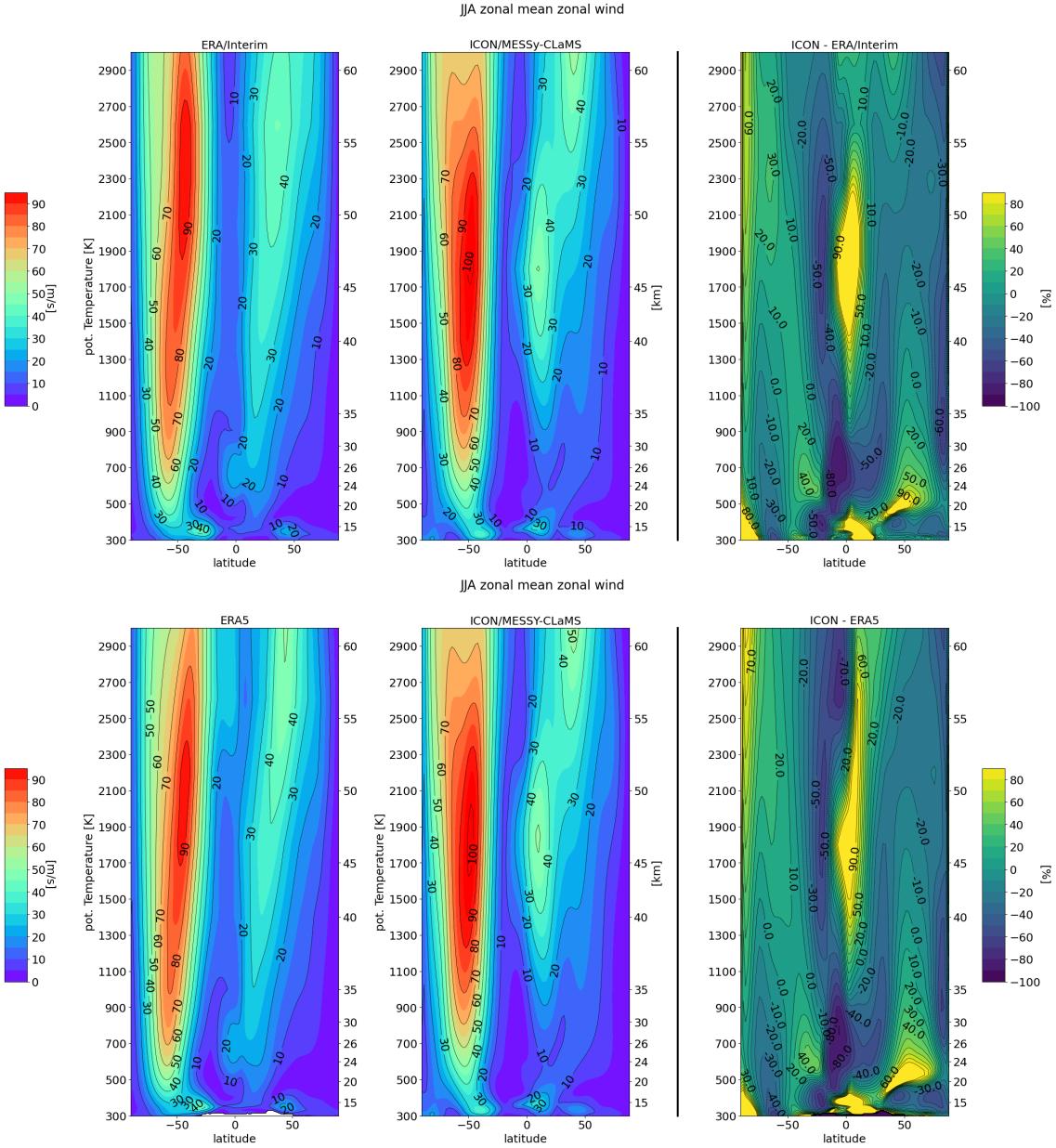

Figure 3.2: same as Figure 3.1 except for: June, July, August (JJA) season

are found between 1700 K and 2300 K (see bottom Figure 3.2). The vertical range is more comparable to ICON/MESSy-CLaMS than in ERA-Interim. This leads to slightly reduced differences. Nevertheless, the differences found between ERA5 and ICON/MESSy-CLaMS are similar to those found between ERA-Interim Reanalysis. In the lower stratosphere the stratospheric westerlies in ICON/MESSy-CLaMS are not as much extended in meridional direction as ERA-Interim Reanalysis. The meridional extension of the ICON/MESSy-CLaMS 20 m/s contour line is reduced at the 450 K isentropic level. The 20 m/s contour line extends from -69.1°S to -39.7°S. The ERA-Interim 20 m/s contour at 450 K extends from -70.6°S to -32.4°S. The transport barrier between 400 K and 500 K in ICON/MESSy-CLaMS at 64°S contains of 40 % weaker maximum horizontal wind speeds (see Figure 3.3). Overall the seasonal structure of the stratospheric polar vortex is well captured by ICON/MESSy-CLaMS model. The stratospheric jets are clearly noticeable, in particular the edge of the polar vortex.

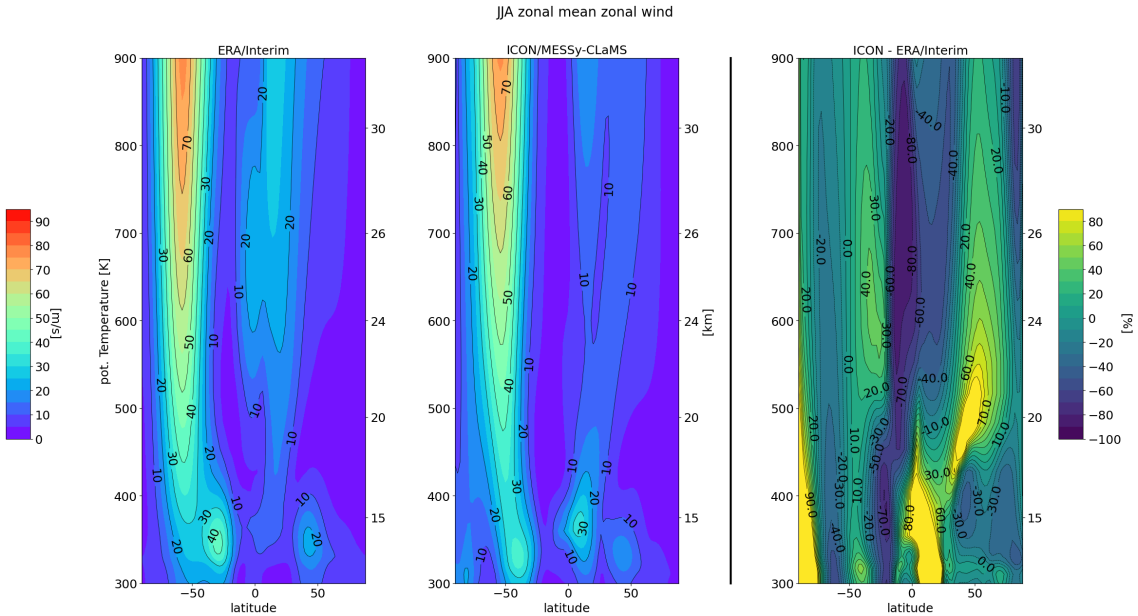

Figure 3.3: as Figure 3.2 except for vertical range of 300 K - 1200 K

A vertical analysis of the maximum wind speed and the meridional location is shown in Figure (3.4). In the top left panel we can see that in DJF season the strength of the stratospheric polar vortex is stronger in ICON/MESSy-CLaMS compared to ERA-Interim, where it is slightly underestimated in middle and lower stratosphere in JJA season. The location of the polar vortex in the northern hemisphere (see Figure 3.4 ; top right panel) is modeled in

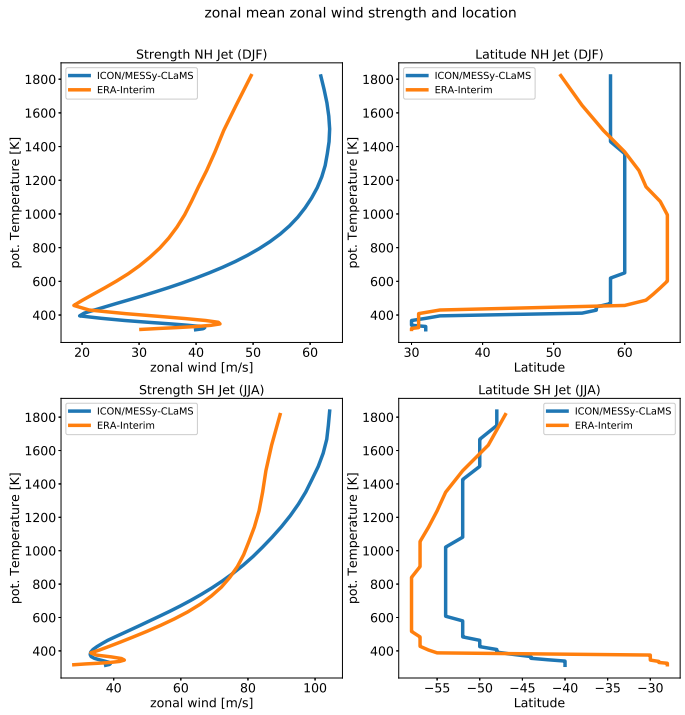

Figure 3.4: Zonal wind speed and latitude of the jet maximum of the NH DJF climatology (top), and of the SH JJA climatology (bottom) of the zonal mean of horizontal wind speed shown in Figure (3.1 and 3.2)

ICON/MESSy-CLaMS at 60°N where it is slightly shifted polewards in ERA-Interim. In the southern hemisphere the polar vortex location of ICON/MESSy-CLaMS is shifted about ten degrees to the equator.

The model evaluation of ICON-A compares the zonal mean zonal wind structure in a multi annual mean climatology to ERA-Interim in a R2B4 horizontal resolution as well as in higher resolution (R2B6) (*Crueger et al.*, 2018). Those horizontal resolution are comparable with the ECHAM6.3-LR and ECHAM6.3-HR, respectively. In addition, the simulation setup includes accompanying model runs of ECHAM6.3-LR and ECHAM6.3-HR. The differences reported in the annual mean maximum wind speeds in the middle stratospheric southern polar vortex among the models reported in (*Crueger et al.*, 2018) are small. *Jungclaus et al.* (2022) presented the ICON-ESM model, where the atmospheric circulation of ICON-A is implemented in an Earth System Model which consists of ICON-O (*Korn*, 2017) and HAMOCC (*Ilyina et al.*, 2013) for the ocean circulation and ocean processes, ICON-Land (*Reick et al.*, 2021) for physical and chemical land processes. The biases in the annual and seasonal zonal

wind is increased by the tuning to the coupled performance of all model compartments compared to ICON-A circulation simulations evaluated in *Crueger et al.* (2018). The biases in the zonal wind structures in the ICON-NWP model derived by grid aggregation in MESSy with the submodel GRAGG presented in this study are of the same magnitude as reported in *Crueger et al.* (2018) albeit the physics package of NWP version is used in the present study. The presented general circulation of the atmosphere performs reasonably well and is suitable for chemical Lagrangian transport with CLaMS.

3.1.2 Diabatic vertical velocities

Vertical velocities for CLaMS air parcel transport are determined by diabatic heating rates (section 2.2.2). In the following section, the diabatic vertical velocities are shown in a vertical range from 450 K up to 900 K and up to 2500 K. The analysis of nitrous oxide later in that chapter is compared to MLS climatologies, which are calculated from 450 K up to 900 K. The chemical transport simulation in CLaMS is calculated with a model top of 2500 K. In Figures (3.5 and 3.6) the vertical velocities for ERA-Interim and ERA5 as well as for ICON/MESSy-CLaMS are shown as an annual mean. For the temporal downscaled version of ERA5, an averaging for the diabatic heating rates is required. The reader is referred to *Ploeger et al.* (2021) for the details. On the abscissa the latitudinal direction is shown, while on the ordinate the altitude of the atmosphere in potential temperature is indicated. The unit of diabatic vertical velocity is Kelvin per day. The color code in left and middle panel of Figures (3.5 - 3.10) is blue for negative values and red for positive values. Positive (red) values indicate upward transport, where on the contrary, negative (blue) values indicate downward transport. The diabatic vertical velocities are compared to ERA-Interim (ERA5) Reanalysis from the perspective of the modeled velocities in ICON/MESSy-CLaMS, If not explicitly said otherwise.

The mean annual vertical transport is updraft in the tropics and vertical downdraft in the polar regions. The general vertical transport structure is well captured in ICON/MESSy-CLaMS (see Figure 3.5). There are some differences simulated in ICON/MESSy-CLaMS. The model simulated increased downdraft in the polar region in the middle and upper stratosphere and reduced updraft in the tropics in middle stratosphere. There is enhanced updraft in the

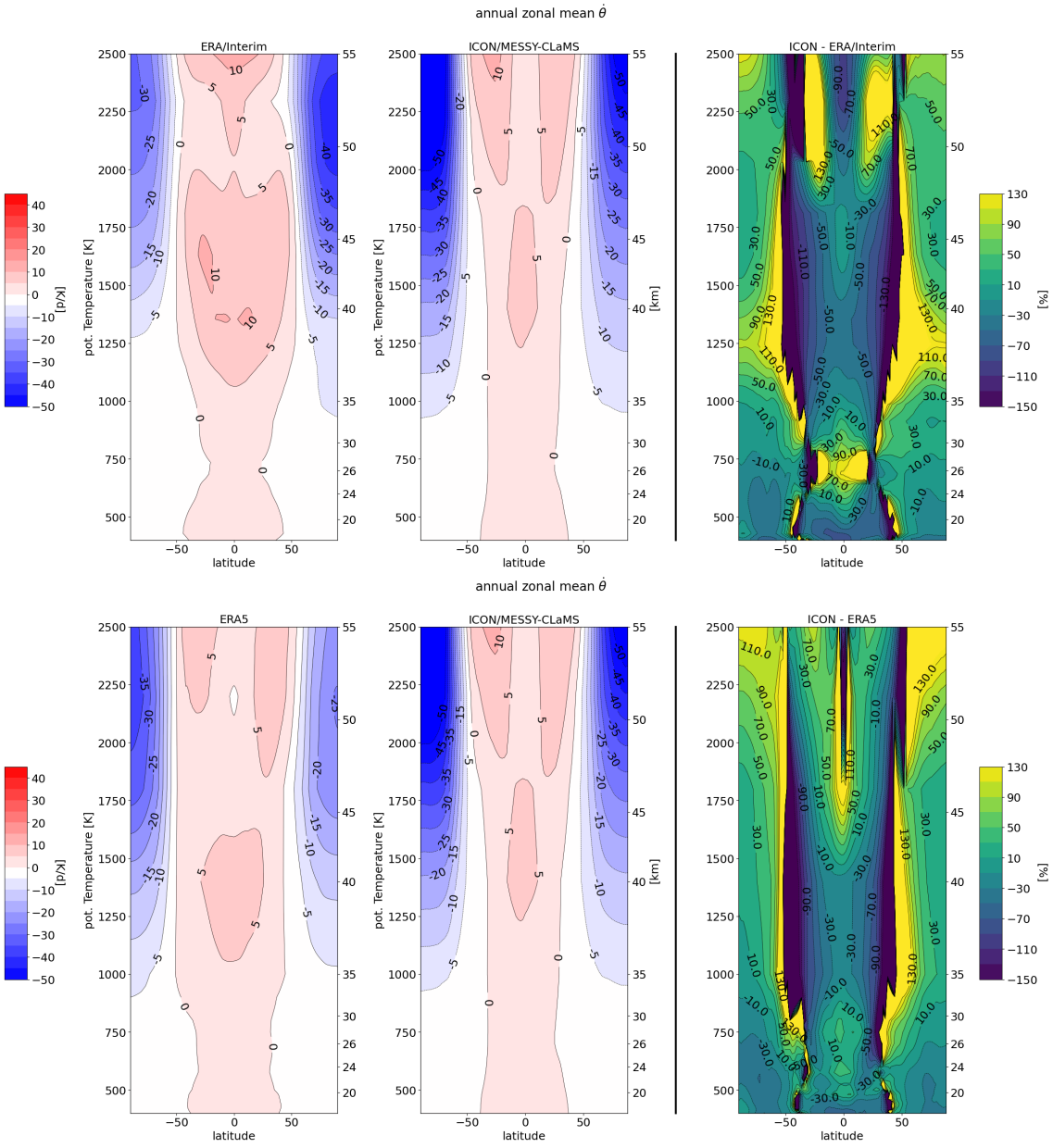

Figure 3.5: Zonal mean diabatic heating rates from ERA-Interim and ERA5 2005-2014 climatology (top left and bottom left column) and ICON/MESSy ten year climatology (middle column). Percentage difference, ICON/MESSy minus ERA-interim divided by ERA-interim (right panel): Annual mean in vertical range from 400 K potential temperature up to 2500 K.

tropics at the isentropic level of 750 K and strongly enhanced downdraft in the northern polar region in middle stratosphere. In Figure (3.6) the details in the lower and middle stratosphere are shown. The tropical updraft is reduced in ICON/MESSy-CLaMS with respect to the reanalysis in the vertical range from 450 K up to 600 K and strongly increase above 600 K. The downdraft in the southern hemisphere is slightly reduced by 10% - 30%. The downdraft in the northern hemisphere is enhanced above 600 K and reduced below. The downdraft at the model top of ICON/MESSy-CLaMS is overestimated by up to 100% in both polar region compared to ERA5, whereas the difference in the downdraft in the polar region in the middle stratosphere between 1000 K and 1500 K is more comparable between ERA5 and ICON/MESSy-CLaMS. The tropical updraft between 500 K and 800 K in ERA5 is different by 10 % to 30 %. The difference in ERA-Interim where considerably higher, 50 % - 120 %. The differences in the annual mean diabatic heating rates between the model simulation and the Reanalysis are significantly reduced using the ERA5 reanalysis reference, especially in the middle stratosphere polar region downdraft and the lower stratospheric tropical updraft.

The vertical transport in the boreal winter season is shown in Figures (3.7 and 3.8). The ICON/MESSy-CLaMS model calculates in the southern hemispheric polar region reduced updraft by values of 20% to 90%. The updraft in the tropics is reduced above 1000 K and below 650 K. There is a strong enhanced updraft between 650 K and 800 K. In the northern hemispheric polar region the model simulates enhanced downdraft by 70 % down to 650 K and reduced downdraft between 450 K and 600 K.

In Figures (3.9 - 3.10) the diabatic vertical velocities in aural winter season are shown. The ICON/MESSy-CLaMS modeled downdraft velocities in the southern polar region are overestimated by 30 % - 50 % in the upper and middle stratosphere with respect to the reanalysis. The vertical velocities in the lower stratosphere in the southern hemispheric in the region of the transport barrier matches the values of ERA-Interim by 10 %. In the tropics in the lower stratosphere the updraft is underestimated by values of 50 % to 90 % and overestimated by values of up to 120 % at isentropic levels of 600 K to 800 K. In the upper stratosphere the updraft in ICON/MESSy-CLaMS is underestimated at levels of 1000 K up to 2000 K by values of 40 %. In the northern hemisphere in the lower stratosphere, a weak updraft is modeled by

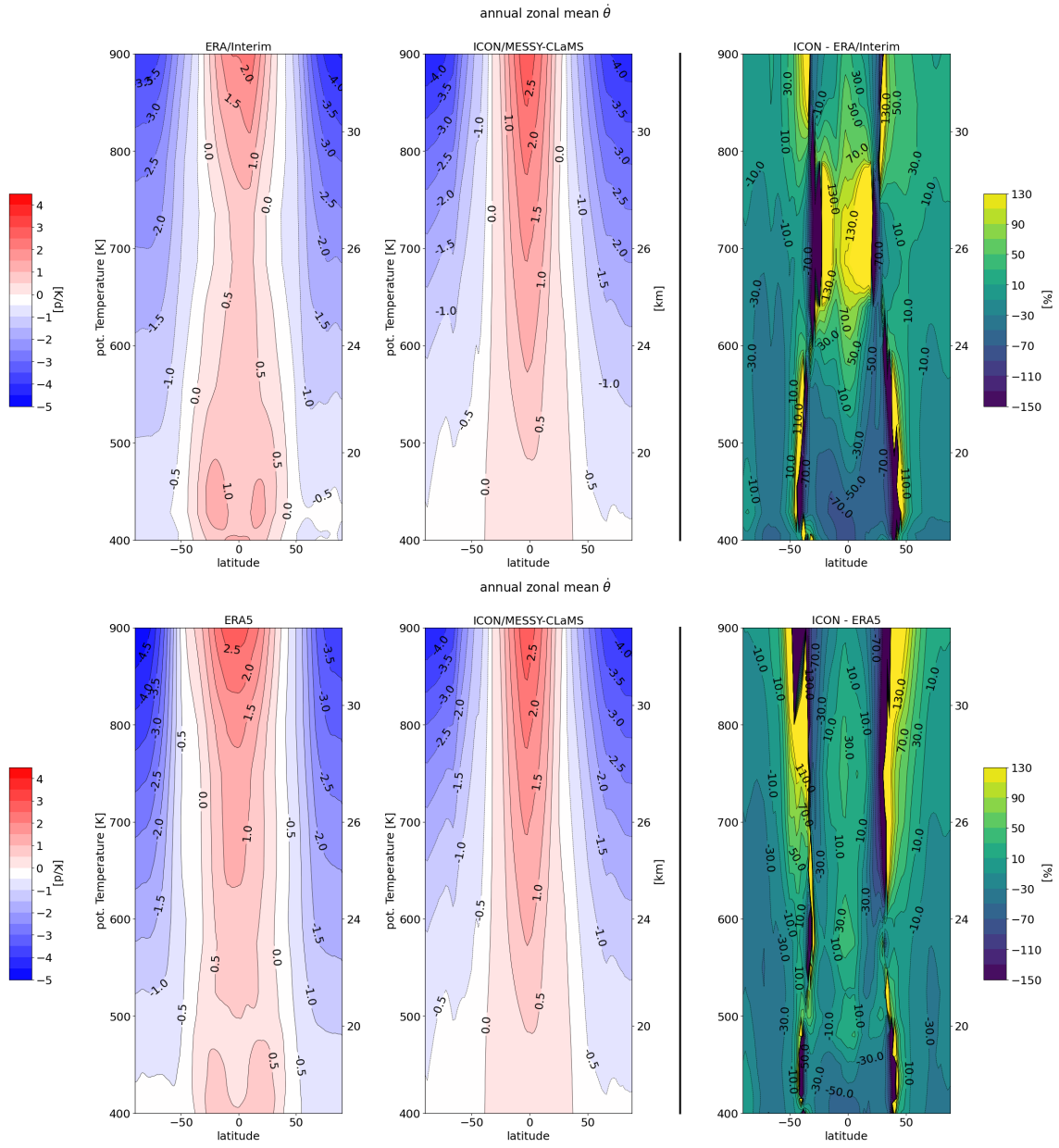

Figure 3.6: same as Figure 3.5 except for: vertical range from 400 K potential temperature up to 900 K.

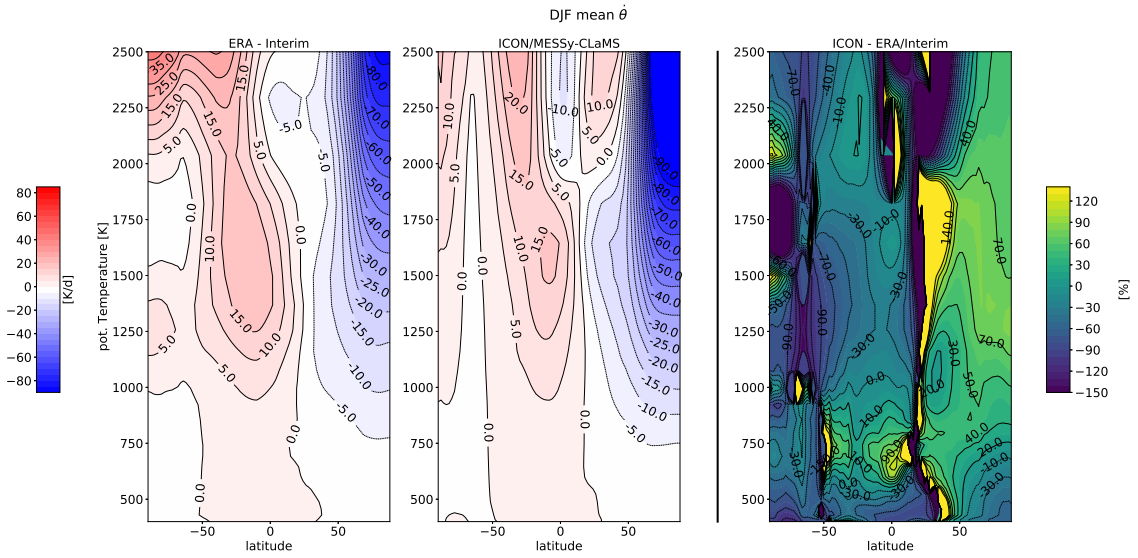

Figure 3.7: same as Figure 3.5 except for: December to Februar (DJF) season

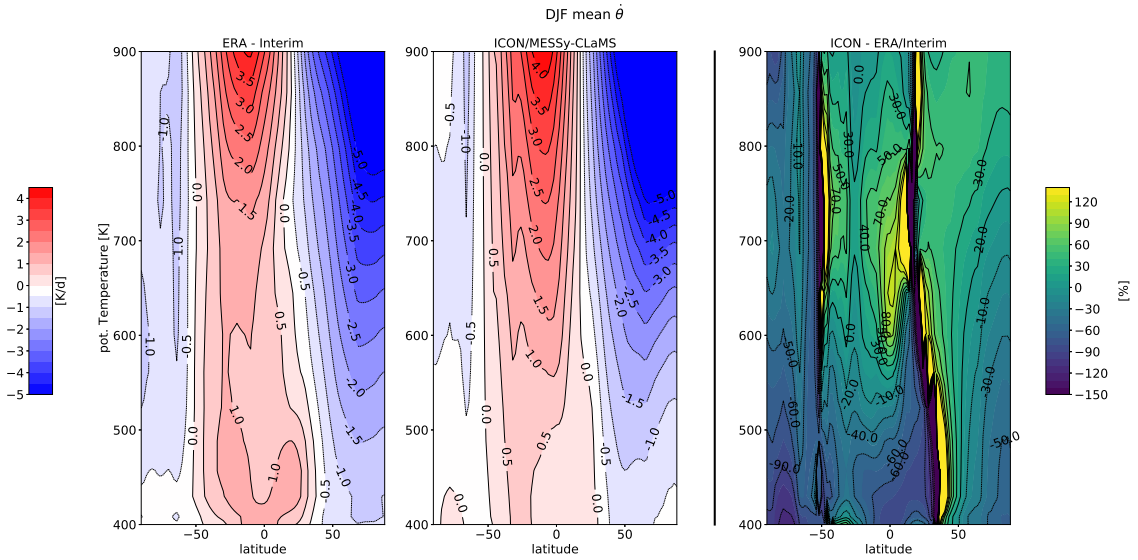

Figure 3.8: same as Figure 3.7 except for: vertical range from 400 K potential temperature up to 900 K.

ICON/MESSy-CLaMS where ERA-Interim predicts weak downdraft.

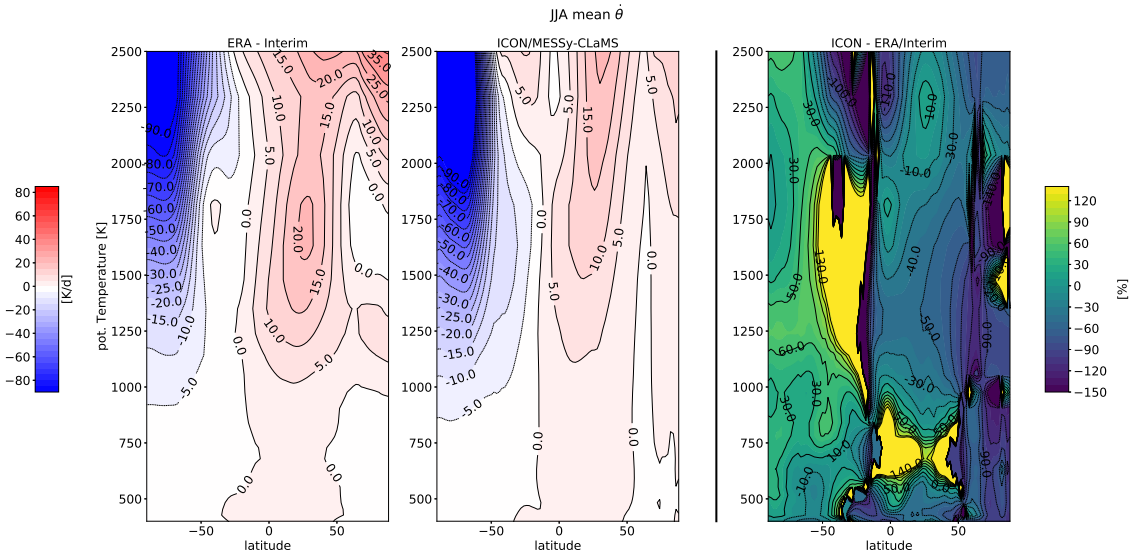

Figure 3.9: same as Figure 3.5 except for: June, July, August (JJA) season

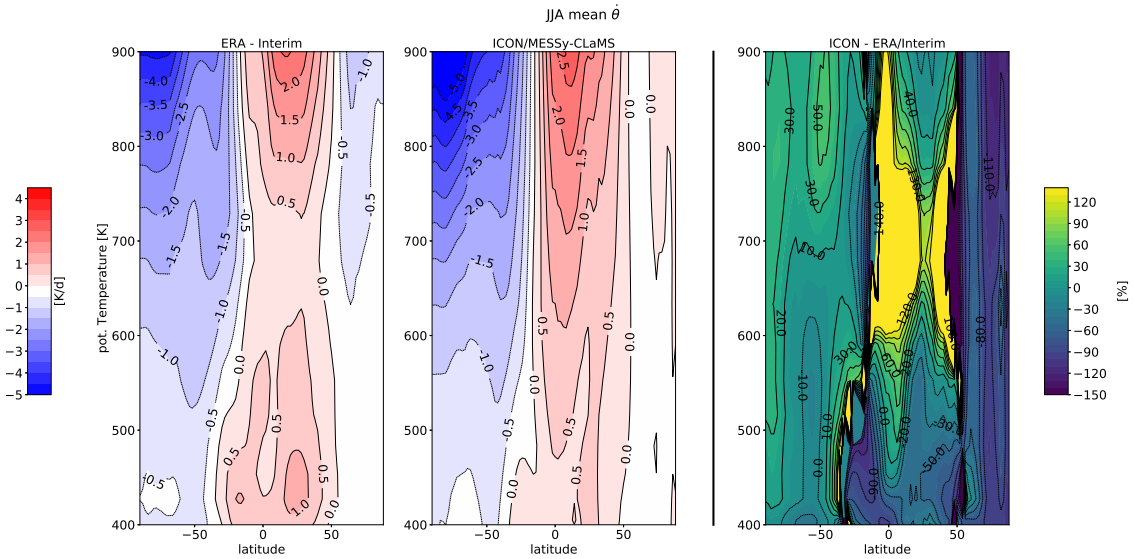

Figure 3.10: same as Figure 3.9 except for: vertical range from 400 K potential temperature up to 900 K.

3.2 Zonal climatologies of nitrous oxide

For model evaluation and analysis of a Chemistry Climate Model, metrics of key processes are quantified and compared to observations. Those observations include satellite data, meteorological reanalyses, ground-based data, balloon flights and aircraft data. The instruments on board satellites measure trace gases using various methods (limb emission, solar occultation, stellar occultation, limb scattering, Nadir emission). The Chemistry Climate Model Validation Project (*Eyring et al.*, 2010) argued that systematic comparison of existing observations is helpful to increase knowledge about the availability, quality and consistency of various satellite measurements. As a result, the SPARC Data Initiative decided to develop an assessment of stratospheric trace gas and aerosol climatologies from satellite limb sounders (*Hegglin and Tegtmeier*, 2017). The report constructs zonal monthly climatologies for a number of satellite instruments (LIMS on Nimbus, SAGE I on AEM-8, HALOE on UARS, MIPAS on Envisat, ACE-FTS on SCISAT-1, MLS on Aura and others) and then evaluates the differences and quality according to metrics of annual and monthly zonal mean climatologies, vertical and meridional mean profiles, seasonal cycles and interannual variability. The following analysis focuses on key processes of stratospheric transport. For that purpose monthly zonal mean climatologies of the model output are compared to climatologies compiled from satellite observations of the MLS instrument on Aura.

For constructing the climatologies of CLaMS trace gas, the simulated air parcels are interpolated on a regular longitude-latitude grid for each isentropic level individually. Ten simulation years are accumulated and monthly and zonally averaged. The seasonal zonal mean structure of nitrous oxide climatologies calculated from ICON/MESSy-CLaMS are shown in Figure (3.11). The chemical distribution of the volume mixing ratio in parts per billion (ppbv) is shown color coded, where the latitude is shown on the x-axis and the isentropic levels in potential temperature on the y-axis.

In Figure (3.11) four panels show the zonal mean climatologies of the seasons for nitrous oxide in the vertical range from 350 K to 1200 K. The chemical distribution resembles the mean state of the atmosphere of nitrous oxide as discussed in climatologies obtained by *Heg-*

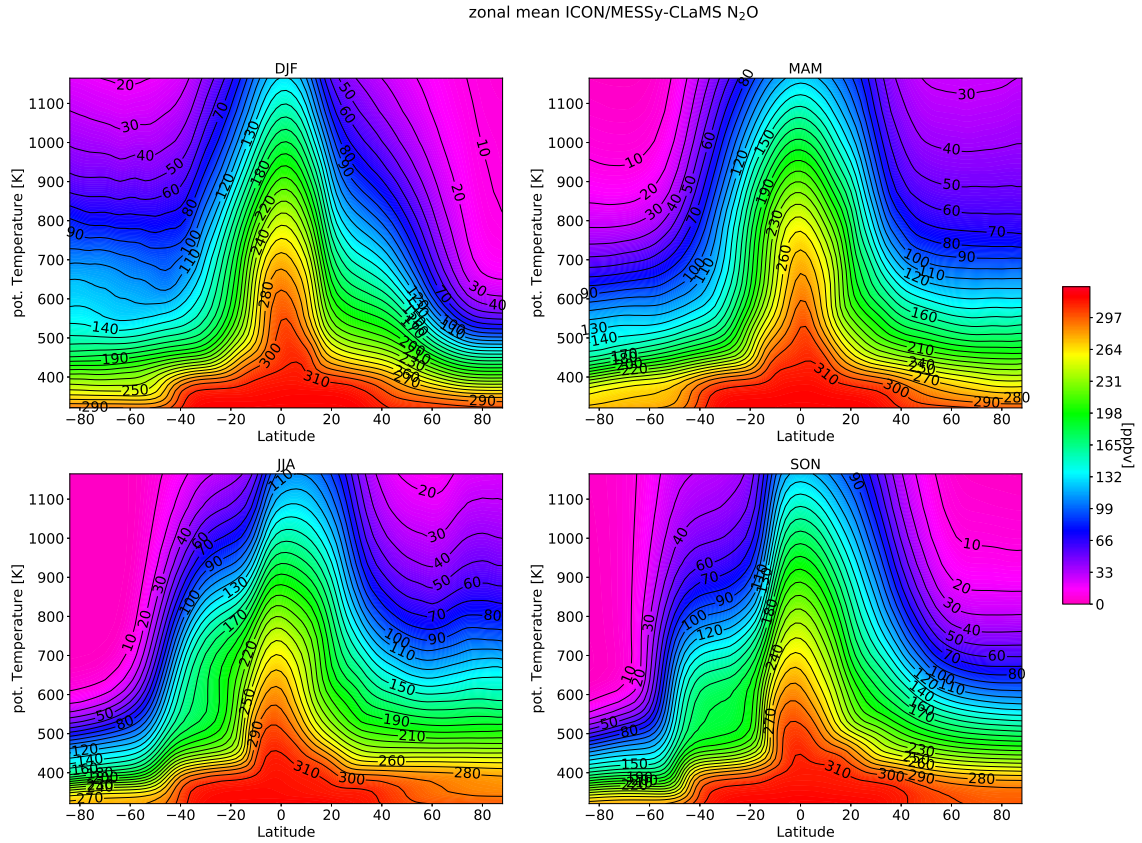

Figure 3.11: Zonal mean nitrous oxide volume mixing ratio for seasonal ten year climatology simulated in ICON/MESSy-CLaMS. Vertical range from 350 K potential temperature up to 1200 K.

glin and Tegtmeier (2017), as well as other climatologies of satellite observations (*Grooß and Russell*, 2005) and other models (*Jin et al.*, 2009; *Froidevaux et al.*, 2019). Nitrous oxide as a long lived species with only very weak chemical sinks (e.g.: O(1 D) and Photolysis) is well mixed in the troposphere with high volume mixing ratio and enters the stratosphere mainly in the tropics and is transported upward in the stratosphere in the tropical pipe. This robust peak of high volume mixing ratios (318.91 ppbv in 2005 annual mean *Lan et al.* (2023)) is modeled consistently in the tropics throughout the seasons. The seasonal change in the lower stratospheric region in the winter hemisphere exhibits air masses with low concentrations which are transported by downdraft from the upper stratosphere. The seasonal cycle is well captured by ICON/MESSy-CLaMS.

In Figures (3.12 - 3.16) the modeled climatologies of nitrous oxide are compared to the climatologies obtained from MLS nitrous oxide. The zonal mean averages are calculated for

the seasons and for an annual mean. The analysis of the chemical distribution and transport barrier focuses on the lower and middle stratosphere. Therefore, the vertical coordinate potential temperature ranges from 450 K to 900 K. The left panel shows the volume mixing ratio of MLS nitrous oxide and the middle panel shows the modeled volume mixing ratio. The percentage difference are shown on the right panel, i.e.: negative percentage values mean ICON/MESSy-CLaMS has lower mixing ratio than MLS.

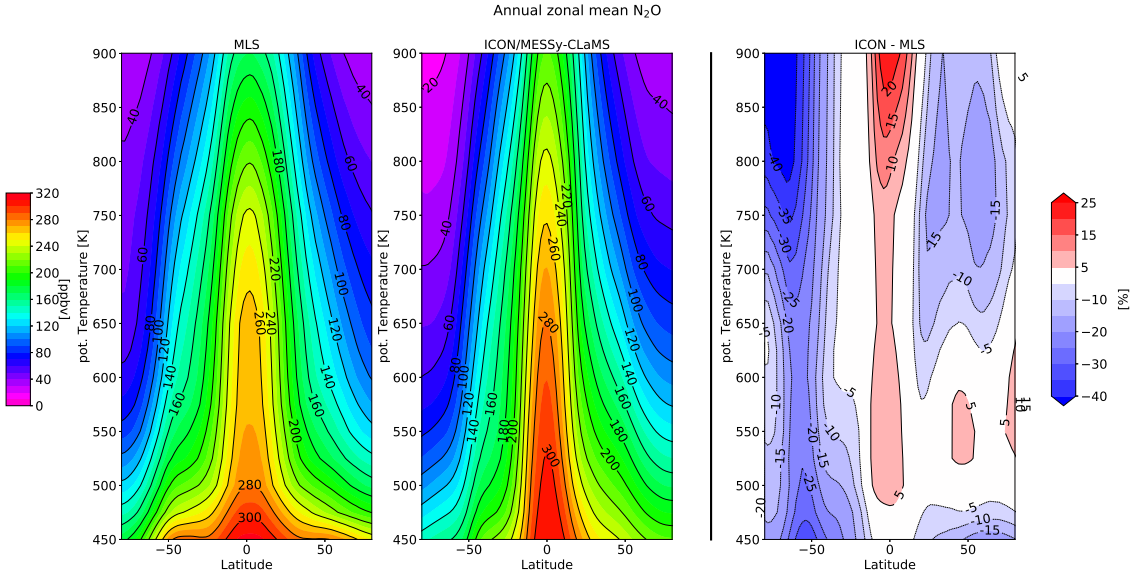

Figure 3.12: Zonal mean nitrous oxide volume mixing ratio for seasonal climatologies. MLS 2005-2017 climatology (left panel). Ten year ICON/MESSy-CLaMS simulation climatology (middle panel). Percentage difference, ICON/MESSy minus MLS divided by MLS (right panel): annual mean. Vertical range from 400 K potential temperature up to 900 K.

The annual zonal mean distribution of nitrous oxide is shown in Figure (3.12) in a latitude-potential temperature cross section. The mean state of the distribution of N_2O is quite similar to the observations in the stratosphere. The values range from over 300 ppbv in the lower stratosphere to less than 20 ppbv in the middle stratosphere. In the tropics enhanced distribution is evident reflecting persistent upwelling in both model and measurement results. In addition, the values of the simulation and the observations are similar within differences of plus 5 % - minus 15 % except smaller volume mixing ratios in the southern polar middle stratosphere. The model results show reduced mixing ratios by up to 40 %.

Further, the decline of nitrous oxide with altitude because of chemical loss at greater heights in the stratosphere is clearly visible. Also, while the model captures high mixing ra-

tios of nitrous oxide at lower altitudes the decline towards lower mixing ratios with altitude starts at lower altitudes (below about 450 K, ≈ 15 km) than observed. However, simulated nitrous oxide mixing ratios in the tropical pipe are larger than observed. In the tropics, *Jin et al.* (2009) compare models results of nitrous oxide in the stratosphere with satellite climatologies and conclude that MLS below 50 hPa (p > 50 hPa, < 490 K) and observe lower mixing ratio as in the model simulations. The meridional profiles of monthly zonal mean N_2O for April and October assessed by *Hegglin and Tegtmeier* (2017) conclude a negative bias in nitrous oxide compared to the multi instrument mean by 5 % to 10 % at 100 hPa not only in the tropics but along all latitudes. A study by *Froidevaux et al.* (2019) of the free running WACCM model (*Marsh et al.*, 2013) annual climatologies with MLS climatologies of the time period 2005- 2014 revealed percentage differences at 10 hPa of plus 5%-10% in the tropics and a negative model bias in the southern polar region of 10% up to 20 % (see Figure 5 in *Froidevaux et al.* (2019))

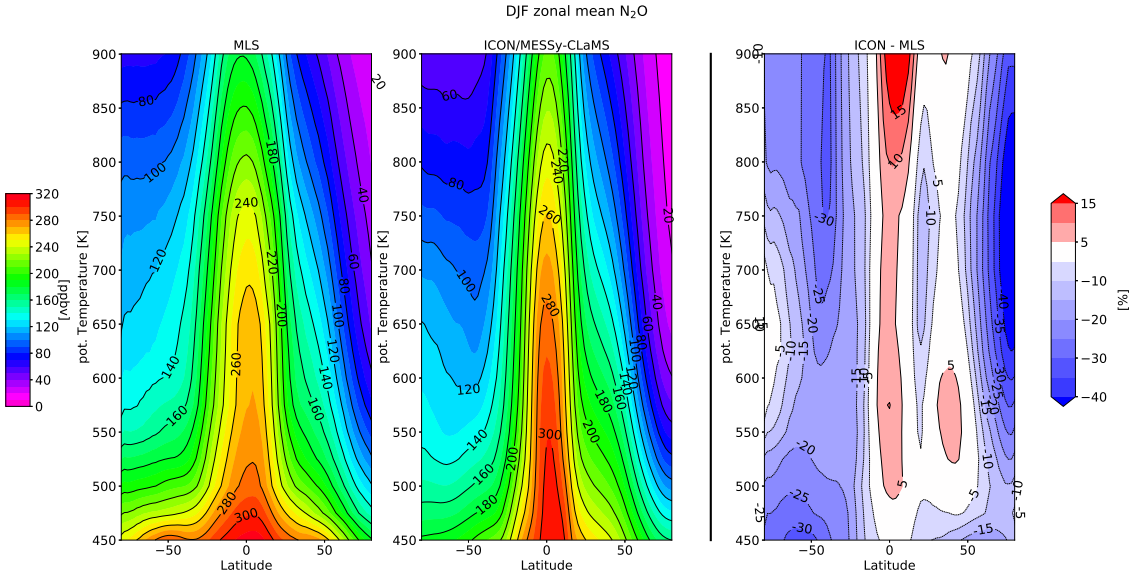

Figure 3.13: same as Figure 3.12 except for DJF season

In the DJF season the modeled volume mixing ratio of nitrous oxide by ICON/MESSy-CLaMS is in good agreement with differences by 5 % to 15 % in the tropics (see Figure 3.13). In the extratropics and polar regions of both hemispheres the differences are larger; up to 40 % in the northern hemisphere in the lower stratosphere. The volume mixing ratio in the model is reduced where downdraft is enhanced.

Figure 3.14 shows the nitrous oxide climatologies of the MAM season. The modeled vol-

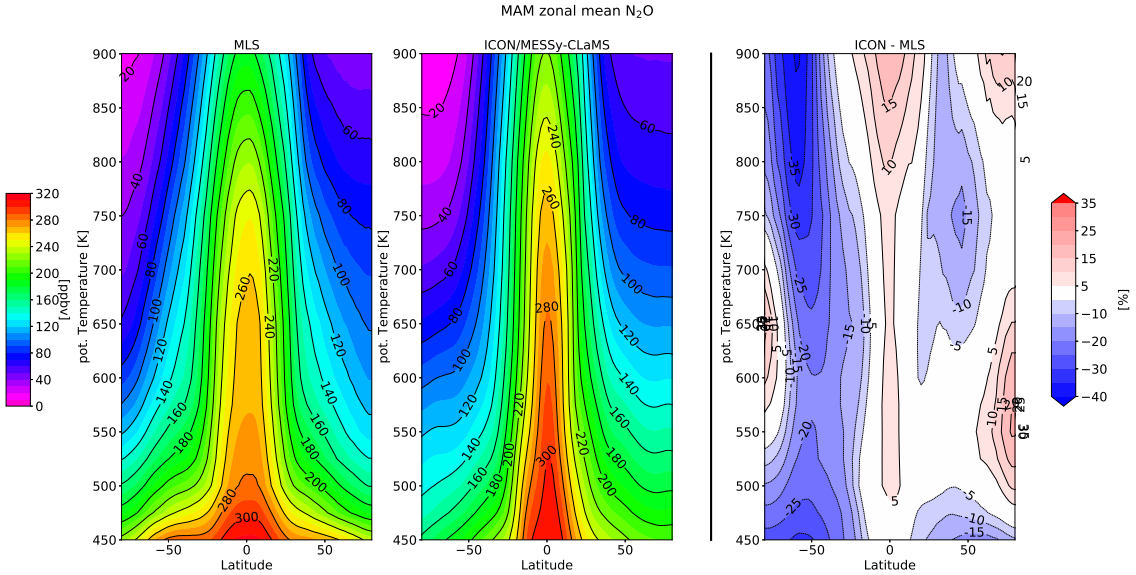

Figure 3.14: same as Figure 3.12 except for MAM season

ume mixing ratio is in good agreement with differences by -15 % to 15 % in the tropics and the northern hemisphere. The volume mixing ratio in the polar region is enhanced in the lower and middle stratosphere, where the values are reduced in mid-latitude middle and lowermost stratosphere. In the southern hemisphere differences up to 40 % are found.

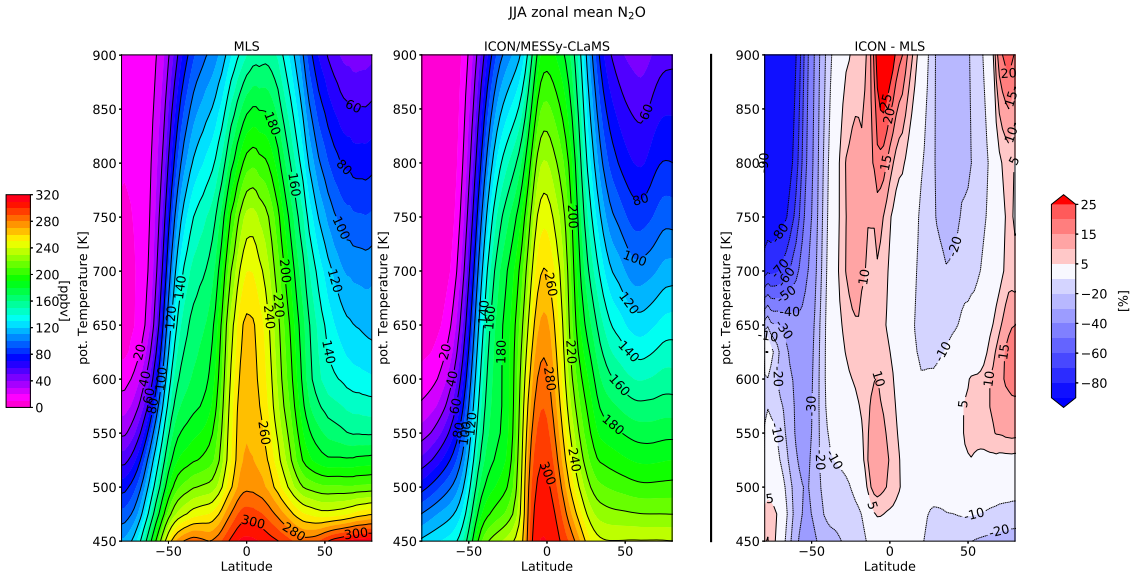

Figure 3.15: same as Figure 3.12 except for JJA season

In boreal summer and autumn the differences in the climatologies are most prominent in the southern hemisphere middle stratosphere and have comparable structures (see Figures 3.15

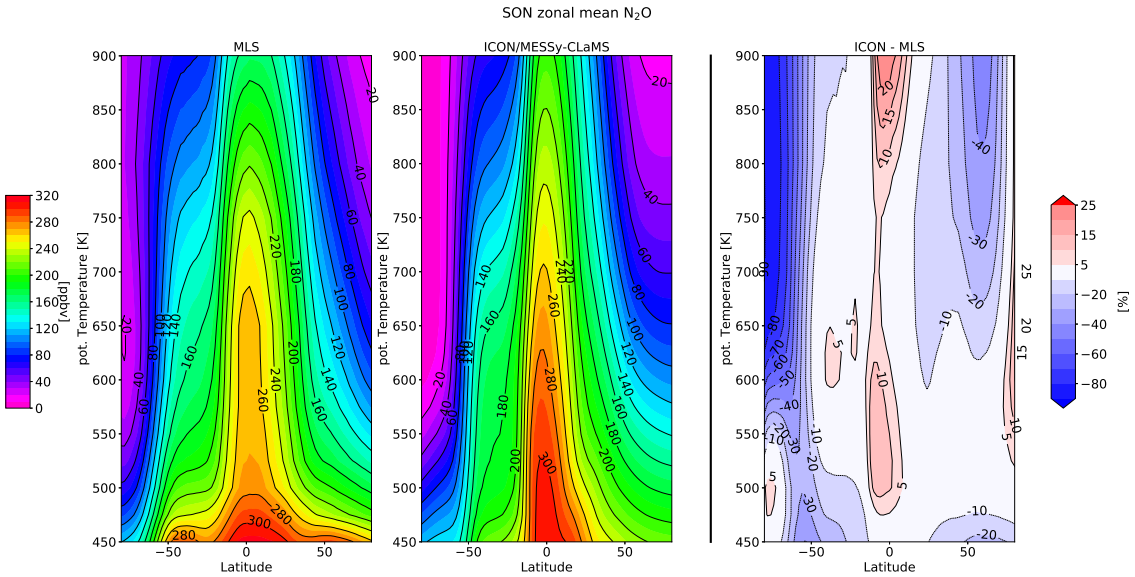

Figure 3.16: same as Figure 3.12 except for SON season

- 3.16). In the southern hemisphere very low (< 1 ppbv) volume mixing ratios are modeled and result in large percentage differences above isentropic level of 600 K. The lower stratosphere tropical volume mixing ratios are enhanced by 10 %. The volume mixing ratio in mid-latitude lower stratosphere in the southern hemisphere is reduced by 10 % to 30 %. In the northern hemisphere the volume mixing ratios in the polar region are enhanced in JJA and are reduced in SON. Upward transport of nitrous oxide mixing ratio in the tropical pipe and diabatic descent over the winter poles is seen in both, the simulation and the MLS observations. In the southern hemisphere in JJA (and SON season) the sub-tropics and sub-polar regions indicate strong horizontal gradients by closely spaced contours in MLS. The contour lines of 200 - 160 ppbv in MLS JJA are more elongated indicating a well mixed surf zone enclosed by sub-tropics and sub-polar. The surf zone is more prominent in MLS JJA than in the model results. *Jin et al.* (2009) conclude for the fall season at high latitudes above 10 hPa (≈> 830 K) a positive bias relative to ACE-FTS. *Jin et al.* (2009) concludes that, the volume mixing ratios of MLS climatologies in SON season above 830 K in the southern hemisphere polar region are overestimated. The volume mixing ratio modeled in ICON/MESSy-CLaMS in the same region are lower by up to 80% than in MLS climatologies. This negative model bias is expected to be reduced in comparison to other satellite observation climatologies. Nevertheless, the analysis of the transport barrier in chapter (5) focuses on the isentropic levels between 450 K and 600

K. Moreover, this negative model bias is seen and discussed from a statistical perspective in chapter (4). The descending branch of the Brewer-Dobson circulation is diagnosed by the seasonal variation of the zonal mean composition of air masses. Within this diagnosis of the seasonal zonal mean distribution, the net effect of multiple transport processes is assessed rather than one particular transport process. The ICON/MESSy-CLaMS model results represent a good balance between the horizontal transport of mid-latitude air and the longer transport process by descending of upper stratospheric air.

3.2.1 Isentropic Cross Sections

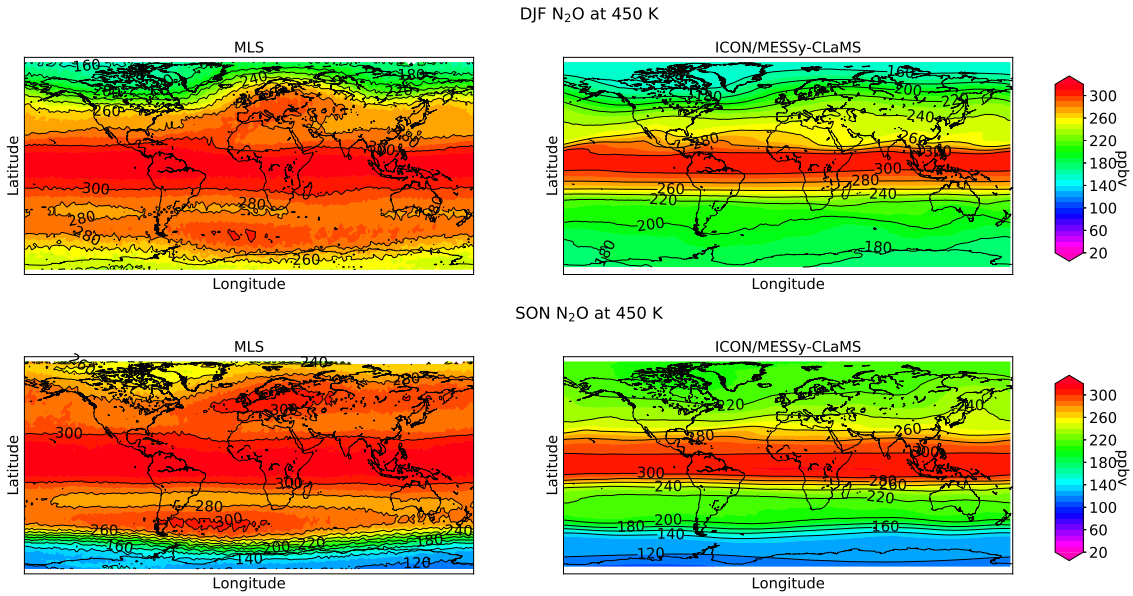

Figure 3.17: Nitrous oxide volume mixing ratio for seasonal climatologies. MLS 2005-2017 climatology (left panels). Ten year ICON/MESSy-CLaMS simulation climatology (right panels): DJF seasonal mean in the top row. SON seasonal mean in the bottom row: 450 K potential temperature

The climatologies of the model results are compared to MLS climatologies on four specific isentropic level, i.e. 450 K, 500 K, 550 K, and 600 K. In an isentropic cross section, distinct features like the latitudinal expand of the tropical band or the transport barrier in the sub-polar regions, can be discussed specific for that isentropic level. The results are shown in Figures (3.17 - 3.21), where DJF season is shown in the top panels and SON season in the bottom panels.

On the isentropic level of 450 K (see Figure 3.17) the tropical band with volume mixing ratios ≥ 300 ppbv is broader extended in the results of MLS climatologies. In addition, high volume mixing ratios of 260 - 280 ppbv are distributed to sub-polar regions, from the Antarctic to northern Europe. This results is seen in seasonal mean in DJF and SON. On the contrary, the model results show a narrow tropical band and intermediate volume mixing ratios of 180 - 220 pbbv in the southern hemisphere in DJF. In the northern hemisphere the contour lines of 240 - 260 ppbv extend to mid-latitudes region. In boreal autumn mid-latitude volume mixing ratios are 40 ppbv lower in the model results. The low concentration of nitrous oxide in the southern hemispheric polar region are comparable. The polar vortex edge is shifted to the tropics in the model results. The striking differences in the large extension of high volume mixing ratios, which is not prevalent in the model, and the reasons for this need to be considered in further model development.

In Figure (3.19) the extension of the tropical band in the model is comparable with the MLS climatologies in both seasons. However, the the maximum volume mixing ratios in the model are slightly higher. The southern hemispheric volume mixing ratios in DJF are lower by 40 - 60 ppbv than in the MLS observations. The concentration of nitrous oxide in the mid latitudes in the northern hemisphere are comparable in both seasons. In the MLS observations, the edge of the polar vortex shows more zonal fluctuations than the simulation.

The differences in the results of DJF southern hemispheric and the tropical band that have been described for the isentropic level of 500 K are prevalent at the isentropic level of 550 K and 600 K. The model results show lower volume mixing ratios in DJF southern hemisphere and higher volume mixing ratios in the tropical band. The northern hemispheric chemical distribution of nitrous oxide is comparable in both seasons as well as the southern hemispheric SON volume mixing ratios. *Pommrich et al.* (2014) conducted analysis of CO with a comparison of MLS climatologies, where the anomalies of CO distribution are overestimated in CLaMS climatologies at the isentropic level of 390 K. This feature is reproduced in the present study and unclear at this point. The statistical analysis in chapter (4) gives a first insight for a potential cause. However, future studies should include simulation setup to investigate the reasoning of this feature.

The air masses in the polar region in the southern hemisphere differ from the mid-latitude air masses in SON season (see bottom panels in Figures 3.17 - 3.21). This feature is clearly visible by the sharp transition from green to blue or violet contour lines. The volume mixing ratios are rapidly decreasing from intermediate (200-180 ppbv) to low volume mixing ratios (120-80 ppbv). The transport barrier in the sub-polar vortex edge in the southern hemisphere is evolving in different isentropic levels and separates the air masses. The gradient in the chemical distribution of nitrous oxide along the latitudinal direction is a measure of the strength of the transport barrier. To what extend the strength of the transport barrier can be quantified, is object of an analysis in chapter (5).

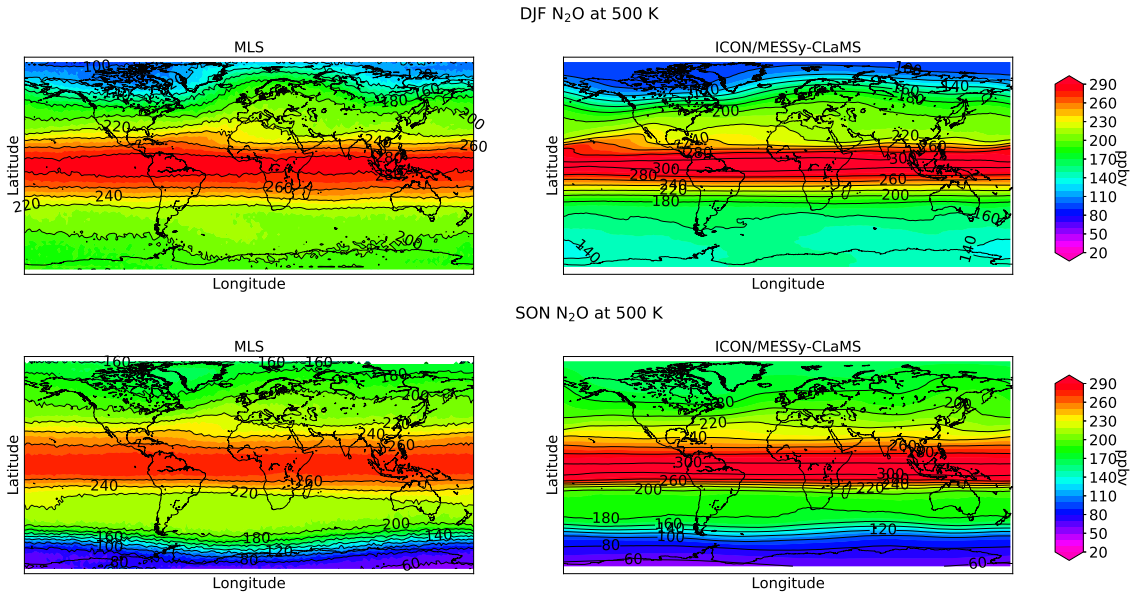

Figure 3.18: same as Figure 3.17 except for: 500 K potential temperature

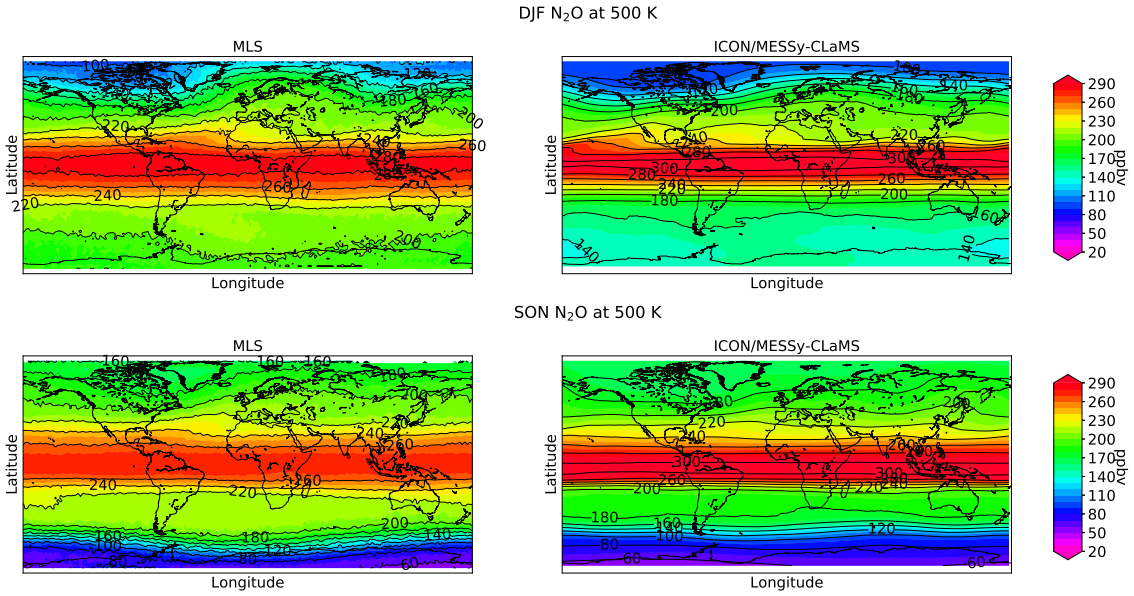

Figure 3.19: same as Figure 3.17 except for: 500 K potential temperature

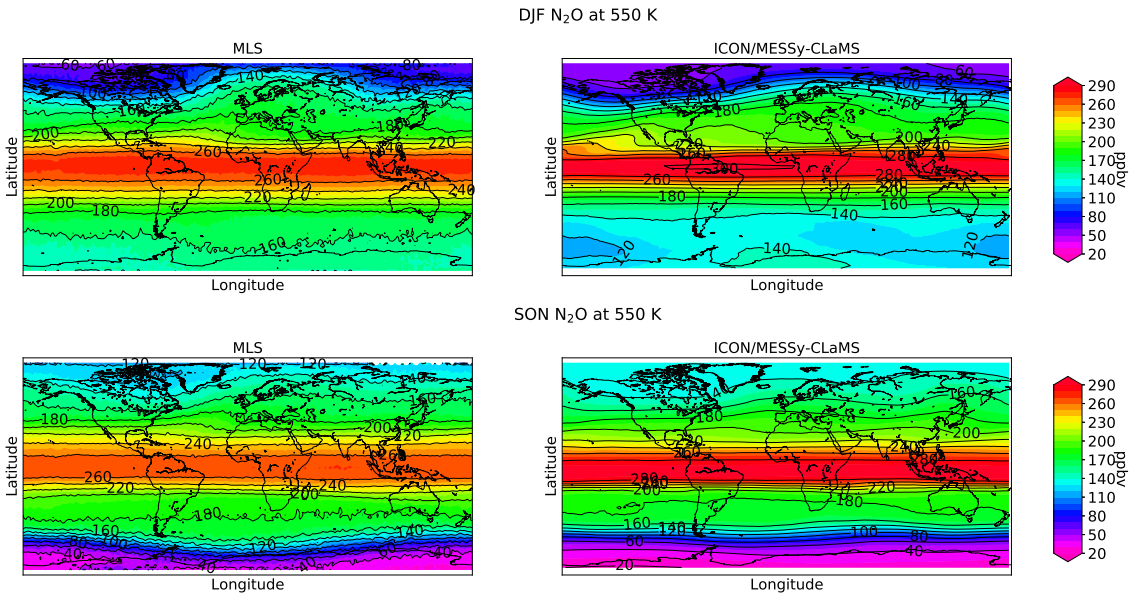

Figure 3.20: same as Figure 3.17 except for: 550 K potential temperature

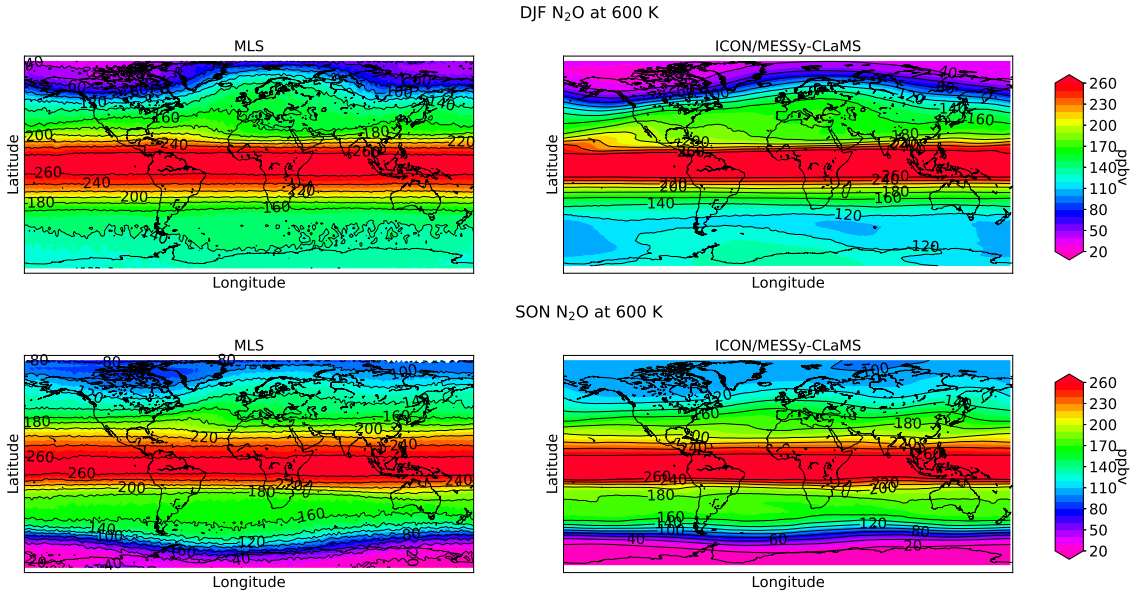

Figure 3.21: same as Figure 3.17 except for: 600 K potential temperature

3.3 Annual mean climatologies of trace gases

The used simplified chemistry simulation setup (*Pommrich et al.*, 2014) does contain other trace gas species besides nitrous oxide. The annual zonal mean climatologies of water vapor, methane, CFC-11 and ozone are shown in Figure (3.22). In the lower stratospheric southern hemispheric polar region, the dehydration in the cold winter polar vortex produce low volume mixing ratios of water vapor. Air masses in the tropical pipe entering the stratosphere are dehydrated at the cold tropical tropopause. The zonally averaged annual mean of water vapor (top left panel Figure 3.22) resembles the main features found in Multi Instrument Mean climatologies by (*Hegglin and Tegtmeier*, 2017), satellite observations (*Grooß and Russell*, 2005) as well as other studies conducted with CLaMS (*Riese et al.*, 2012). With a long lifetime of about 44.7 years (*Minschwaner et al.*, 2013), CFC-11 is expected to be distributed uniformly in the tropical tropopause layer. The updraft in the tropical pipe produces a maxima of CFC-11 mixing ratios in the tropics. With increasing altitude the mixing ratio of CFC-11 is decreasing (see bottom left panel Figure 3.22). The structure of the chemical distribution of methane, as a well mixed tropospheric source gas, is comparable to nitrous oxide. The mixing ratio decreases with increasing altitude and with local maxima in the tropical pipe (top right panel Figure 3.22). The ozone mixing ratio above 500 K potential temperature is prescribed

by HALOE climatologies (*Grooß and Russell*, 2005) in the simulation setup, nevertheless are shown here for reasons of completeness. The high ozone volume mixing ratio in the middle stratosphere is resembles the HALOE concentrations as expected (bottom right panel Figure 3.22).

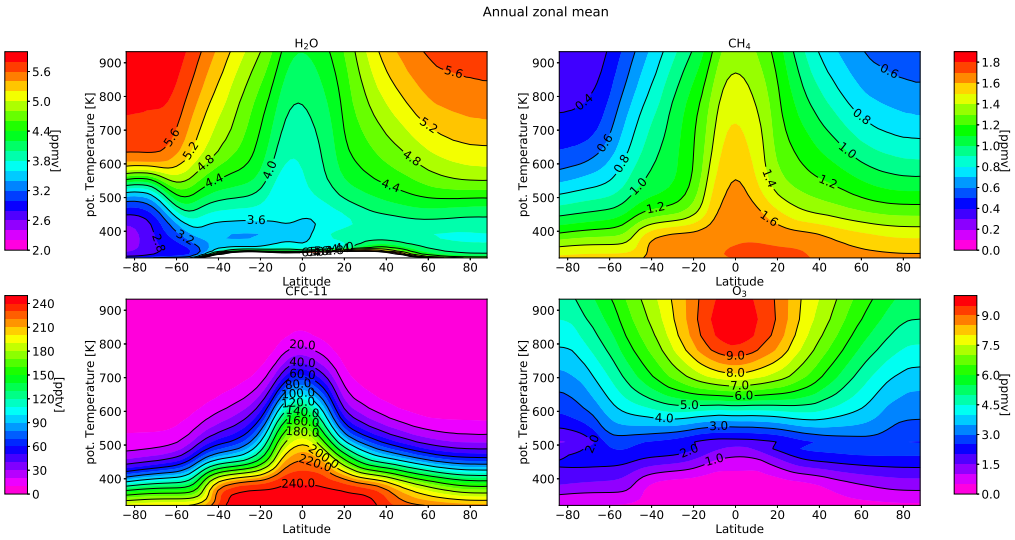

Figure 3.22: Annual zonal mean climatologies of H_2O, CH_4, CFC_{11} and O_3 of ICON/MESSy-CLaMS simulations

Chapter 4

Air Mass Separation in Simulations and Observations

4.1 Probability Distribution Function in Latitude Bands

Data sets of atmospheric quantities, obtained by in-situ observations, satellite measurements or modeled data by simulations can conduce to an analysis from a statistical perspective. The volume mixing ratio of a chemical species is a suitable atmospheric quantity as object of a statistical analysis. The methodology is introduced in large extent by *Sparling* (2000) and used to determine transport and transport barrier in the stratosphere by many other studies, e.g.: (*Shepherd*, 2002; *Bönisch et al.*, 2011; *Ploeger et al.*, 2015) as well as an objective to evaluate Chemistry-Climate Models (*SPARC*, 2010). The probability p to measure a volume mixing ratio r within a latitude band L is defined as follows:

$$p_{L,\zeta}(r) = \sum_{i \in L} p_{[i:i+2],\zeta}(r) \times w_i \quad , \tag{4.1}$$

where L is here a set of latitudes $[lat\_min, lat\_min + 2, ..., lat\_max]$ with increment chosen to be two degrees. The probability p is area weighted with w_i. The area-weight counts a procedural factor corresponding to the proportion that the latitudinal band encompasses in relation to the considered area of the earth atmosphere. The weighting factor therefore inherently incorporates problems with oversampling of MLS satellite observations around the

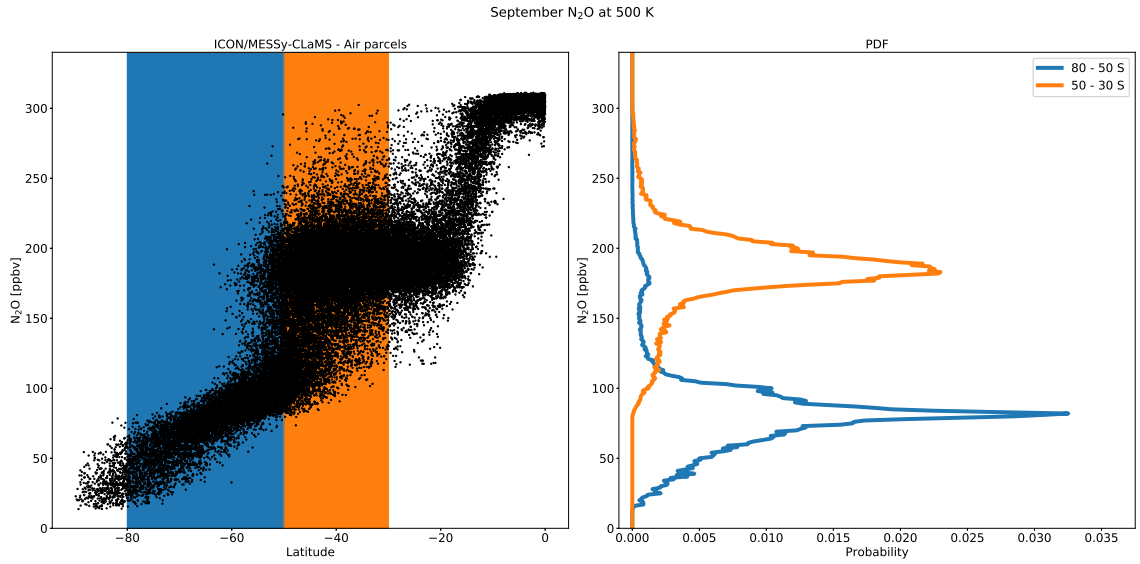

Figure 4.1: Scatter plot of N_2O volume mixing ratio versus latitude of modeled air parcels by ICON/MESSy-CLaMS in September at potential temperature of 500 K. Latitude bin of 80°to 50°S is shaded in blue. Latitude bin of 50°to 30°S is shaded in orange (left Panel). Within the latitude bin a PDF is calculated and the probability is shown versus the volume mixing ratio accordingly (right panel). The color code indicates the latitude bin of the left panel.

pole.

Since MLS satellite observations can not considered to be uniformly distributed over the hemisphere but oversample around the turning point one has to consider weighting according to the latitudinal area covered by the measurements. This area weighting factor is also applied to the modeled CLaMS air parcels. The CLaMS air parcels are distributed uniformly but nevertheless occupy different amount of total area within the atmosphere which are applied to the same weighting factors. With equation (4.1) a probability distribution function (PDF) can be calculated for different sets of latitudes L of the atmospheres. The PDFs used in this section are calculated for the chemical species nitrous oxide for volume mixing ratios from $[0, 1, ..., 350]$ with increment chosen to 1 ppbv.

Probability distribution functions are calculated for different months and different isentropic levels for measured MLS satellite data of the year 2005 and modeled nitrous oxide tracer of CLaMS. With the individually calculated PDFs one can assess how likely concentrations of nitrous oxide are measured or modeled in the specified atmospheric air mass. A statistical perspective can determine to what extent the air masses are separated in chemical composition. Figure (4.1) shows a schematic how the PDF of two different latitudinal bands are connected

to a scatter plot of data points in a volume mixing ratio on the y-axis and latitude on the x-axis.

In the left panel of Figure (4.1), modeled air parcels for the month September are shown in a scatter plot for the southern hemisphere. There are two latitudinal bands highlighted with color shades in the background. One latitudinal band from 30°to 50°S in orange and one for the latitudinal band of 50°to 80°S highlighted in blue. The corresponding PDFs are shown in the right panel color coded according to the latitude bands in the left panel. The air masses in the mid-latitude band from 30°to 50°S in this case at isentropic level of 500 K contain most likely nitrous oxide with a volume mixing ratio of about 186 ± 15 ppbv. There is a small likelihood for nitrous oxide with a volume mixing ratio in the range of 100 to 150 ppbv. The air masses in the latitude band from 50°to 80°S contain most likely nitrous oxide with a volume mixing ratio of about 79 ± 9 ppbv. The main peaks of the PDFs are distinct in volume mixing ratio. The air masses of both latitudinal bands can be considered distinct in chemical composition and can be attributed to mid-latitude air masses and polar region air masses, respectively. The separation of both PDFs can therefore conduce to an understanding of the separation of mid-latitude from polar region air masses. Specifically, by the differentiation between different latitude bands one can clearly see that the PDF in one specific latitude band contains a single peak structure. For the case of a wider latitude region, probabilities of both single peaks accumulate to a double peak structure. A priori, one cannot know if the double peak structure consists of two single peaks or two double peaks. Therefore an understanding of the separation is necessary beforehand. In the following sections the distribution of nitrous oxide in the Antarctic polar region is analyzed for the month of September in different isentropic level in the same way as discussed.

4.2 September Regional PDF

Probability distribution functions of MLS observational data points in September 2005 are calculated in the way described in section (4.1) at four different isentropic levels; 450 K, 500 K, 550 K and 600 K for the southern hemisphere individually. CLaMS modeled air parcels of ten simulated September months are accumulated for one conjunct data set of September. In Figures (4.2 and 4.3) the resulting PDFs for different isentropic levels are shown. In the left

panel the PDFs of MLS data on the specific level are shown, whereas on the right panel the modeled air parcels by CLaMS.

There is a wide range of medium probability to measure volume mixing ratio from about 80 ppbv to 310 ppbv in September measurements of MLS at 450 K in the latitudinal band of 80°to 50°S, whereas in the latitudinal band of 50°to 30°S, there is a distinct probability to measure volume mixing ratios between 250 ppbv and 310 ppbv (left panel, Figure 4.2).

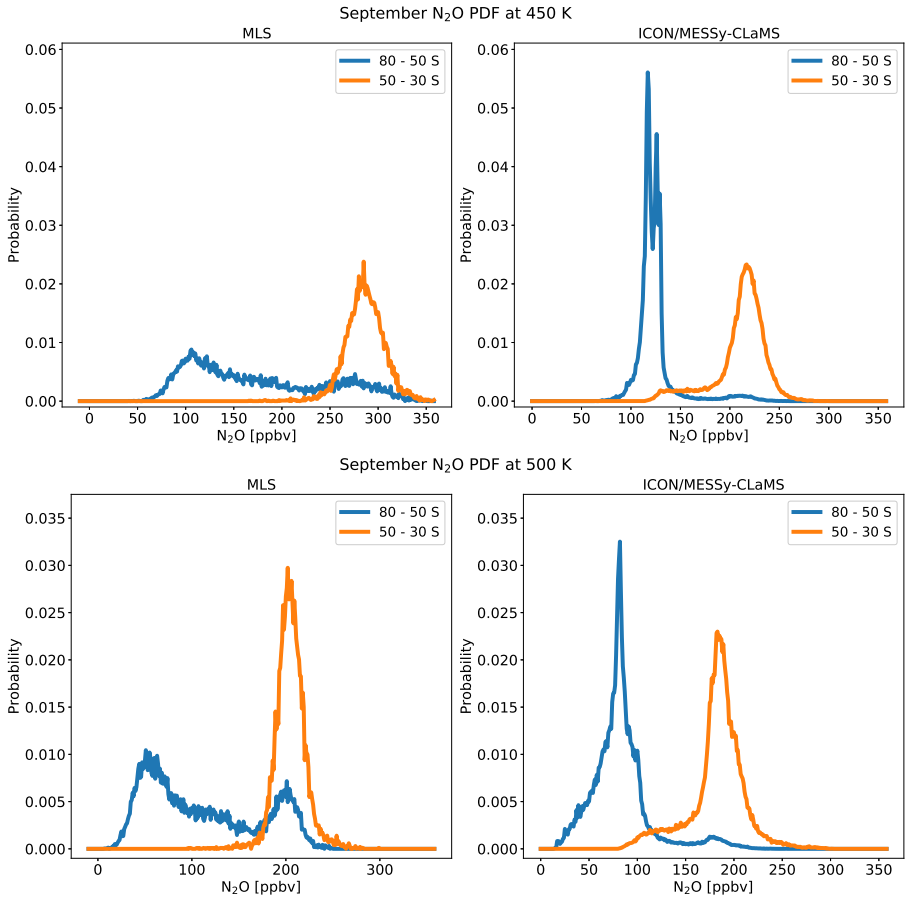

Figure 4.2: PDF of N_2O volume mixing ratio versus latitude in 80°to 50°S in blue. PDF in 50°to 30°S in orange. MLS 2005 (left panel). ICON/MESSy-CLaMS (right panel): September at potential temperature of 450 K (top) 500 K (bottom).

There is a separation of high probability between the two latitudinal bands in the modeled CLaMS data (right panel, Figure 4.2). Both PDFs show a single peak structure for either mid-latitude air masses with high volume mixing ratios as well as low mixing ratio values for polar region air masses. Compared to MLS, the modeled air masses in the polar vortex region show much higher probability of volume mixing ratios of around 100 to 120 ppbv. The location of

the maximum peak in the mid-latitude air at 280 ppbv in MLS data is shifted to lower volume mixing ratio in CLaMS to 220 ppbv. The probability to measure mid-latitude air masses in the latitudinal band of 50°to 30 °S is comparable in MLS as in CLaMS.

At 500 K isentropic level there is a single peak structure with a rather sharp peak around 200 ppbv in the mid-latitude band for MLS (left panel, bottom, Figure 4.2). Air masses in the mid-latitudes in CLaMS contain high amount of air masses with volume mixing ratio of around 200 ppbv with a small probability to model air parcels 100 - 150 ppbv as well (right panel, bottom, Figure 4.2). The peak in the polar region overestimates the amount of low mixing ratio air masses in CLaMS compared to MLS. The air masses in the polar region in MLS for September 2005 contain air with volume mixing ratios of 200 ppbv. Looking at the higher levels, 550 K and 600 K (Figure 4.3), the separation of air masses between the polar region latitude band and the mid-latitude band is captured in the peak structure of the PDFs. The PDFs show a consistent single peak structure in the mid-latitude band for MLS as well as CLaMS. There are partially air masses in the polar region with higher volume mixing ratio, although the probability is lower compared to the low mixing ratio values. At 600 K, shown in the bottom of Figure (4.3), CLaMS strongly overestimates the probability to measure volume mixing ratio below 50 ppbv.

4.2.1 Regional PDF in August, October and November

An equivalent analysis is done for the months of August, October and November. Figures of the PDFs are shown in Appendix A (6). Throughout the months from August to November the PDFs of the mid-latitude band show a single peak structure in all considered levels (450 K, 500 K, 550 K, 600 K). This feature is displayed in MLS monthly datasets as well as in modeled CLaMS air parcels. CLaMS mid-latitude air masses have a low probability to measure volume mixing ratio of about 100 to 150 ppbv. The polar vortex air masses in MLS display a broad range of probability to measure low values from 50 ppbv to higher values of 200 ppbv for August. In the next months, September and October a double peak structure develops with roughly the same probability to measure the polar vortex peak with low volume mixing ratio at around 50 ppbv and the mid-latitude peak with high volume mixing ratio of around 200

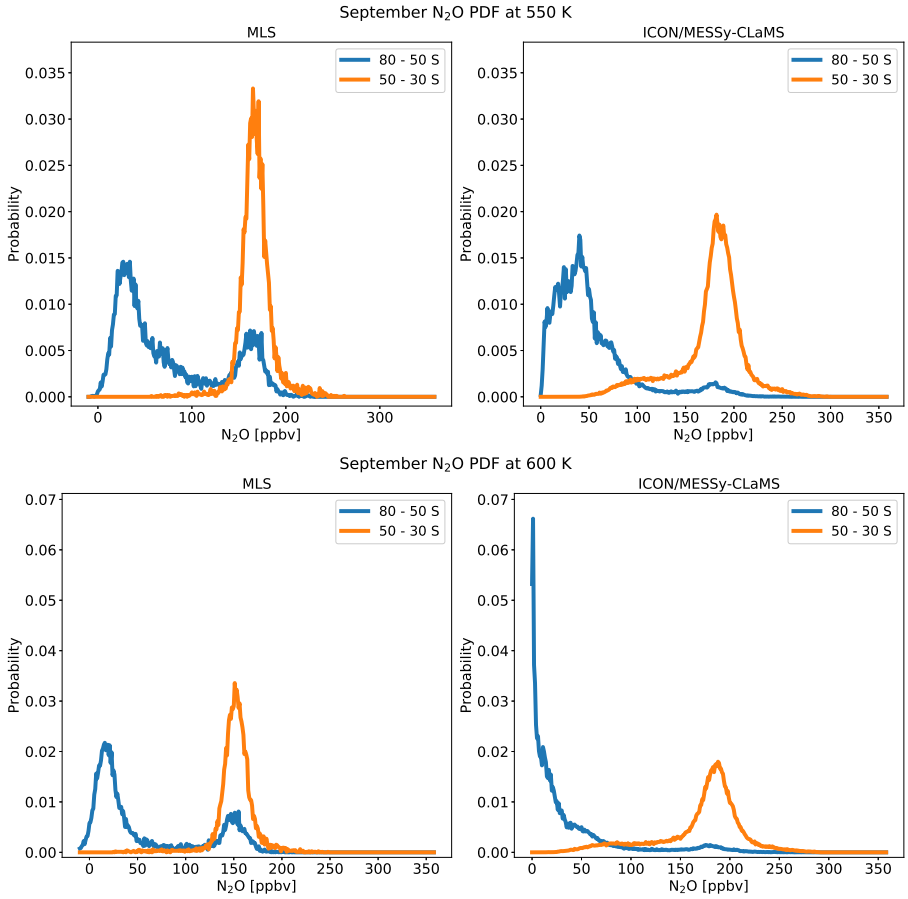

Figure 4.3: as 4.2 but for potential temperature of 550 K (top) 600 K (bottom).

ppbv. In November the double peak feature favors higher volume mixing ratio in the upper stratosphere. The polar vortex starts to break earlier at higher altitudes. The mid-latitude peak of CLaMS is in good agreement with MLS peak with a slightly underestimation in probability in CLaMS. The polar vortex peak is overestimated in CLaMS for the isentropic levels 450 K, 500 K, and 600 K. At 550 K level the low volume mixing ratios are in good agreement for August, September and October. In November the double peak structure has a higher probability to measure mid-latitude air masses in MLS, where in CLaMS the low volume mixing ratios have a higher probability. Overall the regional PDFs show a consistent picture throughout the months. On the one hand, a clear separation of mid-latitude and polar region air masses but on the other hand an overestimation of low volume mixing ratio in polar region by modeled CLaMS air parcels.

4.3 Combined SH PDF from August to November

The PDF considered in this section contains data sets from both latitudinal bands, 80°to 50°S and 50°to 30°S, combined. Therefore the PDF is calculated in the band from 80°to 30°S. The single peak structure from two different latitudinal band PDFs combine to a double peak structure. As mentioned in section (4.1), the knowledge of the separation of the probability into both latitude bands is a priori not necessarily known. The combination of both latitude bands allow for a more comprised picture of the air mass separation through out the months. With the knowledge of section (4.1), a direct comparison of calculated PDFs for MLS data with the CLaMS modeled air parcels is more enhanced. mid-latitude and polar vortex air masses can contribute to all volume mixing ratios in the PDF and might broaden the double peak structure.

In Figures (4.4 - 4.7) the PDFs are shown for the month from August to November at four different isentropic levels; 450 K, 500 K, 550 K and 600 K. The black lines denotes the PDF from 80°to 30°S for the CLaMS modeled air parcels. The red line denote the data set of the corresponding month of the year 2005 of the MLS data. At 450 K the peak corresponding to mid-latitude air mass for MLS is around 290 ppbv during the month from August to November (see Figure 4.4). The polar vortex air mass peak is not prominent in the month of August and September and evolving during October and November. In the CLaMS modeled nitrous oxide the separation between the air masses is prominent during all months, where the peak for the mid-latitude air mass is shifted to lower volume mixing ratio at around 220 ppbv. The probability peak for the vortex air masses is overestimated. At 500 K the mid-latitude air mass of modeled CLaMS nitrous oxide is in good agreement with the measurements of MLS. However, the lower volume mixing ratio peak for the polar vortex air mass is slightly overestimated in CLaMS (see Figure 4.5). The double peak structure is well captured in the isentropic level of 550 K in MLS and in CLaMS (Figure 4.6). At 600 K during August and September (Figure 4.7) the low volume mixing ratios are strongly overestimated in CLaMS. The number of air masses with higher volume mixing ratio is increasing and the amount of low mixing ratio is decreasing during October and November. The same is true for MLS, although the double peak structure is slightly shifted to lower volume mixing ratios of N_2O.

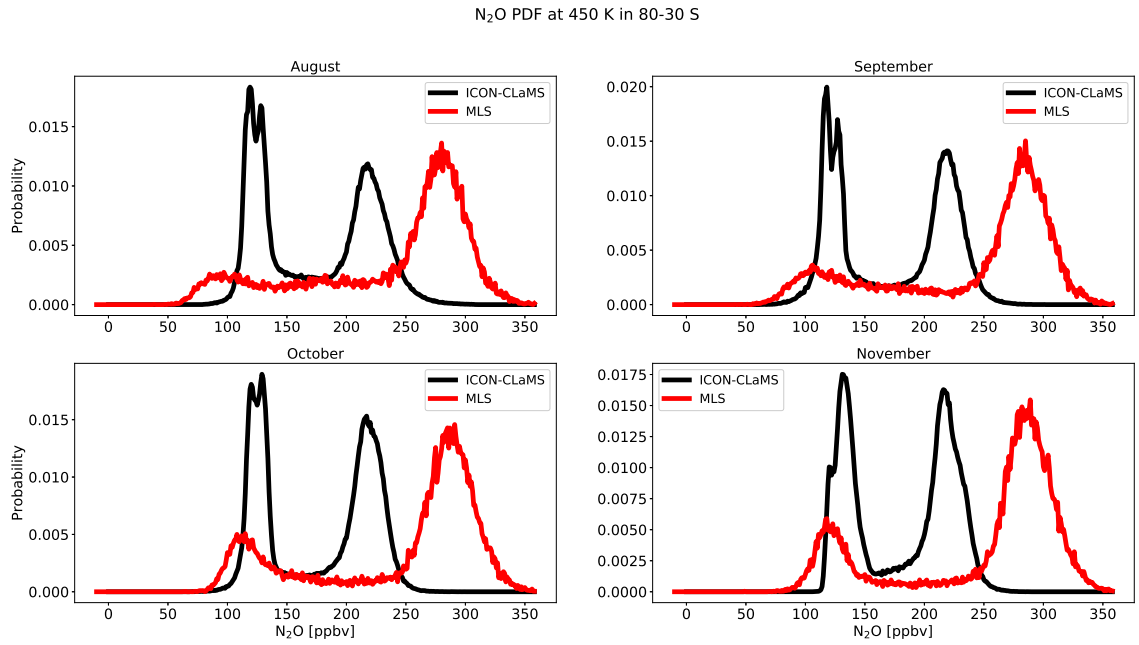

Figure 4.4: PDF of N_2O volume mixing ratio versus latitude in 80°to 30°S. PDF of MLS data marked in red. Modeled ICON/MESSy-CLaMS air parcels marked in black. The different panels show different month: All panels show potential temperature of 450 K.

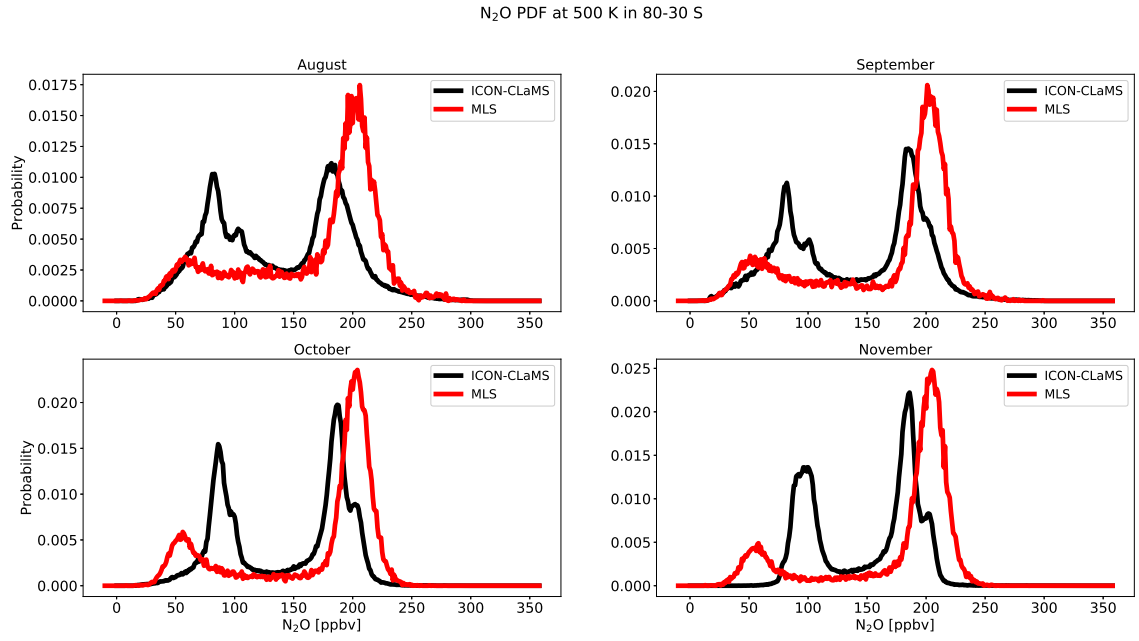

Figure 4.5: as Figure 4.4 but for potential temperature of 500 K.

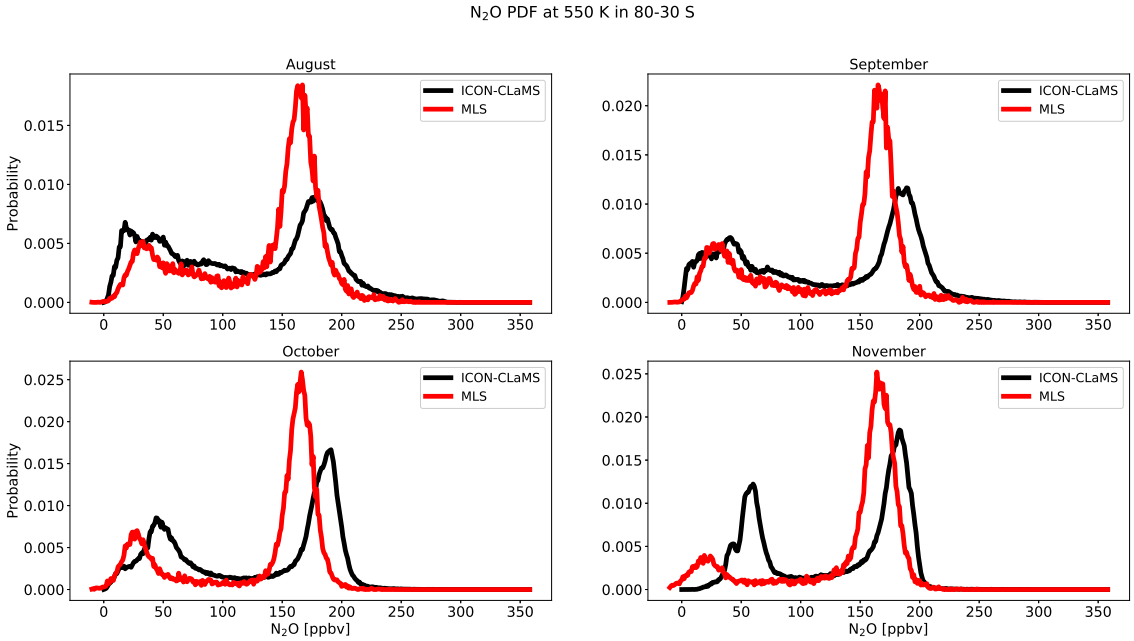

Figure 4.6: as Figure 4.4 but for potential temperature of 550 K.

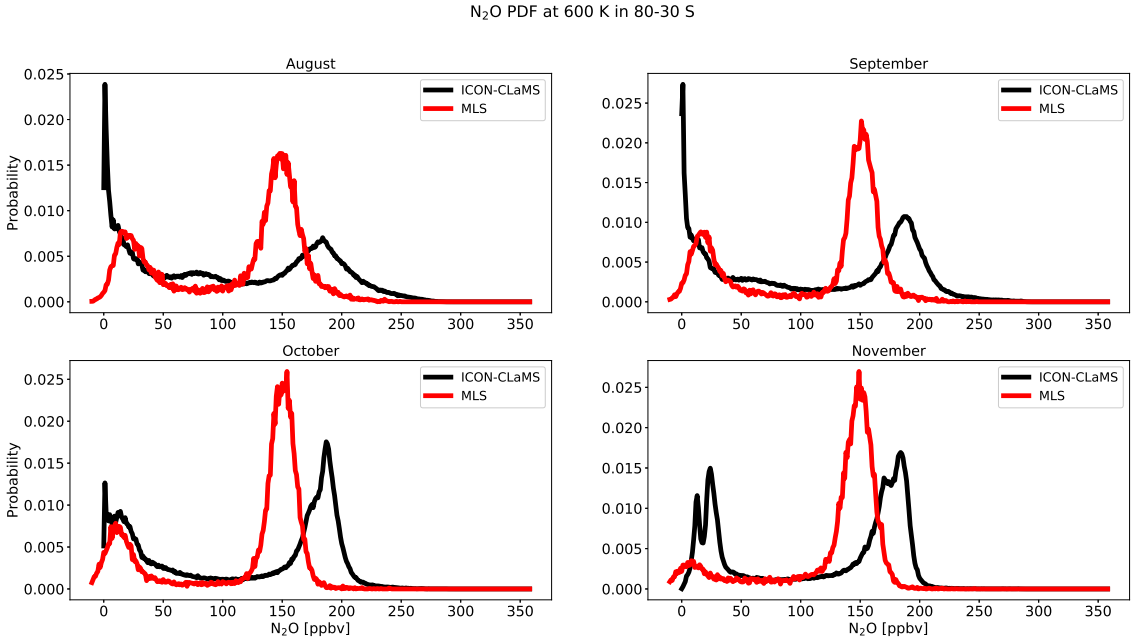

Figure 4.7: as Figure 4.4 but for potential temperature of 600 K.

4.4 From Air Mass Separation to Transport Barrier

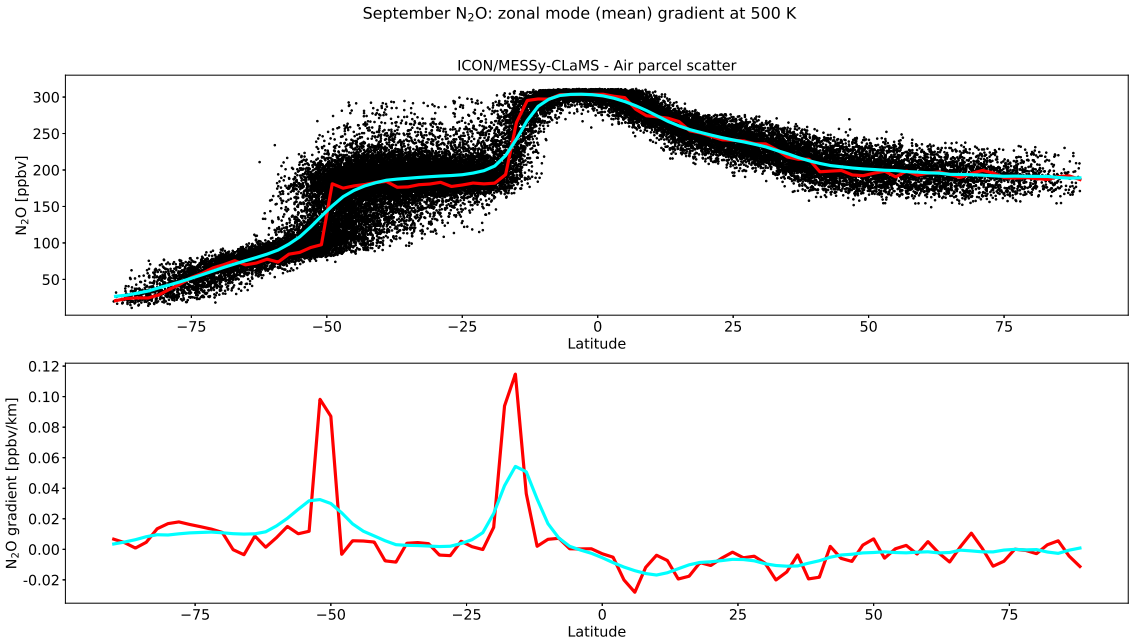

Figure 4.8: Scatter plot of N_2O volume mixing ratio of air parcels in both hemispheres modeled by ICON/MESSy-CLaMS in September at potential temperature of 500 K. For each latitude bin of two degrees the mean value of volume mixing ratio is calculated (top panel cyan colored line). Highest probability volume mixing ratio (zonal mode) calculated from the PDF in the two degrees latitude bin (top panel red colored line). Bottom panel: Gradient in latitudinal direction of the zonal mean and zonal mode of nitrous oxide.

Displaying monthly observational MLS or modeled CLaMS data points with volume mixing ratio of nitrous oxide versus latitude in a scatter plot on one isentropic level visualizes the separation of air masses in the polar region and mid-latitude surf zone, as discussed in the previous sections. In addition, the PDF enables to determine the transport barrier between the separated air masses. The concept of zonal mode is introduced by *Sparling* (2000). The zonal mode envisions the transport barrier, especially the gradient of the zonal mode.

The zonal mode is defined within a specified latitude band by the volume mixing ratio with the highest observed or modeled probability of the PDF. In the following analysis the zonal mode is calculated consecutively for latitude bins of two degrees for both hemispheres. The resulting zonal mode is displayed in red colored line and overlayed on the scatter plot of the CLaMS modeled air parcels (Fig. 4.8) and observed MLS data points (Fig. 4.9). The cyan colored line represents the zonal mean volume mixing ratio of N_2O within the two degree

latitude band. In the bottom panel the meridional gradient of the zonal mode and zonal mean is calculated.

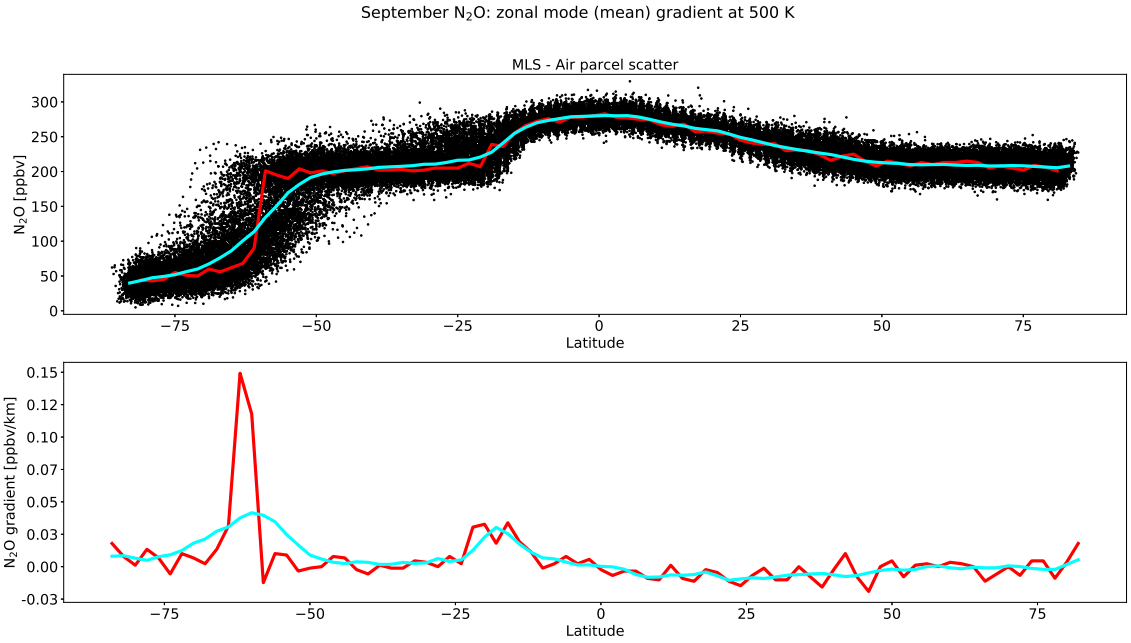

Figure 4.9: Same as Figure (4.8) but for MLS N_2O observations in September 2005 at potential temperature of 500 K.

In Figure (4.8) the scatter plot for CLaMS air parcels in September on the 500 K isentropic level is shown for nitrous oxide. In the southern hemisphere at around 50°S a steep gradient envisions the location where the air masses of polar vortex and mid-latitudes are separated and where the edge of the polar vortex is located. The gradient is defined positive in the direction from South Pole to North Pole. In Figure (4.9) the observational data points of MLS for September 2005 are shown at isentropic level of 500 K.

The statistical analysis in terms of binning latitudinal bands to a probability distribution function allows differences to be quantified in chemical concentration of air masses in a predefined time frame as well as altitude, respective isentropic level. The modeled chemical concentration of nitrous oxide with simulations of ICON/MESSy-CLaMS capture the separation of mid-latitude air masses from polar air masses. The probability to model low volume mixing ratios of nitrous oxide in the polar region is overestimated at isentropic levels of 450 K, 500 K and 600 K compared to the observations in MLS. At 550 K CLaMS modeled air parcels capture the probability to measure low volume mixing ratios in the polar region compared to

MLS observations. The modeled volume mixing ratio of N_2O for the mid-latitude air masses is underestimated at the isentropic level of 450 K but overestimated for the isentropic level of 600 K. The probability of low volume mixing ratios is strongly enhanced in CLaMS in the polar region latitude band at 600 K and above, whereas in MLS the probability is lower. The strongest gradient of the zonal mode displays the edge of the polar vortex at 500 K September for ICON/MESSy-CLaMS at around 50°S. In contrast the edge of the polar vortex in MLS is closer to the pole at around 60°S.

Within the polar region of 80°S - 90°S air parcels are simulated with volume mixing ratio of < 10 ppbv. The calculation of the PDF is area weighted and accounts for oversampling around the polar region. Nevertheless the PDF at isentropic levels of 600 K and above are skewed with high probability to very low volume mixing ratios. The seasonal diabatic descent in JJA in the region 80°S - 90°S is overestimated by 30 % - 60 % in the isentropic levels of 1250 K - 2500 K (see Figure 3.9) and might induce very low mixing ratio of the CLaMS model top (2500 K) chemical boundary conditions down to isentropic levels of 600 K. The analysis of the transport barrier in the next chapter (5) focuses on the isentropic levels between of 450K and 550K, due to the fact of the overestimation of the low volume mixing ratios at isentropic levels of 600 K and above compared to PDF conducted by MLS observations.

The higher probability of modeling lower mixing ratios in the polar region in modeled ICON/MESSy-CLaMS nitrous oxide resembles the lower volume mixing ratios in the seasonal zonal mean analysis and the seasonal distribution on isentropic cross sections in section (3.2.1). The ICON/MESSy-CLaMS model simulates a larger extension of the polar region. With the PDF analysis concentrated to polar region of 80°S to 50°S, the absolute amount of air parcels with lower mixing ratios within this region is higher. In addition, the stronger descent in the upper stratospheric southern hemisphere polar region contributes more lower mixing ratio air parcels to the PDF.

In future studies the analysis of the model top boundary conditions may contribute to a better understanding of this effect. The model results show a narrow tropical band at the isentropic level of 450 K, whereas the MLS climatologies show a wide distribution of high volume mixing ratios of nitrous oxide (see Figure 3.17). This feature is also seen in the statistical

analysis. The PDFs of the MLS observations at 450 K show a peak at higher volume mixing ratios as in the modeled PDF with a shift from 220 ppbv to 290 ppbv and a very low probability of MLS measurements observing low volume mixing ratios below 150 ppbv. Future studies should include the vertical correction of the MLS climatologies by the satellite retrieval as well as tuning of the resolution parameterization of the discrete vertical levels of the model to see to what extent the differences can be reduced.

Chapter 5

Representation of Antarctic Polar Vortex

In the following chapter (5) the representation of the southern hemisphere polar vortex in the ICON/MESSy-CLaMS model is described. The transport processes of a long-lived chemical species across the sub-polar transport barrier are directly linked to the strength of the horizontal gradient of that chemical species (*Shepherd*, 2007; *Jin et al.*, 2009; *Hegglin et al.*, 2010). The horizontal gradient of nitrous oxide in a monthly zonal mean are calculated for MLS climatologies and ICON/MESSy-CLaMS model results. In addition, the horizontal gradient of nitrous oxide is calculated on a daily basis, in order to overcome the smoothing of a climatology which affects the strength of the horizontal gradient. The method is described in section (5.2) and enables a time evolution analysis.

5.1 Horizontal Gradient

The zonal mean climatologies obtained in chapter (3) are used to calculate horizontal gradient in latitudinal direction in a monthly climatological analysis on one specific isentropic level. The strength of the gradient of nitrous oxide for climatological mean September is shown in Figure (5.1) for MLS climatologies as well as ICON/MESSy-CLaMS on the isentropic level of 450 K - 550 K in color code in units of ppbv per kilometer. The gradient is obtained by the differences in the volume mixing ratio on the regular longitude latitude grid on grid points

subsequent to each other and division to the latitudinal distance.

As a measure of the transport barrier at the edge of the Antarctic vortex, the horizontal gradient of nitrous oxide for September, October and November at 450 K (≈ 15 km, top), 500 K (≈ 18 km, middle), and 550 K (≈ 20 km, bottom) are shown in Figures (5.1 - 5.3); both for MLS climatologies as well as for the results of the simulation with ICON/MESSy-CLaMS. A higher value in the horizontal gradient of N_2O corresponds to a increased transport barrier or more strength in the transport barrier. Clearly, nitrous oxide mixing ratios for both, measurements and simulation show a pronounced transport barrier visible as a strong enhancement of the N_2O gradient at the edge of the polar vortex.

In general, the transport barrier simulated in ICON/MESSy-CLaMS increases in strength moving upwards in the stratosphere for September, October and November. The horizontal gradient in September and October are approximately unchanged on the respective isentropic level, whereas a weakening of the transport barrier is simulated in November. In the observations of MLS climatologies, the horizontal gradient is increasing from September to October and weakening from October to November at the isentropic levels of 500 K and 550 K. At the isentropic level of 450 K the transport barrier is unchanged in the month of October and November. In contrast to the simulation, the MLS climatologies observe an increased barrier with lower potential temperature surfaces. The MLS climatologies observe an increased barrier at the isentropic level of 450 K compared to a weaker transport barrier at the higher isentropic levels of 500 K and 550 K.

On all isentropic levels in the lower stratosphere (450 K, 500 K, and 550 K) the simulation shows a more narrow edge of the vortex (covering a smaller latitude range) than the observations. Further, in the simulation, the transport barrier is located more equatorward, (i.e. the vortex is larger than observed). The observed transport barrier is also more variable than the simulated one, especially at the isentropic level of 450 K. The strength in the transport barrier between the observation and the simulation are in good agreement with some exceptions. At the isentropic level of 450 K a stronger horizontal gradient is observed in the MLS climatologies, independent of the month considered. The transport barrier in October at 500 K is underestimated in the simulation.

The maximum values of the gradient, consistent along all meridional directions, are in the order of 0.05 - 0.07 ppbv/km in the simulation. There are exceptions of even higher maximum values up to 0.1 ppbv/km, e.g.: 90°W - 30°E in September 550 K and 30°W - 90°E in October 550 K. The values of the horizontal gradient are consistent with the values found in previous studies of zonal monthly mean distribution of nitrous oxide. Maximum values in a simulations of Lagrangian transport driven by ECHAM atmospheric circulation are 0.06 ppbv/km in September at 450 K (*Hoppe et al.*, 2014) as well as maximum values of 0.05 ppbv/km in July between approximately 490 K and 650 K conducted in a CTM simulation driven by a GCM with ECMWF Reanalysis nudging (*Miyazaki and Toshiki*, 2008).

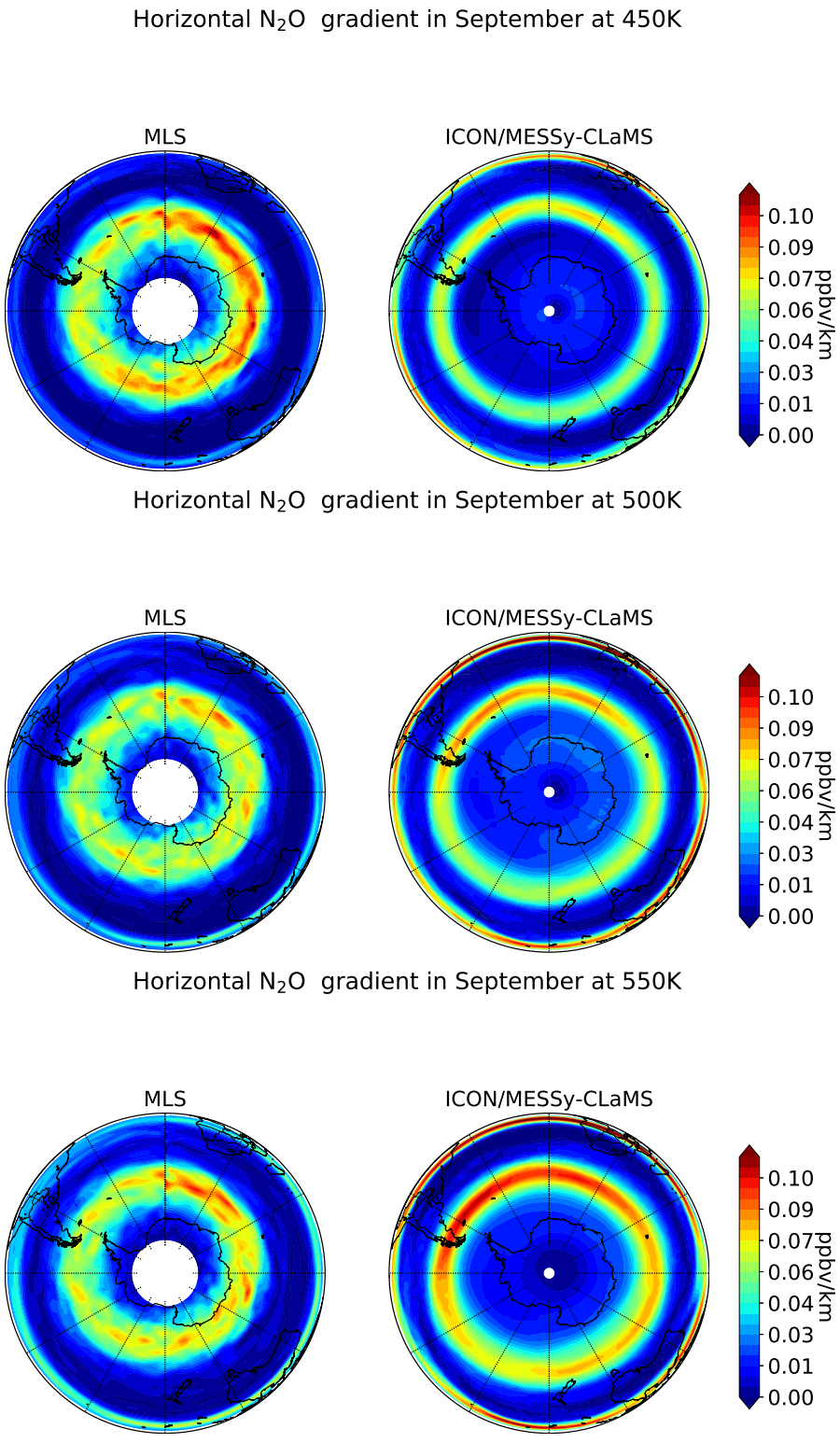

Figure 5.1: Horizontal N_2O gradient in the southern hemisphere in September at 450 - 550 K potential temperature. Gradient calculated from monthly mean 2005-2017 MLS climatologies (left panel) and monthly mean of ten year simulations in MESSy/ICON-CLaMS (right panel)

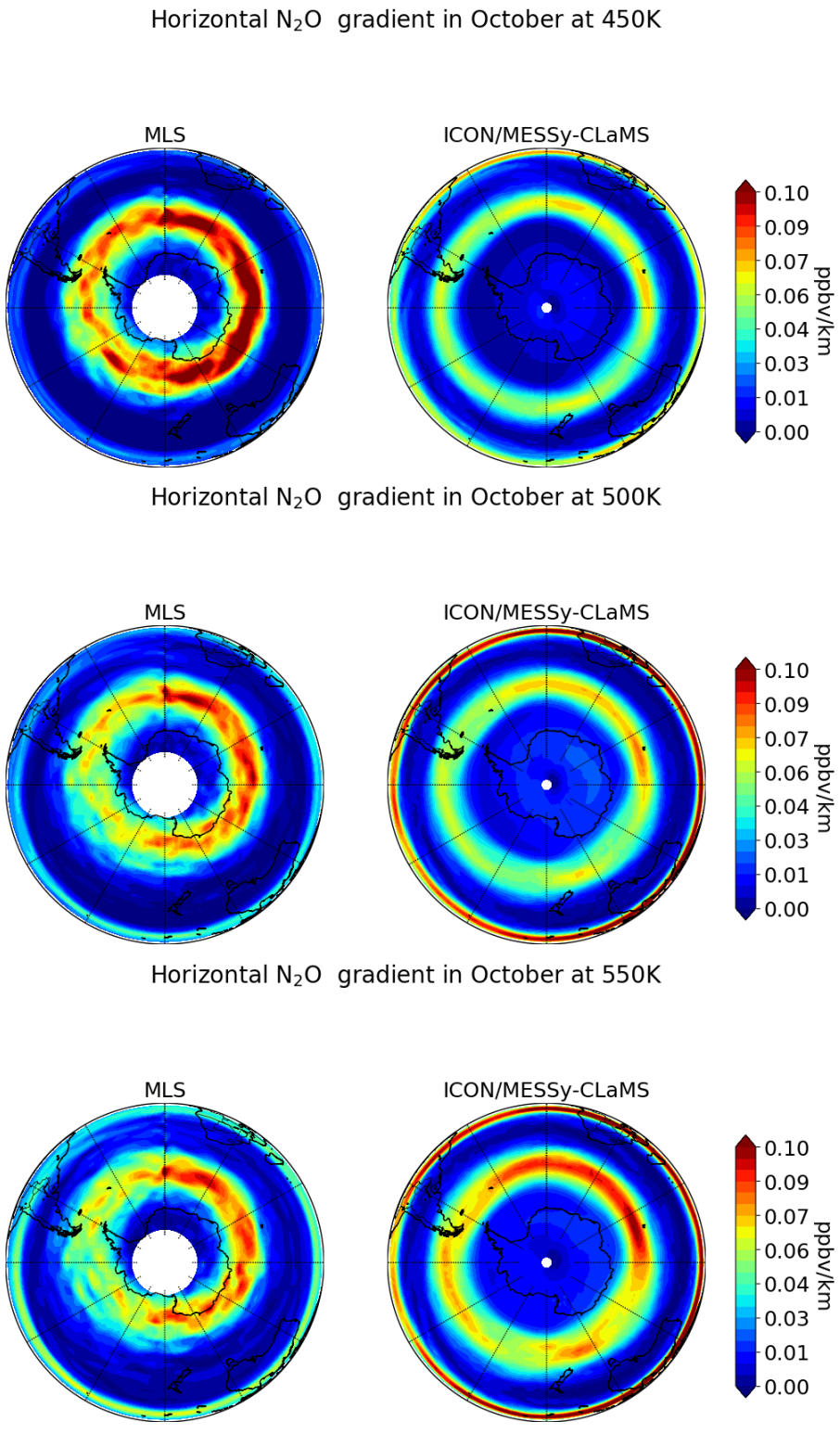

Figure 5.2: Horizontal N_2O gradient in the southern hemisphere in October at 450 - 550 K potential temperature. Gradient calculated from monthly mean 2005-2017 MLS climatologies (left panel) and monthly mean of ten year simulation in MESSy/ICON-CLaMS (right panel)

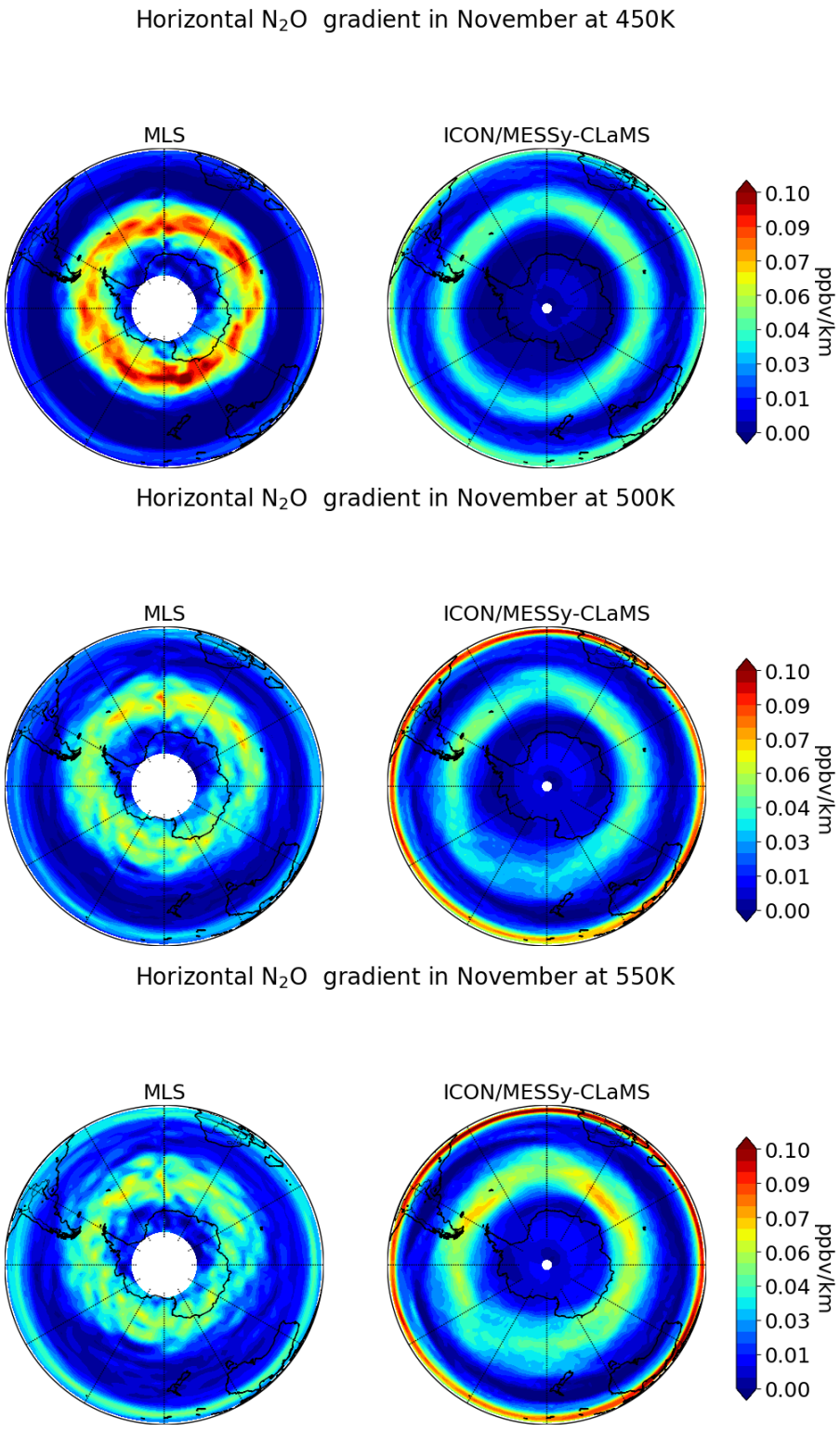

Figure 5.3: Horizontal N_2O gradient in the southern hemisphere in November at 450 - 550 K potential temperature. Gradient calculated from monthly mean 2005-2017 MLS climatologies (left panel) and monthly mean of ten year simulation in MESSy/ICON-CLaMS (right panel)

5.2 Maximum Horizontal Gradient of Nitrous Oxide

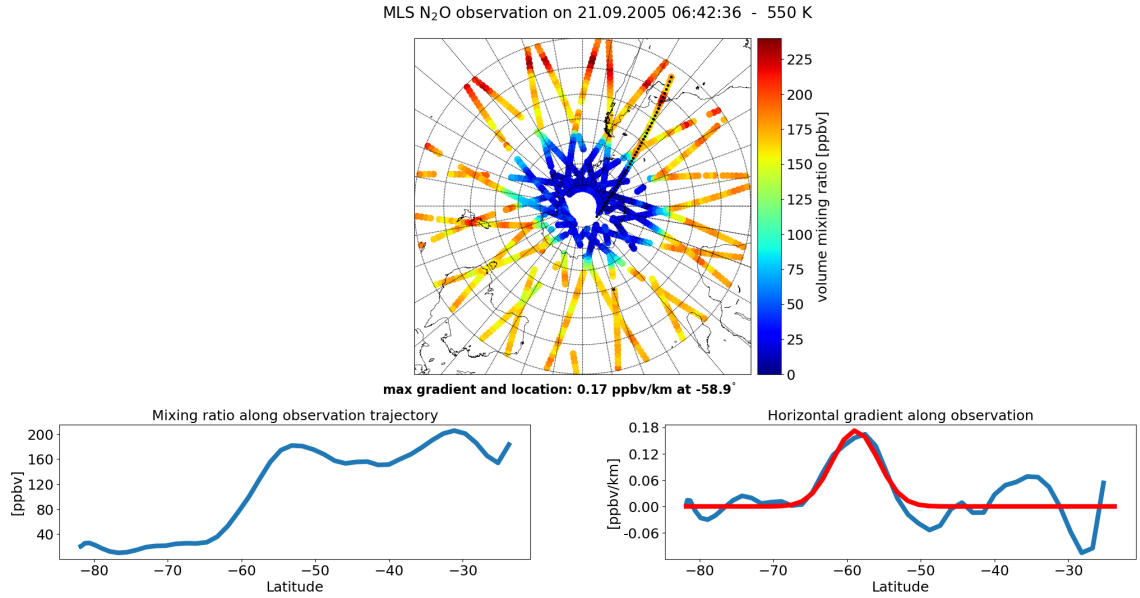

Figure 5.4: MLS observations of N_2O in the southern polar region. The satellite orbit and the corresponding observational locations are accumulated for 24 hours. In the Figure the day 21.09.2022 is shown as an example. Along one orbit trajectory the volume mixing ratio of N_2O (bottom left panel) and the latitudinal gradient (bottom right panel) is shown. The analyzed orbit is marked with black dots in the top panel.

The measured distribution of N_2O by MLS across the polar vortex region is analyzed to estimate the maximum gradient of N_2O at the vortex edge. Slices along the observation flight paths of the satellite show the measurements of MLS N_2O mixing ratio. The Antarctic polar region is transected 15 times a day. As an example the accumulated observations on 21.09.2005 are shown in the top panel of Figure (5.4) for the 550 K isentropic level. The N_2O volume mixing ratio is depicted in the colorcode. The volume mixing ratio along the observation orbit is plotted versus latitude in the bottom left panel. The single flight path under consideration is highlighted with black dots in the top panel. Furthermore the gradient along the latitude direction is calculated. Within the range of 70°S to 40°S the gradient is fitted to a Gaussian profile (see Figure 5.4 bottom left panel). Whenever the position of the maximum gradient is outside the interval 70°S to 40°S, the profile was considered invalid. Furthermore any observational path is considered invalid, where two consecutive measurement points are missing. This analysis allows a value to be determined for the maximal horizontal gradient

regardless of a smoothed zonal mean distribution.

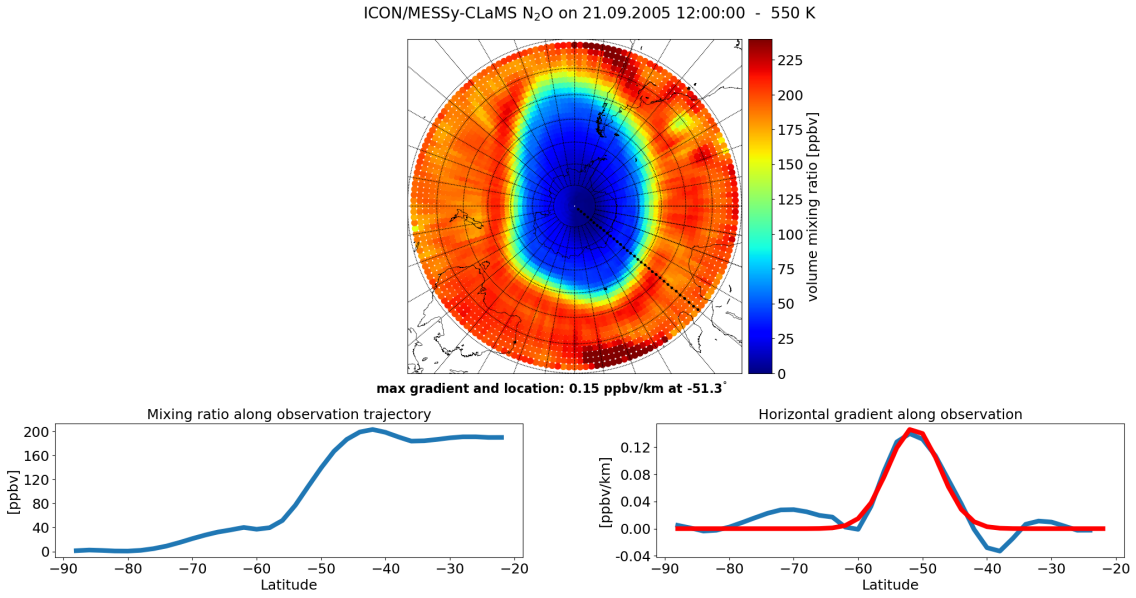

Figure 5.5: ICON/MESSy-CLaMS modeled N_2O volume mixing ratio is shown in the southern polar region (top panel). The satellite orbit and the corresponding observational locations are accumulated for 24 hours. In the Figure the day 21.09.2022 is shown as an example. Along one orbit trajectory the volume mixing ratio of N_2O (bottom left panel) and the latitudinal gradient (bottom right panel) is shown. The analyzed orbit is marked with black dots in the top panel.

The resulting fitting parameter for the strength of the maximum gradient (cf. Gaussian multiplier) are accumulated for all valid transections within a period of three days. For this accumulated list of valid parameters the arithmetic mean value is calculated to specify the maximum horizontal gradient of nitrous oxide. The average values are calculated for the vertical extent of 450 K to 700 K and from the beginning of May to the end of January of the year 2005 within a period of three days. The maximum strength of N_2O gradient is shown in colorcode on the left panel in Figure (5.6) in the next section (5.3).

The modeled points of ICON/MESSy-CLaMS nitrous oxide provide an equivalent analysis. The mixing ratio is assessed along the meridional direction. The meridional profiles are evaluated every ten degrees of longitude. The top panel of Figure (5.5) displays the distribution of nitrous oxide mixing ratio given at one particular timestep. The bottom panels show the mixing ratio along the explicit meridian and the gradient as for Figure (5.4) described

above. The maximum strength of N_2O gradient is shown in colorcode on the right panel in Figure (5.6)

5.3 Time Evolution of Maximum Horizontal Gradient

According to the analysis described in the previous section (5.2), the values for the maximum horizontal gradients of the southern hemispheric polar region are accumulated for three days and a three day average is calculated after accumulation. This can be done for a certain time period and on several isentropic surfaces. The statistical analysis of the maximum horizontal gradient between the time period May to January on the isentropic surfaces from 450 K to 700 K (≈ 15-26 km) are shown in right panels of Figures (5.6 - 5.12) for seven different simulation years (Simulation year 1 - Simulation year 7) of ICON/MESSy-CLaMS. In the left panels the maximum horizontal gradient in the MLS observations from May 2005 to January 2006 are shown, repeatedly. For different years of MLS observations see the next section (5.4).

The overall strength of the transport barrier (in volume mixing ratio per km) is similar for the simulation and the observation, however the simulated transport barrier looses its strength below about 550 K (≈ 20 km) while the observations show that the transport barrier extends down to 450 K (≈ 15 km). The observed transport barrier gains in strength starting in August (at the top potential temperature levels); it rapidly looses strength at 700 K (≈ 26 km) in late November, while at 450 K (≈ 15 km) there remains a transport barrier until early January (Figures 5.6 - 5.12; left panels). In contrast, the ICON/MESSy-CLaMS simulation indicates the existence of a transport barrier until too late in the season (above about 550 K, ≈ 20 km). There is some variability in the individual years of the time slice run (right panels). Those variability arise in quantitative values in mixing ratio per kilometer rather then qualitative features. The Simulation years 6 and 7 are weaker in maximum horizontal gradient than the Simulation years 1-5. The maximum gradient in Simulation year 2 is

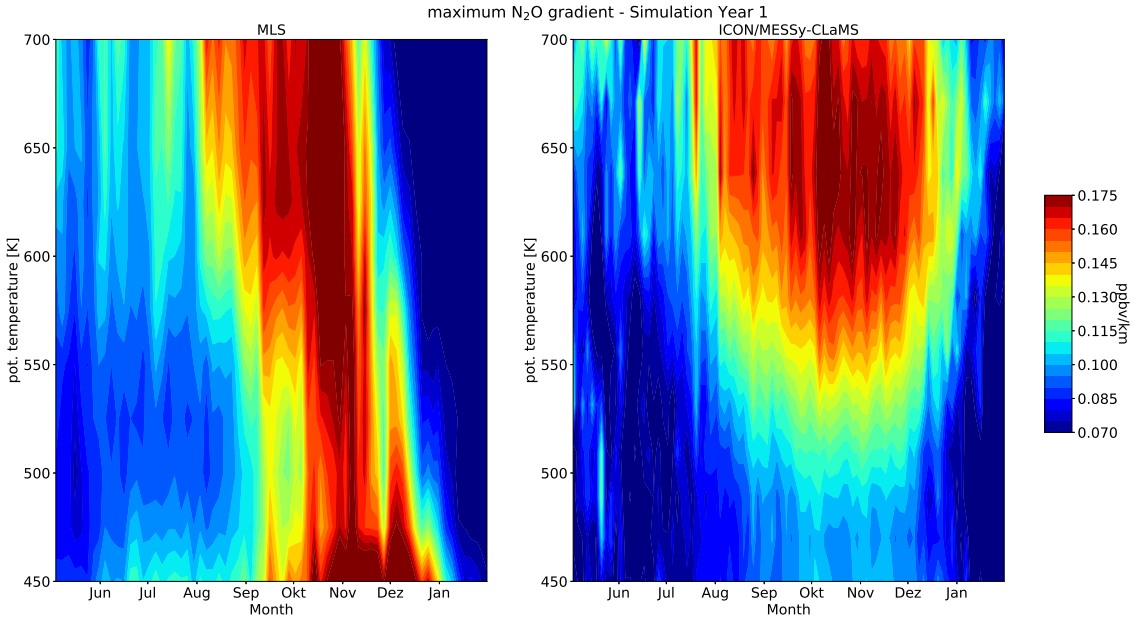

Figure 5.6: Time series of maximum gradient of nitrous oxide in latitudinal direction in vertical range from 450 K potential temperature up to 700 K. MLS 2005 observations (left panel). ICON/MESSy-CLaMS Simulation Year 1 (right panel)

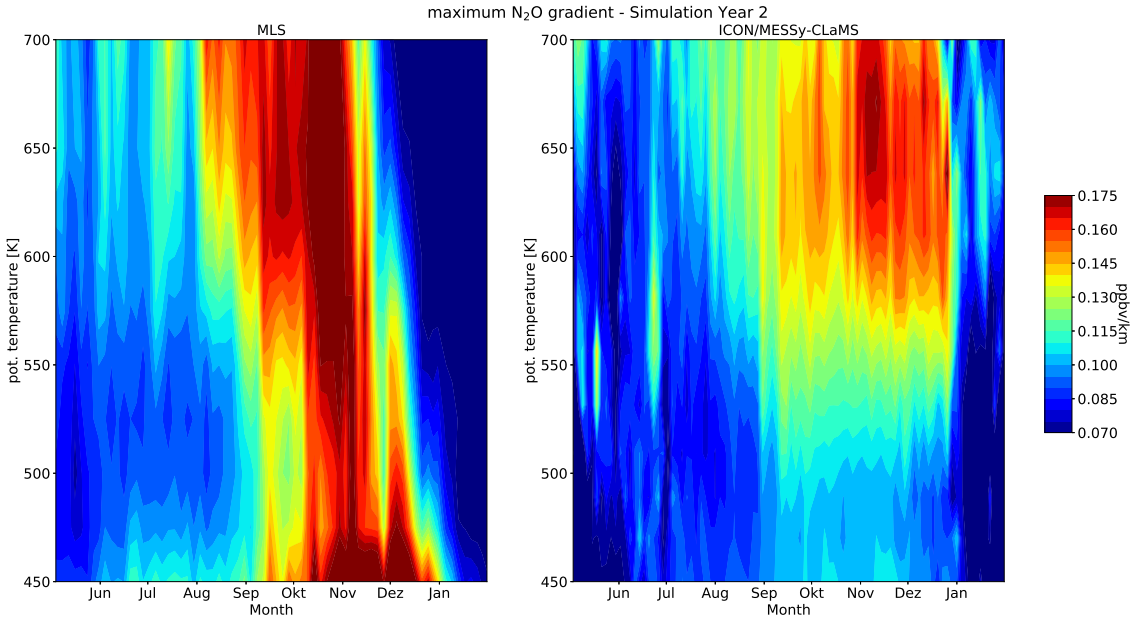

Figure 5.7: Same as Figure 5.6 except for ICON/MESSy-CLaMS Simulation Year 2 (right panel)

weaker below 600 K and before November, than the other simulation years. In a study by *Seo and Choi* (2022) determining the vortex breakup date in the stratosphere from 430 K up

to 1260 K, the mean break up date is terminated at the beginning of December for 600 K and at the end of December for 430 K.

The results shown in this section focus on three day average of the maximum horizontal gradient, instead of horizontal gradient of the monthly mean distribution. The time average in section (5.1) is calculated on a coarser temporal resolution. There is no discrepancy between the results shown in section (5.1) and section (5.2).
On the other hand there are differences in the maximum horizontal gradient in the lower isentropic level of 450 K and to some extent 500 K. In the previous chapters, the distribution of volume mixing in the lower level showed differences in MLS climatologies and the simulation results at this particular level. The present study provides a good overview of the representation of the transport barrier in the Antarctic polar vortex region. In future studies an additional comparison of the chemical distribution of nitrous oxide and the corresponding horizontal gradient with other satellite or in-situ measurements in the lower stratosphere can contribute to a better quantification of the transport barrier.

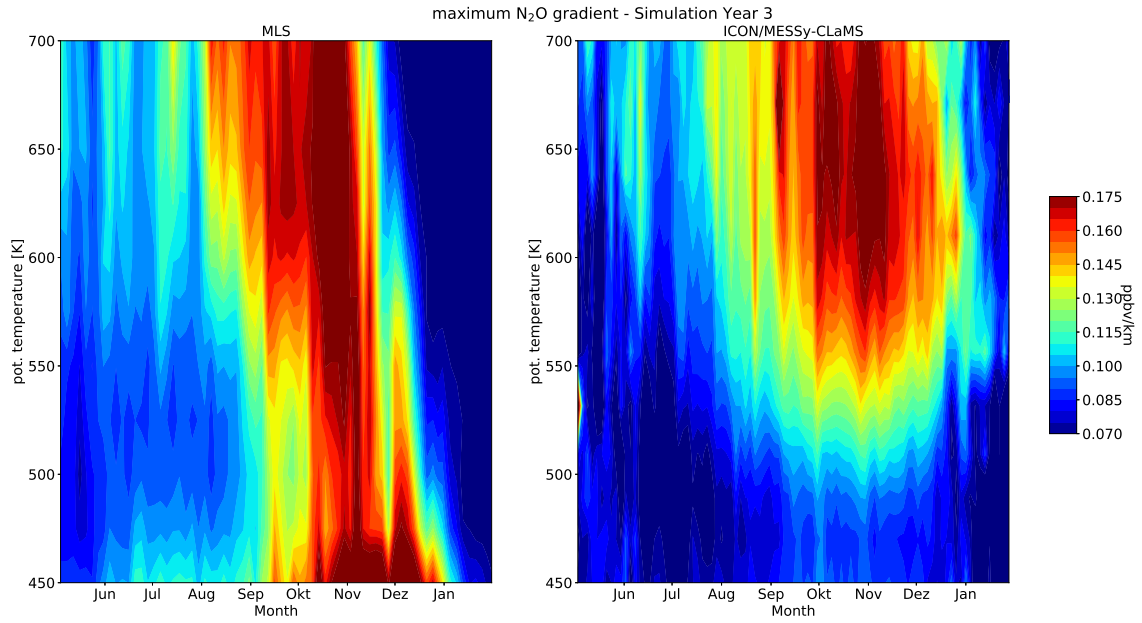

Figure 5.8: Same as Figure 5.6 except for ICON/MESSy-CLaMS Simulation Year 3 (right panel)

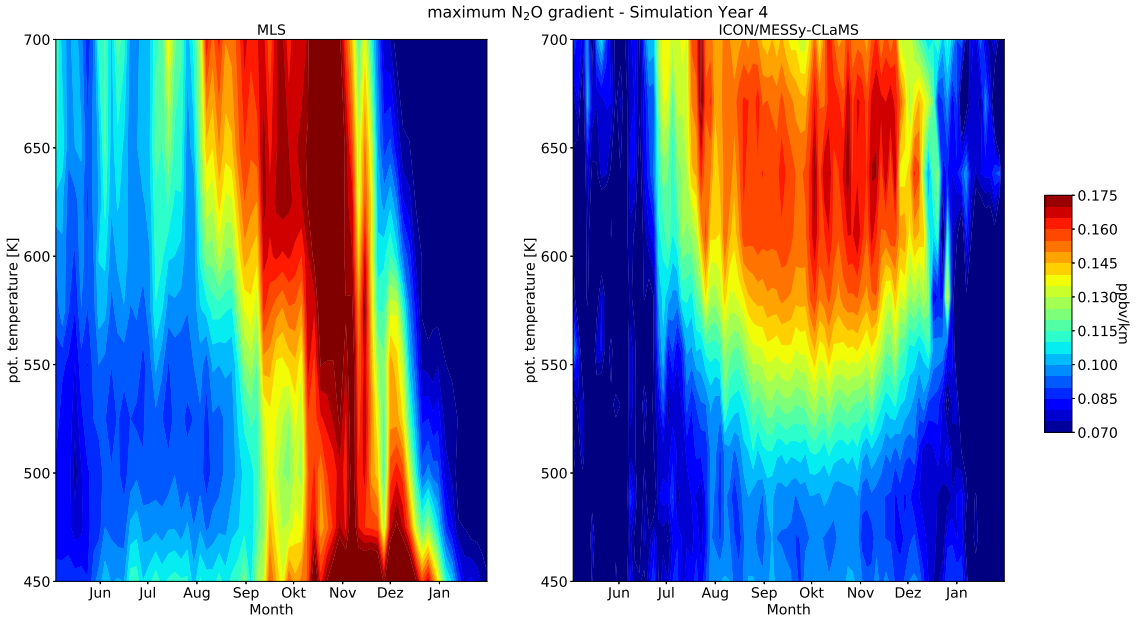

Figure 5.9: Same as Figure 5.6 except for ICON/MESSy-CLaMS Simulation Year 4 (right panel)

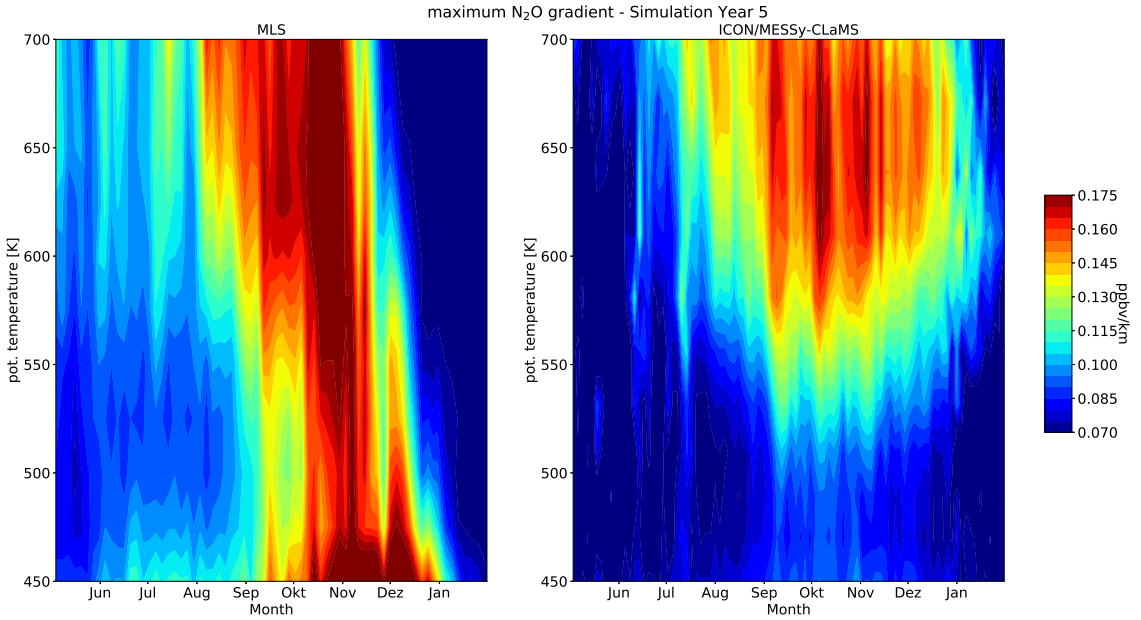

Figure 5.10: Same as Figure 5.6 except for ICON/MESSy-CLaMS Simulation Year 5 (right panel)

5.4 Maximum Horizontal Gradient in MLS 2005 - 2010

Similar analyses were conducted for the results of different observation years with MLS. The results for the years 2005 - 2010 are shown in Figures (5.13 - 5.15) There is also a certain year-

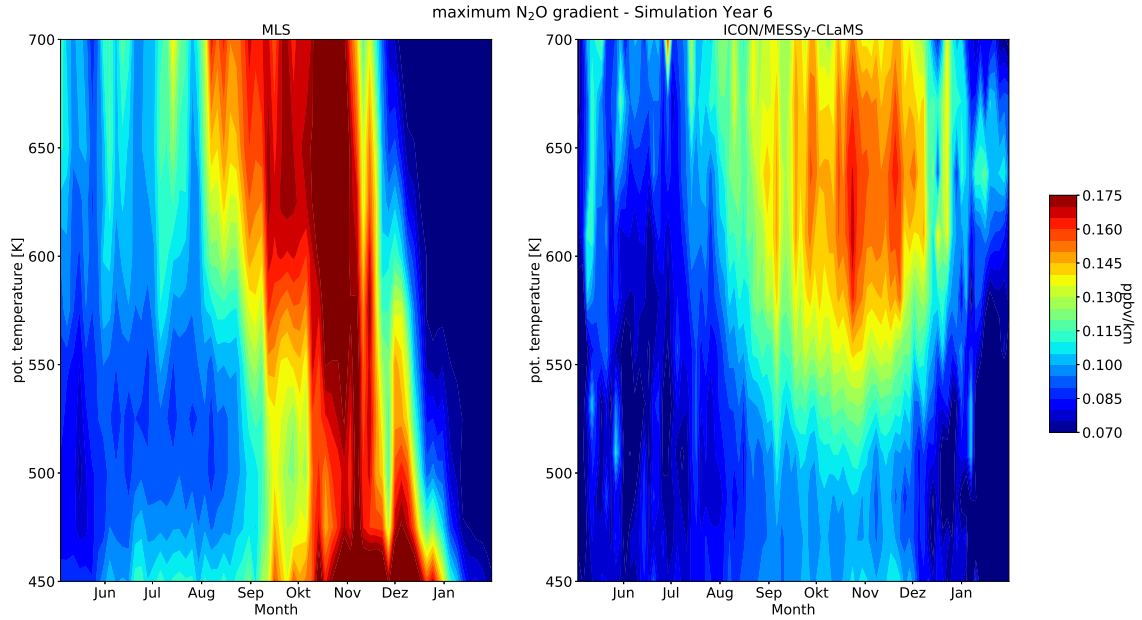

Figure 5.11: Same as Figure 5.6 except for ICON/MESSy-CLaMS Simulation Year 6 (right panel)

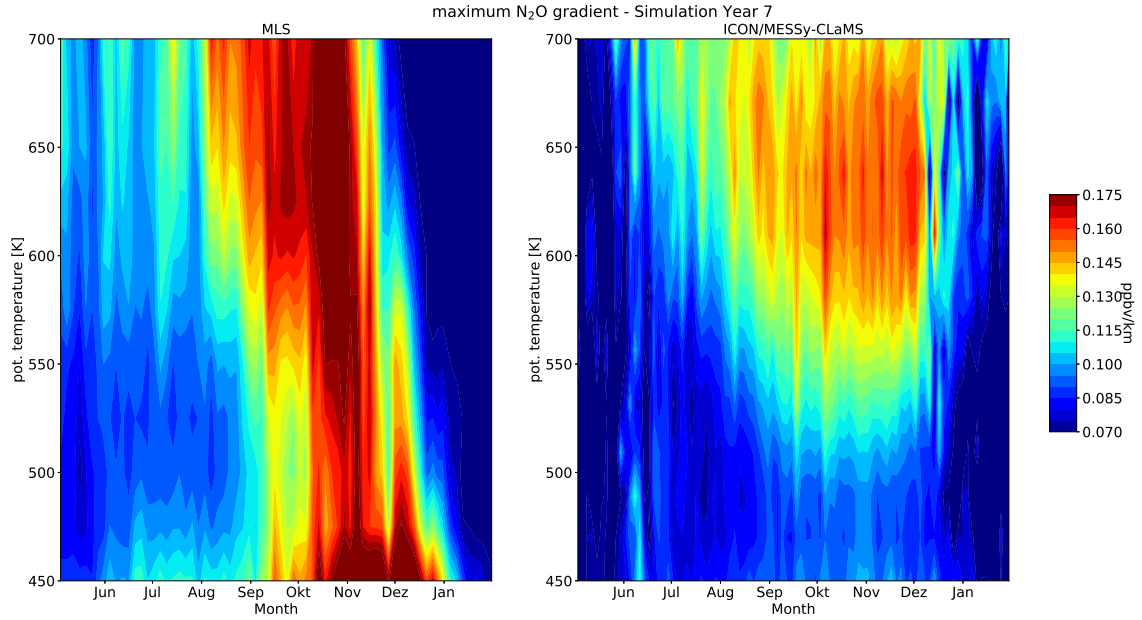

Figure 5.12: Same as Figure 5.6 except for ICON/MESSy-CLaMS Simulation Year 7 (right panel)

to-year variability in the observations, but the overall feature discussed in the previous section for the year 2005 is robust. The strength of the transport barrier is consistent throughout the isentropic levels in November. An earlier vortex breakup is observed in higher isentropic levels until the vortex break up reaches isentropic levels of 450 K in January.

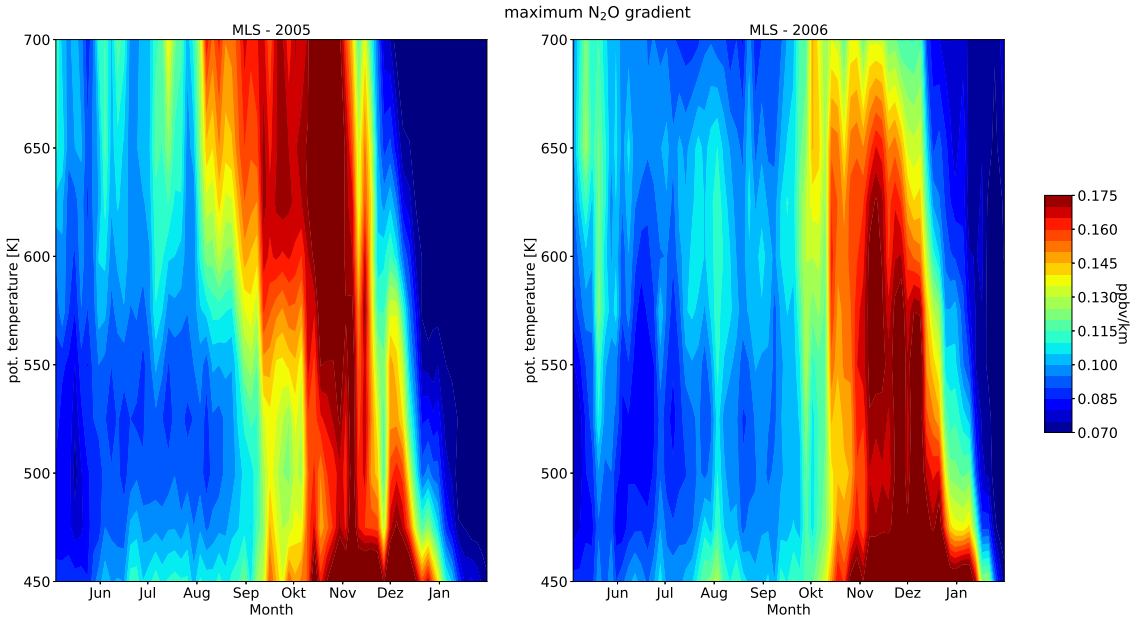

Figure 5.13: Time series of maximum gradient of nitrous oxide in latitudinal direction in vertical range from 450 K potential temperature up to 700 K. MLS 2005 observations (left panel). MLS 2006 observations (right panel)

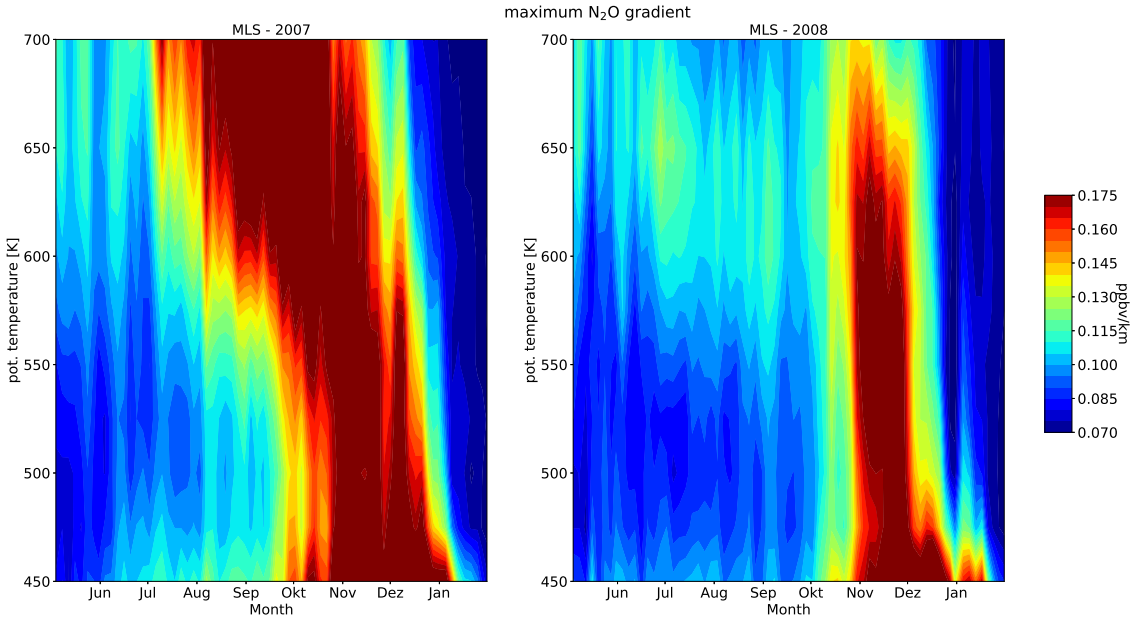

Figure 5.14: Same as Figure 5.13 except for 2007 (left panel) and 2008 (right panel)

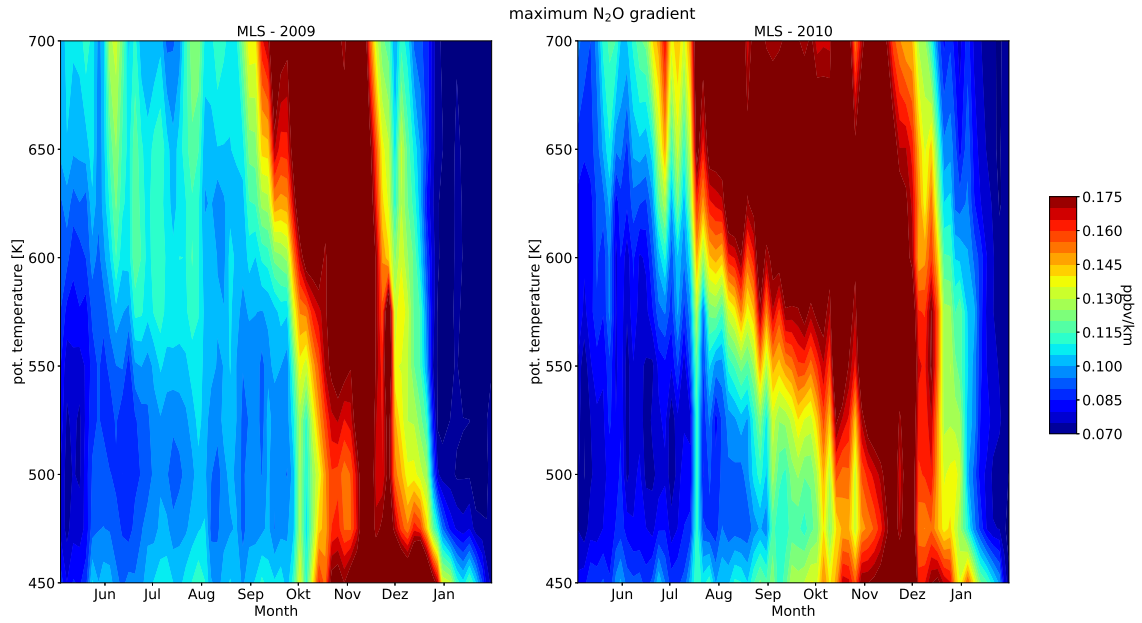

Figure 5.15: Same as Figure 5.13 except for 2009 (left panel) and 2010 (right panel)

Chapter 6

Discussion

The transport of atmospheric constituents and the representation of atmospheric transport barriers in a newly developed chemistry transport model, ICON/MESSY-CLaMS, are described and analyzed in the present study. Horizontal winds and vertical velocities on the ICON grid (where vertical velocities are deduced from diabatic terms calculated in the ICON model) were integrated into a Lagrangian transport simulation based on the CLaMS model. Simulating transport using Lagrangian methods can reduce problems caused by numerical diffusion in Eulerian schemes (e.g., *McKenna et al.* (2002b); *Charlesworth et al.* (2023)). However, there are limitations. In this study, horizontal winds on the ICON grid were interpolated onto a regular latitude-longitude grid with a horizontal resolution of 2°x 2°to drive the CLaMS transport. This horizontal resolution may not be be sufficient to accurately resolve small-scale features like sharp boundaries of transport barriers like the antarctic polar vortex.

The zonal mean diabatic heating rates, which determine the vertical transport, derived from ICON temperature tendencies, are in reasonable agreement with ERA-Interim and ERA-5 heating rates. It is important to note that the ICON heating rates are derived from a free running simulation that is not nudged to observed conditions, so a close correspondence is not expected. Possible discrepancies between the observations and Lagrangian simulations may be due to the ICON winds, which include diffusion related to the ICON dynamical core, which is not Lagrangian. The same applies to ERA5, where the underlying model (e.g., section 2.7) is also diffusive to some extent. Ideally, a dynamical core employing Lagrangian

techniques would be used to better control the numerical diffusion of the dynamical core; here progress is difficult as such models are currently not under development.

The quality of the transport in the ICON/MESSy-CLaMS model is tested in this study through comparison with N_2O measurements by the MLS instrument. The model simulation, consistently with MLS observations, shows a decline of N_2O with altitude, which is caused by chemical loss of N_2O at greater heights in the stratosphere (above about 500 K). Further, upward transport of N_2O in the tropical pipe and diabatic descent over the winter poles is represented in the model simulation. Further, comparisons of the results of simulations with the ICON/MESSy-CLaMS model with MLS-N_2O observations (see section 3.2.1) suffer from the uncertainty of MLS measurements, especially at lower altitudes; the MLS uncertainty at $\approx$ 400 K is 44% and at $\approx$ 460 K is 22%. And the results of the perpetual model simulations for N_2O for 2005 can only be expected to be comparable to, but not very close to an observed MLS N_2O climatology for 2005-2017.

In future studies further issues should be explored. First, tests of the transport (e.g., N_2O) in the default Eulerian transport scheme of ICON (*Reinert*, 2020; *Reinert and Zängl*, 2021) and comparison with the Lagrangian techniques described here should be performed. Also conducting ensemble simulations would a way to better characterize the inherent uncertainties of model simulations. Further tests with an increased horizontal resolution and tests of the sensitivity of the results on the chosen resolution would be helpful. Finally, results may be improved by employing Lagrangian methods, which work directly on ICON native triangular grid. Implementing such Lagrangian methods into the dynamical core or the transport scheme has the potential to reduce numerical diffusion in global models.

A focus of the comparisons presented here is on the Antarctic vortex. Clearly both, the observations and the simulation for the Antarctic show the transport barrier at the edge of the vortex (horizontal maps of N_2O mixing ratios). The transport barrier is manifested as a strong enhancement of the latitudinal N_2O gradient. The simulation shows a larger than observed vortex and the transport barrier is less variable in the simulation than in the observations. Both, the simulation and the observations show low N_2O mixing ratios in the Antarctic vortex, which are caused by diabatic descent. The strength of the transport barrier in October and

November in the MLS observations extends down to 450 K (≈ 15 km), while the simulation indicates a substantial reduction of the strength of the transport barrier below about 550 K (≈ 20 km).

The transport barrier at the edge of the polar vortex was analysed with the help of PDFs of N_2O mixing ratios with respect to latitude. These PDFs allow polar and mid-latitude airmasses to be clearly distinguished in the simulations as a double peak structure for the period when the polar vortex is present (August - November). The double peak structure is similarly seen in the observations albeit the observed peak in the N_2O PDF is generally higher and shifted somewhat towards higher N_2O mixing ratios than simulated. Overall there is an agreement between the simulations and the observations. Some differences between the observations and the Lagrangian simulations are caused by the underlying ICON winds.

The polar vortex (and the associated transport barrier at its edge) is well represented in the simulations, although the simulated polar vortex is larger than observed. By the use of the Lagrangian transport calculations, in general, a good representation of atmospheric transport barriers is possible. The coupled ICON/MESSy-CLaMS transport scheme allows tracer distributions in the free troposphere and in the stratosphere to be better simulated than by classical Eulerian schemes. In future work, the impact of the spatial resolution in ICON and CLaMS on the results of the simulation will be investigated. Further, a more direct coupling of ICON winds with Lagrangian transport is envisaged.

Bibliography

Alexander, L., Global observed long-term changes in temperature and precipitation extremes: A review of progress and limitations in IPCC assessments and beyond, *Wea. and Clim. Extr.*, *11*, 4–16, doi:10.1016/j.wace.2015.10.007, 2016.

Arias, P., et al., Technical Summary, in *Climate Change 2021: The Physical Science Basis. Contribution of Working Group I to the Fourth Assessment Report of the Intergovernmental Panel on Climate Change*, pp. 33–144, Masson-Delmotte, V. and P. Zhai and A. Pirani and S.L. Connors and C. Péan and S. Berger and N. Caud and Y. Chen and L. Goldfarb and M.I. Gomis and M. Huang and K. Leitzell and E. Lonnoy and J.B.R. Matthews and T.K. Maycock and T. Waterfield and O. Yelekçi and R. Yu and and B. Zhou (eds.), Cambridge University Press, Cambridge, United Kingdom and New York, NY, USA., doi:10.1017/9781009157896.002, 2021.

Baldwin, M. P., et al., 100 years of progress in understanding the stratosphere and mesosphere, *Meteorol. Monographs*, *59*, 27.1–27.29, doi:10.1175/AMSMONOGRAPHS-D-19-0003.1, 2019.

Bechtold, P., M. Köhler, T. Jung, F. Doblas-Reyes, M. Leutbecher, M. J. Rodwell, F. Vitart, and G. Balsamo, Advances in simulating atmospheric variability with the ECMWF model: From synoptic to decadal time-scales, *Q. J. R. Meteorol. Soc.*, *134*(634), 1337–1351, doi:10.1002/qj.289, 2008.

Becker, G., J.-U. Grooß, D. S. McKenna, and R. Müller, Stratospheric photolysis frequencies: Impact of an improved numerical solution of the radiative transfer equation, *J. Atmos. Chem.*, *37*, 217–229, doi:10.1023/A:1006468926530, 2000.

Birner, T., and H. Bönisch, Residual circulation trajectories and transit times into the extratropical lowermost stratosphere, *Atmos. Chem. Phys.*, *11*, 817–827, doi:10.5194/acp-11-817-2011, 2011.

Bodeker, G., et al., Reference upper-air observations for climate: From concept to reality, *Bull. Am. Meteorol. Soc.*, *97*(1), 123–135, 2016.

Bonaventura, L., and T. Ringler, Analysis of discrete shallow-water models on geodesic delaunay grids with c-type staggering, *Mon. Wea. Rev.*, *133*(8), 2351–2373, 2005.

Bönisch, H., A. Engel, T. Birner, P. Hoor, D. W. Tarasick, and E. A. Ray, On the structural changes in the Brewer-Dobson circulation after 2000, *Atmos. Chem. Phys.*, *11*, 3937–3948, doi:10.5194/acp-11-3937-2011, 2011.

Brewer, A. W., Evidence for a world circulation provided by the measurements of helium and water vapour distribution in the stratosphere, *Q. J. R. Meteorol. Soc.*, *75*(326), 351–363, doi:10.1002/qj.49707532603, 1949.

Brinkop, S., and P. Jöckel, Attila 4.0: Lagrangian advective and convective transport of passive tracers within the echam5/messy (2.53.0) chemistry–climate model, *Geosci. Model Dev.*, *12*(5), 1991–2008, doi:10.5194/gmd-12-1991-2019, 2019.

Butchart, N., The Brewer-Dobson circulation, *Rev. Geophys.*, *52*, 157–184, doi:10.1002/2013RG000448, 2014.

Charlesworth, E., et al., Stratospheric water vapor affecting atmospheric circulation, *Nature Comm.*, *14*(1), 3925, doi:https://doi.org/10.1038/s41467-023-39559-2, 2023.

Charlesworth, E. J., A.-K. Dugstad, F. Fritsch, P. Jöckel, and F. Plöger, Impact of Lagrangian transport on lower-stratospheric transport time scales in a climate model, *Atmos. Chem. Phys.*, *20*, 15,227–15,245, doi:10.5194/acp-20-15227-2020, 2020.

Chen, D., et al., Framing,context,and methods, in *Climate Change 2021: The Physical Science Basis. Contribution of Working Group I to the Sixth Assessment Report of the Intergovernmental Panel on Climate Change*, pp. 147–286, Masson-Delmotte, V. and P. Zhai and A. Pirani

and S.L. Connors and C. Pean and S. Berger and N. Caud and Y. Chen and L. Goldfarb and M.I. Gomis and M. Huang and K. Leitzell and E. Lonnoy and J.B.R. Matthews and T.K. Maycock and T. Waterfield and O. Yelekci and R. Yu and B. Zhou (eds.), Cambridge University Press, Cambridge, United Kingdom and New York, NY, USA., doi: 10.1017/9781009157896.003, 2021.

Chipperfield, M. P., New version of the TOMCAT/SLIMCAT off-line chemical transport model: Intercomparison of stratospheric tracer experiments, *Q. J. R. Meteorol. Soc.*, *132*(617, B), doi:10.1256/qj.05.51, 2006.

Crueger, T., et al., ICON-A, The Atmosphere Component of the ICON Earth System Model: II. Model Evaluation, *J. Adv. Mod. Earth Sys.*, *10*, 1638–1662, doi:10.1029/2017MS001233, 2018.

Crutzen, P. J., The influence of nitrogen oxides on the atmospheric ozone content, *Q. J. R. Meteorol. Soc.*, *96*, 320–325, 1970.

Dee, D. P., et al., The ERA-Interim reanalysis: configuration and performance of the data assimilation system, *Q. J. R. Meteorol. Soc.*, *137*, 553–597, doi:10.1002/qj.828, 2011.

Di Luca, A., R. de Elía, M. Bador, and D. Argüeso, Contribution of mean climate to hot temperature extremes for present and future climates, *Wea. and Clim. Extr.*, *28*, 100,255, doi:10.1016/j.wace.2020.100255, 2020.

Dobson, G. M. B., Origin and distribution of polyatomic molecules in the atmosphere, *Proc. R. Soc. London A.*, *236*, 187–193, 1956.

Doms, G., et al., A description of the nonhydrostatic regional cosmo model part ii : Physical parameterization, *Tech. Rep. LM F90 4.20*, DWD: Offenbach, Germany, last access: 18 September 2023, 2011.

Dubal, M., N. Wood, and A. Staniforth, Analysis of parallel versus sequential splittings for time-stepping physical parameterizations, *Mon. Wea. Rev.*, *132*(1), 121–132, doi: https://doi.org/10.1175/1520-0493(2004)131<0121:AOPVSS>2.0.CO;2, 2004.

Dubal, M., N. Wood, and A. Staniforth, Mixed parallel–sequential-split schemes for time-stepping multiple physical parameterizations, *Mon. Wea. Rev.*, *133*(4), 989–1002, doi: https://doi.org/10.1175/MWR2893.1, 2005.

Dunn, R., et al., Development of an updated global land in situ-based data set of temperature and precipitation extremes: Hadex3, *J. Geophys. Res.*, *16*(125), doi:10.1029/2019jd032263, 2020.

ECMWF, *IFS Documentation Cy33r1*, European Centre for Medium-Range Weather Forecasts ECMWF, www.ecmwf.int/research/ifsdocs/CY33r1/DYNAMICS/, 2009.

Eyring, V., T. G. Sheperd, and D. W. W. (eds.) (Eds.), *SPARC report on the evaluation of chemistry-climate models*, SPARC Rep. No. 5, WRCP-132, WMO-TD No. 1526, 434 pp., World Meteorol. Organ., Geneva, 2010.

Fischer, E. M., and R. Knutti, Observed heavy precipitation increase confirms theory and early models, *Nature Clim. Cha.*, *6*(11), 986–991, doi:10.1038/NCLIMATE3110, 2016.

Froidevaux, L., D. E. Kinnison, R. Wang, J. Anderson, and R. A. Fuller, Evaluation of cesm1 (waccm) free-running and specified dynamics atmospheric composition simulations using global multispecies satellite data records, *Atmos. Chem. Phys.*, *19*(7), 4783–4821, doi: 10.5194/acp-19-4783-2019, 2019.

Fueglistaler, S., B. Legras, A. Beljaars, J.-J. Morcrette, A. Simmons, A. M. Tompkins, and S. Uppapla, The diabatic heat budget of the upper troposphere and lower/mid stratosphere in ECMWF reanalyses, *Q. J. R. Meteorol. Soc.*, *135*, 638, doi:10.1002/qj.361, 2009.

Fujiwara, M., et al., Introduction to the SPARC reanalysis intercomparison project (S-RIP) and overview of the reanalysis systems, *Atmos. Chem. Phys.*, *17*(2), 1417–1452, doi: 10.5194/acp-17-1417-2017, 2017.

Geist, K., U. Parlitz, and W. Lauterborn, Comparison of different methods for computing Lyapunov exponents, *Progr. Theor. Phys.*, *83*, 875–893, 1990.

Giorgetta, M. A., et al., ICON-A, The Atmosphere Component of the ICON Earth System Model: I. Model Description, *J. Adv. Mod. Earth Sys.*, *10*, 1613–1637, doi: 10.1029/2017MS001242, 2018.

Grooß, J.-U., and J. M. Russell, Technical note: A stratospheric climatology for O_3, H_2O, CH_4, NO_x, HCl, and HF derived from HALOE measurements, *Atmos. Chem. Phys.*, *5*, 2797–2807, doi:10.5194/acp-5-2797-2005, 2005.

Grooß, J.-U., G. Günther, R. Müller, P. Konopka, S. Bausch, H. Schlager, C. Voigt, C. M. Volk, and G. C. Toon, Simulation of denitrification and ozone loss for the Arctic winter 2002/2003, *Atmos. Chem. Phys.*, *5*, 1437–1448, 2005.

Grooß, J.-U., et al., Simulation of ozone depletion in spring 2000 with the Chemical Lagrangian Model of the Stratosphere (CLaMS), *J. Geophys. Res.*, *107*, 8295, doi: 10.1029/2001JD000456, 2002.

Gulev, S., et al., Changing state of the climate system, in *Climate Change 2021: The Physical Science Basis. Contribution of Working Group I to the Sixth Assessment Report of the Intergovernmental Panel on Climate Change*, Masson-Delmotte, V. and P. Zhai and A. Pirani and S.L. Connors and C. Pean and S. Berger and N. Caud and Y. Chen and L. Goldfarb and M.I. Gomis and M. Huang and K. Leitzell and E. Lonnoy and J.B.R. Matthews and T.K. Maycock and T. Waterfield and O. Yelekci and R. Yu and B. Zhou, Cambridge University Press, Cambridge, United Kingdom and New York, NY, USA., doi:10.1017/9781009157896.004, 2021.

Harlow, F. H., and J. E. Welch, Numerical calculation of time-dependent viscous incompressible flow of fluid with free surface, *The Phys. of Fluids.*, *8*(12), 2182–2189, 1965.

Hartmann, D., et al., Observations: Atmosphere and Surface., in *Climate Change 2013: The Physical Science Basis. Contribution of Working Group I to the Fifth Assessment Report of the Intergovernmental Panel on Climate Change*, T.F. Stocker, D. Qin, G.-K. Plattner, M. Tignor, S.K. Allen, J. Boschung, A. Nauels, Y. Xia, V. Bex and P.M. Midgley (eds.), Cambridge University Press, Cambridge, United Kingdom and New York, NY, USA., 2013.

Hegglin, M. I., and S. e. Tegtmeier (Eds.), *The SPARC Data Initiative: Assessment of stratospheric trace gas and aerosol climatologies from satellite limb sounders*, doi:10.3929/ethz-a-010863911, 2017.

Hegglin, M. I., et al., Multimodel assessment of the upper troposphere and lower stratosphere: Extratropics, *J. Geophys. Res.*, *115*, D00M09, doi:10.1029/2010JD013884, 2010.

Hersbach, H., et al., The ERA5 global reanalysis, *Q. J. R. Meteorol. Soc.*, *146*(730), 1999–2049, doi:10.1002/qj.3803, 2020.

Hoffmann, L., et al., From ERA-Interim to ERA5: the considerable impact of ECMWF's next-generation reanalysis on Lagrangian transport simulations, *Atmos. Chem. Phys.*, *19*(5), 3097–3124, doi:10.5194/acp-19-3097-2019, 2019.

Hollmann, R., et al., The ESA climate change initiative: Satellite data records for essential climate variables, *Bull. Am. Meteorol. Soc.*, *94*(10), 1541–1552, 2013.

Hoppe, C. M., L. Hoffmann, P. Konopka, J.-U. Grooß, F. Ploeger, G. Günther, P. Jöckel, and R. Müller, The implementation of the CLaMS lagrangian transport core into the chemistry climate model EMAC 2.40.1: application on age of air and transport of long-lived trace species, *Geosci. Model Dev.*, 7(6), 2639–2651, doi:10.5194/gmd-7-2639-2014, 2014.

Hoppe, C. M., F. Ploeger, P. Konopka, and R. Müller, Kinematic and diabatic vertical velocity climatologies from a chemistry climate model, *Atmos. Chem. Phys.*, *16*(10), 6223–6239, doi:10.5194/acp-16-6223-2016, 2016.

Ilyina, T., K. D. Six, J. Segschneider, E. Maier-Reimer, H. Li, and I. Núñez-Riboni, Global ocean biogeochemistry model hamocc: Model architecture and performance as component of the mpi-earth system model in different cmip5 experimental realizations, *J. Adv. Mod. Earth Sys.*, *5*(2), 287–315, doi:doi.org/10.1029/2012ms000178, 2013.

IPCC, Summary for Policymakers, in *Climate Change 2021: The Physical Science Basis. Contribution of Working Group I to the Sixth Assessment Report of the Intergovernmental Panel on Climate Change*, Masson-Delmotte, V. and P. Zhai and A. Pirani and S.L. Connors and

C. Pean and S. Berger and N. Caud and Y. Chen and L. Goldfarb and M.I. Gomis and M. Huang and K. Leitzell and E. Lonnoy and J.B.R. Matthews and T.K. Maycock and T. Waterfield and O. Yelekci and R. Yu and B. Zhou (eds.), Cambridge University Press, Cambridge, United Kingdom and New York, NY, USA., doi:10.1017/9781009157896.001, 2021.

Jin, J., et al., Comparison of CMAM simulations of carbon monoxide (CO), nitrous oxide (N2O), and methane (CH4) with observations from Odin/SMR, ACE-FTS, and Aura/MLS, *Atmos. Chem. Phys.*, *9*(10), 3233–3252, 2009.

Joeckel, P., A. Kerkweg, A. Pozzer, R. Sander, H. Tost, H. Riede, A. Baumgaertner, S. Gromov, and B. Kern, Development cycle 2 of the Modular Earth Submodel System (MESSy2), *Geosci. Model Dev.*, *3*(2), 717–752, doi:10.5194/gmd-3-717-2010, 2010.

Jungclaus, J. H., et al., The ICON earth system model version 1.0, *J. Adv. Mod. Earth Sys.*, *14*(4), e2021MS002,813, doi:https://doi.org/10.1029/2021MS002813, 2022.

Kasahara, A., Various vertical coordinate systems used for numerical weather prediction, *Mon. Wea. Rev.*, *102*, 509–522, 1974.

Kern, B., and P. Jöckel, A diagnostic interface for the ICOsahedral Non-hydrostatic (ICON) modelling framework based on the Modular Earth Submodel System (MESSy v2.50), *Geosci. Model Dev.*, *9*(10), 3639–3654, doi:10.5194/gmd-9-3639-2016, 2016.

Konopka, P., J. U. Grooß, G. Günther, D. S. McKenna, R. Müller, J. W. Elkins, D. Fahey, and P. Popp, Weak impact of mixing on chlorine deactivation during SOLVE/THESEO2000: Lagrangian modeling (CLaMS) versus ER-2 in situ observations., *J. Geophys. Res.*, *108*, 8324, doi:10.1029/2001JD000876, 2003.

Konopka, P., et al., Mixing and ozone loss in the 1999-2000 Arctic vortex: Simulations with the 3-dimensional Chemical Lagrangian Model of the Stratosphere (CLaMS), *J. Geophys. Res.*, *109*, D02315, doi:10.1029/2003JD003792, 2004.

Konopka, P., et al., Ozone loss driven by nitrogen oxides and triggered by stratospheric

warmings may outweigh the effect of halogens, *J. Geophys. Res.*, *112*, D05105, doi: 10.1029/2006JD007064, 2007a.

Konopka, P., et al., Contribution of mixing to upward transport across the tropical tropopause layer (TTL), *Atmos. Chem. Phys.*, 7(12), 3285–3308, 2007b.

Korn, P., Formulation of an unstructured grid model for global ocean dynamics, *J. Comp. Phys.*, *339*, 525–552, doi:https://doi.org/10.1016/j.jcp.2017.03.009, 2017.

Lan, X., K. Thoning, and E. Dlugokencky, Trends in globally-averaged CH4, N2O, and SF6 determined from NOAA Global Monitoring Laboratory measurements, doi: https://doi.org/10.15138/P8XG-AA10, 2023.

Le Treut, H., R. Somerville, U. Cubasch, Y. Ding, C. Mauritzen, A. Mokssit, T. Peterson, and M. Prather, Historical Overview of Climate Change, in *Climate Change 2007: The Physical Science Basis. Contribution of Working Group I to the Fourth Assessment Report of the Intergovernmental Panel on Climate Change*, Solomon, S. and D. Qin and M. Manning and Z. Chen and M. Marquis and K.B. Averyt and M. Tignor and H.L. Miller (eds.), Cambridge University Press, Cambridge, United Kingdom and New York, NY, USA., 2007.

Leuenberger, D., M. Koller, O. Fuhrer, and C. Schär, A generalization of the SLEVE vertical coordinate, *Mon. Wea. Rev.*, *138*(9), 3683–3689, 2010.

Li, C., F. Zwiers, X. Zhang, G. Li, Y. Sun, and M. Wehner, Changes in annual extremes of daily temperature and precipitation in CMIP6 models, *J. Climate*, *34*(9), 3441–3460, doi: 10.1175/jcli-d-19-1013.1, 2021.

Livesey, N. J., et al., Version 4.2x level 2 data quality and description document, *JPL D-33509 Rev. C*, 2017.

Livesey, N. J., et al., Investigation and amelioration of long-term instrumental drifts in water vapor and nitrous oxide measurements from the Aura Microwave Limb Sounder (MLS) and their implications for studies of variability and trends, *Atmos. Chem. Phys.*, *21*(20), 15,409–15,430, 2021.

Lott, F., and M. J. Miller, A new subgrid-scale orographic drag parametrization: Its formulation and testing, *Q. J. R. Meteorol. Soc.*, *123*(537), 101–127, doi: https://doi.org/10.1002/qj.49712353704, 1997.

Mahowald, N. M., R. A. Plumb, P. J. Rasch, J. del Corral, and F. Sassi, Stratospheric transport in a three-dimensional isentropic coordinate model, *J. Geophys. Res.*, *107*(D15), 4254, doi: 10.1029/2001JD001313, 2002.

Marsh, D. R., M. J. Mills, D. E. Kinnison, J.-F. LAmarque, N. Calvo, and L. M. Polvani, Climate change from 1850 to 2005 simulated in CESM1(WACCM), *J. Climate*, *26*, 7372–7390, doi:10.1175/JCLI-D-12-00558.1, 2013.

McIntyre, M. E., On the Antarctic ozone hole, *J. Atmos. Terr. Phys.*, *51*, 29–43, 1989.

McIntyre, M. E., and T. N. Palmer, The 'surf zone' in the stratosphere, *J. Atmos. Terr. Phys.*, *46*, 825–849, 1984.

McKenna, D. S., J.-U. Grooß, G. Günther, P. Konopka, R. Müller, G. Carver, and Y. Sasano, A new Chemical Lagrangian Model of the Stratosphere (CLaMS): 2. Formulation of chemistry scheme and initialization, *J. Geophys. Res.*, *107*(D15), 4256, doi: 10.1029/2000JD000113, 2002a.

McKenna, D. S., P. Konopka, J.-U. Grooß, G. Günther, R. Müller, R. Spang, D. Offermann, and Y. Orsolini, A new Chemical Lagrangian Model of the Stratosphere (CLaMS): 1. Formulation of advection and mixing, *J. Geophys. Res.*, *107*(D16), 4309, doi: 10.1029/2000JD000114, 2002b.

Minschwaner, K., R. J. Salawitch, and M. B. McElroy, Absorption of solar radiation by O_2: Implications for O_3 and lifetimes of N_2O, $CFCl_3$, and CF_2Cl_2, *J. Geophys. Res.*, *98*, 10,543–10,561, 1993.

Minschwaner, K., L. Hoffmann, A. Brown, M. Riese, R. Müller, and P. F. Bernath, Stratospheric loss and atmospheric lifetimes of CFC-11 and CFC-12 derived from satellite observations, *Atmos. Chem. Phys.*, *13*(8), 4253–4263, doi:10.5194/acp-13-4253-2013, 2013.

Miyazaki, K., and I. Toshiki, The gradient genesis of stratospheric trace species in the subtropics and around the polar vortex, *J. Atmos. Sci.*, *65*, 490–508, 2008.

Mlawer, E. J., S. J. Taubman, P. D. Brown, M. J. Iacono, and S. A. Clough, Radiative transfer for inhomogeneous atmospheres: RRTM, a validated correlated-k model for the longwave, *J. Geophys. Res. A*, *102*(D14), 16,663–16,682, doi:https://doi.org/10.1029/97JD00237, 1997.

Morgenstern, O., et al., Review of the formulation of present-generation stratospheric chemistry-climate models and associated external forcings, *J. Geophys. Res.*, *115*, D00M02, doi:10.1029/2009JD013728, 2010.

Müller, R., The impact of the rise in atmospheric nitrous oxide on stratospheric ozone, *Ambio*, *50*, 1–5, doi:10.1007/s13280-020-01428-3, 2021.

Müller, R., J.-U. Grooß, A. M. Zafar, S. Robrecht, and R. Lehmann, The maintenance of elevated active chlorine levels in the Antarctic lower stratosphere through HCl null cycles, *Atmos. Chem. Phys.*, *18*(4), 2985–2997, doi:10.5194/acp-18-2985-2018, 2018.

Orr, A., P. Bechtold, J. Scinocca, M. Ern, and M. Janiskova, Improved middle atmosphere climate and forecasts in the ECMWF model through a nonorographic gravity wave drag parameterization, *J. Climate*, *23*, 5905–5926, doi:10.1175/2010JCLI3490.1, 2010.

Perić, M., R. Kessler, and G. Scheuerer, Comparison of finite-volume numerical methods with staggered and colocated grids, *Comp. a. Fluids*, *16*(4), 389–403, doi: https://doi.org/10.1016/0045-7930(88)90024-2, 1988.

Ploeger, F., P. Konopka, G. Günther, J.-U. Grooß, and R. Müller, Impact of the vertical velocity scheme on modeling transport across the tropical tropopause layer, *J. Geophys. Res.*, *115*, D03301, doi:10.1029/2009JD012023, 2010.

Ploeger, F., P. Konopka, R. Müller, G. Günther, J.-U. Grooß, C. Schiller, F. Ravegnani, A. Ulanovski, and M. Riese, Backtrajectory reconstruction of water vapour and ozone in-situ observations in the TTL, *Meteorol. Z.*, *21*(3), 239–244, 2012.

Ploeger, F., et al., Insight from ozone and water vapour on transport in the tropical tropopause layer (TTL), *Atmos. Chem. Phys.*, *11*, 407–419, doi:10.5194/acp-11-407-2011, 2011.

Ploeger, F., et al., A potential vorticity-based determination of the transport barrier in the Asian summer monsoon anticyclone, *Atmos. Chem. Phys.*, *15*(22), 13,145–13,159, doi: 10.5194/acp-15-13145-2015, 2015.

Ploeger, F., et al., How robust are stratospheric age of air trends from different reanalyses?, *Atmos. Chem. Phys.*, *19*, 6085–6105, doi:10.5194/gmd-12-2441-2019, 2019.

Ploeger, F., et al., The stratospheric brewer–dobson circulation inferred from age of air in the era5 reanalysis, *Atmos. Chem. Phys. Discuss.*, pp. 1–27, doi:10.5194/acp-2020-1253, 2021.

Plumb, R. A., A "tropical pipe" model of stratospheric transport, *J. Geophys. Res.*, *101*, 3957–3972, 1996.

Plumb, R. A., Stratospheric transport, *J. Meteorol. Soc. Jpn.*, *80*(4B), 793–809, 2002.

Plumb, R. A., Tracer interrelationships in the stratosphere, *Rev. Geophys.*, *45*, RG4005, doi: 10.1029/2005RG000179, 2007.

Pommrich, R., et al., Tropical troposphere to stratosphere transport of carbon monoxide and long-lived trace species in the Chemical Lagrangian Model of the Stratosphere (CLaMS), *Geosci. Model Dev.*, 7(6), 2895–2916, doi:10.5194/gmd-7-2895-2014, 2014.

Pozzer, A., P. Zimmermann, U. M. Doering, J. van Aardenne, H. Tost, F. Dentener, G. Janssens-Maenhout, and J. Lelieveld, Effects of business-as-usual anthropogenic emissions on air quality, *Atmos. Chem. Phys.*, *12*(15), 6915–6937, doi:10.5194/acp-12-6915-2012, 2012.

Prinn, R. G., et al., History of chemically and radiatively important atmospheric gases from the advanced global atmospheric gases experiment (agage), *Earth Sys. Sci. Data*, *10*(2), 985–1018, doi:10.5194/essd-10-985-2018, 2018.

Rauwoens, P., J. Vierendeels, and B. Merci, A solution for the odd–even decoupling problem

in pressure-correction algorithms for variable density flows, *J. Comp. Phys.*, *227*(1), 79–99, doi:https://doi.org/10.1016/j.jcp.2007.07.010, 2007.

Reick, C. H., et al., JSBACH3 - the land component of the MPI Earth System Model: documentation of version 3.2, *Tech. rep.*, MPI für Meteorologie, doi:https://doi.org/10.17617/2.3279802, 2021.

Reinert, D., The tracer transport module Part I: A mass consistent finite volume Approach with fractional steps, *Tech. rep.*, doi:10.5676/DWD_pub/nwv/icon_005, 2020.

Reinert, D., and G. Zängl, The tracer transport module Part II: Description and validation of the vertical transport operator, *Tech. rep.*, doi:10.5676/DWD_pub/nwv/icon_007, 2021.

Riese, M., F. Ploeger, A. Rap, B. Vogel, P. Konopka, M. Dameris, and P. Forster, Impact of uncertainties in atmospheric mixing on simulated UTLS composition and related radiative effects, *J. Geophys. Res.*, *117*, D16305, doi:10.1029/2012JD017751, 2012.

Roberts, M. J., et al., Description of the resolution hierarchy of the global coupled hadgem3-gc3.1 model as used in cmip6 highresmip experiments, *Geosci. Model Dev.*, *12*(12), 4999–5028, doi:10.5194/gmd-12-4999-2019, 2019.

Roeckner, E., et al., The atmospheric general circulation model ECHAM5 part I: Model description, *Report 349*, MPI für Meteorologie, Hamburg, 2003.

Rosanka, S., R. Sander, B. Franco, C. Wespes, A. Wahner, and D. Taraborrelli, Oxidation of low-molecular-weight organic compounds in cloud droplets: global impact on tropospheric oxidants, *Atmos. Chem. Phys.*, *21*(12), 9909–9930, doi:10.5194/acp-21-9909-2021, 2021.

Sander, R., et al., The community atmospheric chemistry box model caaba/mecca-4.0, *Geosci. Model Dev.*, *12*(4), 1365–1385, doi:https://doi.org/10.5194/gmd-12-1365-2019, 2019.

Sander, S. P., et al., *Evaluation No. 17, JPL Publication 10-6*, Chemical Kinetics and Photochemical Data for Use in Atmospheric Studies, Jet Propulsion Laboratory, Pasadena, 2011.

Satoh, M., T. Matsuno, H. Tomita, H. Miura, T. Nasuno, and S. Iga, Nonhydrostatic icosahedral atmospheric model (NICAM) for global cloud resolving simulations, *J. Comp. Phys.*, *227*(7), 3486–3514, 2008.

Seo, J., and W. Choi, Stratospheric polar vortex revisited: New diagnostic for the vortex breakup, *J Meteorol Soc Japan*, *100*(4), 687–705, doi:doi:10.2151/jmsj.2022-036, 2022.

Shepherd, T. G., Issues in stratosphere-troposphere coupling, *J Meteorol Soc Japan*, *80*(4B), 769–792, 2002.

Shepherd, T. G., Transport in the middle atmosphere, *J Meteorol Soc Japan*, *85B*, 165–191, 2007.

SPARC (Ed.), *SPARC report on the evaluation of chemistry-climate models*, SPARC Report No. 5, WCRP-132, WMO/TD-No. 1526, 2010.

Sparling, L. C., Statistical perspectives on stratospheric transport, *Rev. Geophys.*, *38*(4), 417–436, 2000.

Taylor, K. E., D. Williamson, and F. Zweiers, The sea surface temperature and sea ice concentration boundary conditions for AMIP II simulations. PCMDI Report 60. Program for Climate Model Diagnosis and Intercomparison, Lawrence Livermore National Laboratory, https://pcmdi.llnl.gov/report/pdf/60.pdf, 2000.

Thompson, R. L., et al., Transcom N2O model inter-comparison–part 1: Assessing the influence of transport and surface fluxes on tropospheric N2O variability, *Atmos. Chem. Phys.*, *14*(8), 4349–4368, doi:doi:10.5194/acp-14-4349-2014, 2014.

Thuburn, J., Horizontal discretizations: Some basic ideas, in *Numerical Techniques for Global Atmospheric Models*, edited by P. H. Lauritzen, C. Jablonowski, M. A. Taylor, and R. D. Nair, pp. 43–57, Springer, 2011.

Tilmes, S., et al., Representation of the community earth system model (cesm1) cam4-chem within the chemistry-climate model initiative (ccmi), *Geosci. Model Dev.*, *9*(5), 1853–1890, doi:10.5194/gmd-9-1853-2016, 2016.

Vogel, B., C. M. Volk, J. Wintel, V. Lauther, R. Müller, P. K. Patra, M. Riese, Y. Terao, and F. Stroh, Reconstructing high-resolution in-situ vertical carbon dioxide profiles in the sparsely monitored asian monsoon region, *Nat. Commun.*, *4*(1), 72, 2023.

Walters, D., et al., The Met Office Unified Model global atmosphere 4.0 and JULES global land 4.0 configurations, *Geosci. Model Dev.*, 7(1), 361–386, doi:10.5194/gmd-7-361-2014, 2014.

Wan, H., M. A. Giorgetta, G. Zängl, M. Restelli, K. F. D. Majewski and, L. Bonaventura and, D. Reinert, P. Rípodas, L. Kornblueh, and J. Förstner, The ICON-1.2 hydrostatic atmospheric dynamical core on triangular grids – Part 1: Formulation and performance of the baseline version, *Geosci. Model Dev.*, *6*, 735–763, doi:10.5194/gmd-6-735-2013, 2013.

Waters, J. W., et al., The Earth Observing System Microwave Limb Sounder (EOS MLS) on the Aura satellite, *IEEE Trans. Geosci. Remote Sens.*, *44*(5), 1106–1121, 2006.

Waugh, D. W., and L. M. Polvani, Stratospheric polar vortices, in *The Stratosphere: Dynamics, Transport, and Chemistry*, edited by L. M. Polvani, A. H. Sobel, and D. W. Waugh, pp. 43–57, American Geophysical Union, 2010.

Waugh, D. W., and W. J. Randel, Climatology of Arctic and Antarctic polar vortices using elliptical diagnostics, *J. Atmos. Sci.*, *56*, 1594–1613, 1999.

Waugh, D. W., W. J. Randel, S. Pawson, P. A. Newman, and E. R. Nash, Persistence of the lower stratospheric polar vortices, *J. Geophys. Res.*, *104*(D22), 27,191–27,201, 1999.

Waugh, D. W., A. H. Sobel, and L. M. Polvani, What is the polar vortex and how does it influence weather?, *Bull. Am. Meteorol. Soc.*, *98*(1), 37–44, doi:https://doi.org/10.1175/BAMS-D-15-00212.1, 2017.

Wehner, M., P. Gleckler, and J. Lee, Characterization of long period return values of extreme daily temperature and precipitation in the CMIP6 models: Part 1, model evaluation, *Wea. and Clim. Extr.*, *30*, 100,283, doi:10.1016/j.wace.2020.100283., 2020.

Williamson, D. L., Time-split versus process-split coupling of parameterizations and dynamical core, *Mon. Wea. Rev.*, *130*(8), 2024–2041, doi:https://doi.org/10.1175/1520-0493(2002)130<2024:TSVPSC>2.0.CO;2, 2002.

WMO, *The Stratosphere 1981 theory and measurements*, WMO global ozone research and monitoring report No. 11, 1982.

Zängl, G., D. Reinert, P. Rípodas, and M. Baldauf, The ICON (ICOsahedral Non-hydrostatic) modelling framework of DWD and MPI-M: Description of the non-hydrostatic dynamical core, *Q.J.R. Meteorol. Sc.*, *141*, 563 – 579, doi:10.1002/qj.2378, 2015.

List of Figures

List of Abbreviations

ACM Atmospheric Circulation Model

AGAGE Advanced Global Atmospheric Gases Experiment

AMIP Atmospheric Model Intercomparison Project

BDC Brewer-Dobson Circulation

CCM Chemistry Climate Model

CHANNEL Channel MESSy submodel

CLaMS Chemical Lagrangian Model of the Stratosphere

CLOUDOPT Cloud Optical Properties MESSy submodel

COSMO Consortium for Small-scale Modeling

CTM Chemistry Transport Model

DISSOC Dissociation MESSy submodel

DJF December, January and February

DWD Deutscher Wetterdienst

ECHAM ECMWF Hamburg

EMAC ECHAM/MESSy Atmospheric Chemistry

EOS Earth Observing System

ERA European Reanalysis

ESM Earth System Model

GCM General Circulation Model

GRAGG Grid Aggregation

HAMOCC Hamburg Ocean Carbon Cycle model

HR high resolution

ICON Icosahedral nonhydrostatic modeling framework

IFS Integrated Forecasting System

IPCC Intergovernmental Panel on Climate Change

JJA June, July and August

LR low resolution

MAM March, April and May

MESSy Modular Earth Submodel System

MLS Microwave Limb Sounder

MPI Max Planck Institut

NH Northern Hemisphere

NOAA National Oceanic and Atmospheric Administration

NWP Numerical Weather Prediction

PDF Probability density function

RRTM Rapid Radiative Transfer Model

SH Southern Hemisphere

SLEVE Smooth Level Vertical

SON September, October and November

SPARC Stratosphere-troposphere Processes And their Role in Climate

TTL Tropical Tropopause layer

UTLS Upper Troposhere Lower Stratosphere

WACCM Whole Atmosphere Community Climate Model

WMO World Meteorological Organization

H_2O Water (Vapor)

N_2O Nitrous Oxide

CH_4 Methane

CO_2 Carbon Dioxide

CO Carbon Monoxide

O_3 Ozone

CCl_3F CFC-11 or Trichlorofluoromethane

CCl_2F_2 CFC-12 or Dichlorodifluoromethane

OH Hydroxyl Radical

NO Nitric Oxide

Appendix A

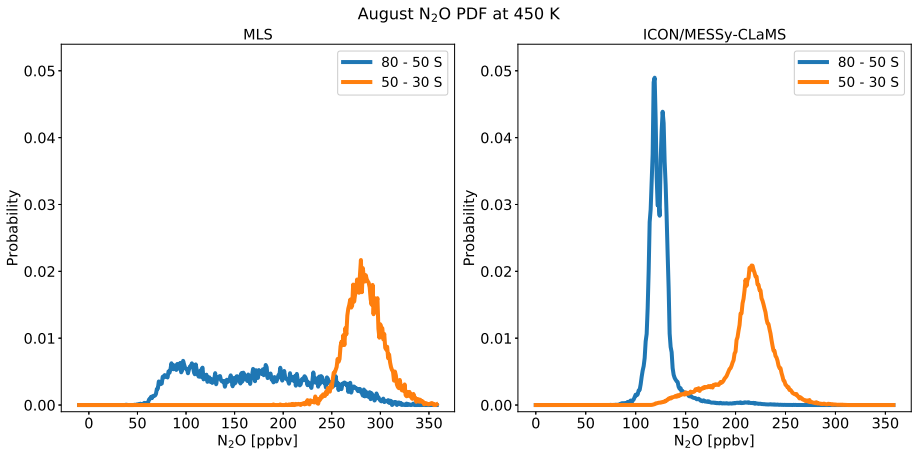

Figure 1: PDF of N_2O versus latitude in 80 to 50 degrees South in blue. PDF in 50 to 30 degrees South in orange. MLS (left panel). ICON/MESSy-CLaMS (right panel): August at potential temperature of 450 K.

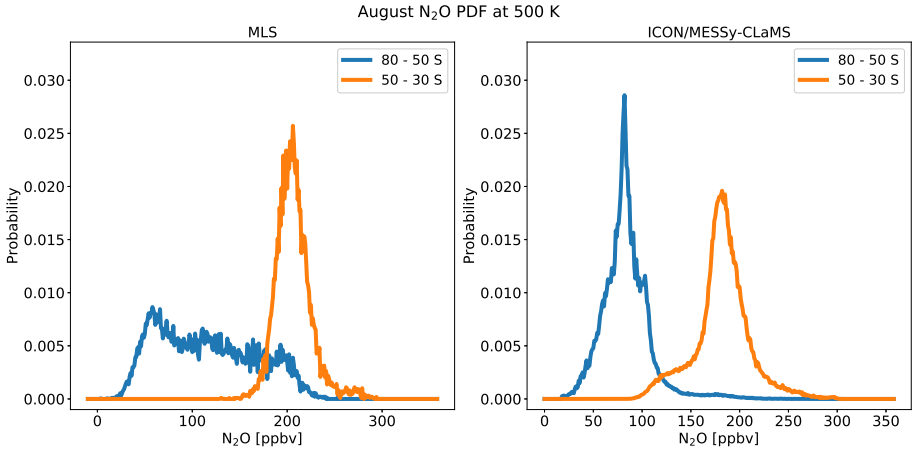

Figure 2: PDF of N_2O versus latitude in 80 to 50 degrees South in blue. PDF in 50 to 30 degrees South in orange. MLS (left panel). ICON/MESSy-CLaMS (right panel): August at potential temperature of 500 K.

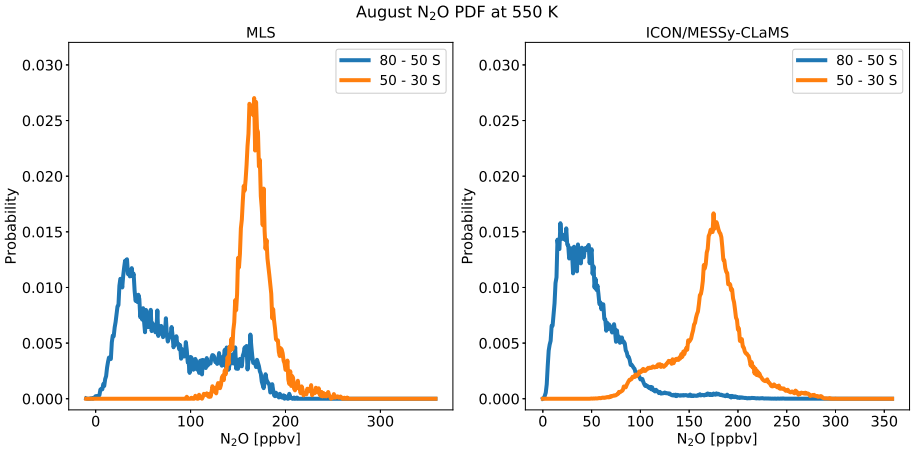

Figure 3: PDF of N_2O versus latitude in 80 to 50 degrees South in blue. PDF in 50 to 30 degrees South in orange. MLS (left panel). ICON/MESSy-CLaMS (right panel): August at potential temperature of 550 K.

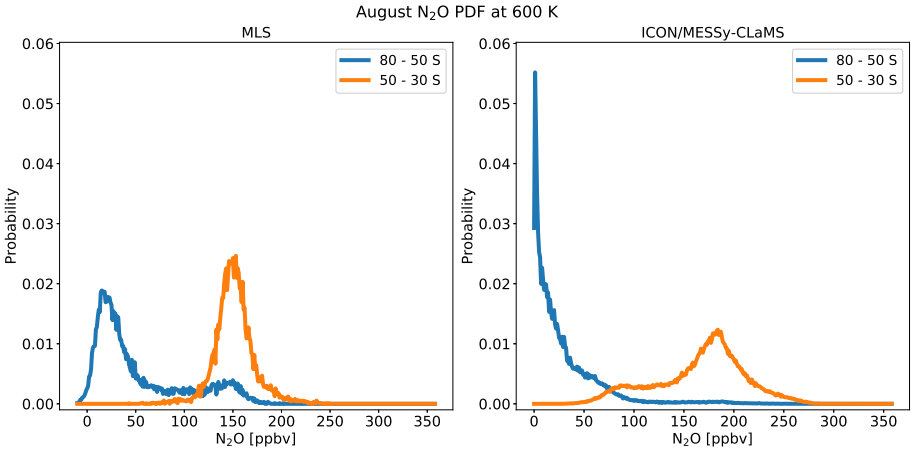

Figure 4: PDF of N_2O versus latitude in 80 to 50 degrees South in blue. PDF in 50 to 30 degrees South in orange. MLS (left panel). ICON/MESSy-CLaMS (right panel): August at potential temperature of 600 K.

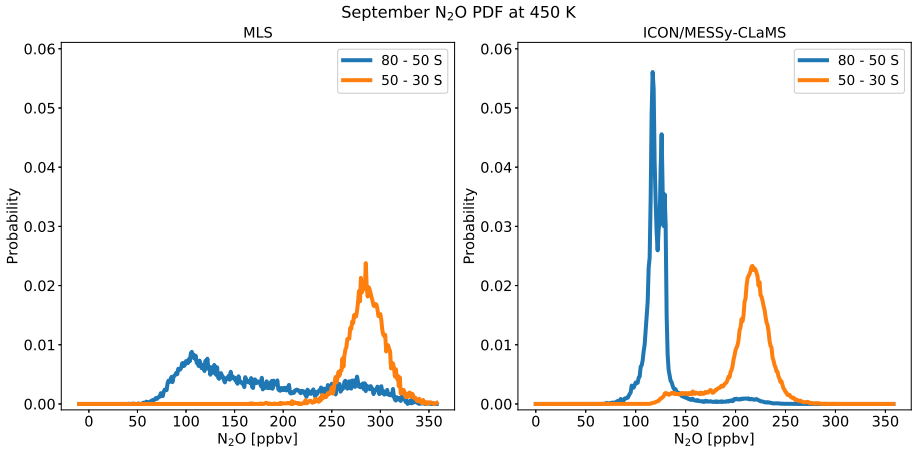

Figure 5: PDF of N_2O versus latitude in 80 to 50 degrees South in blue. PDF in 50 to 30 degrees South in orange. MLS (left panel). ICON/MESSy-CLaMS (right panel): September at potential temperature of 450 K.

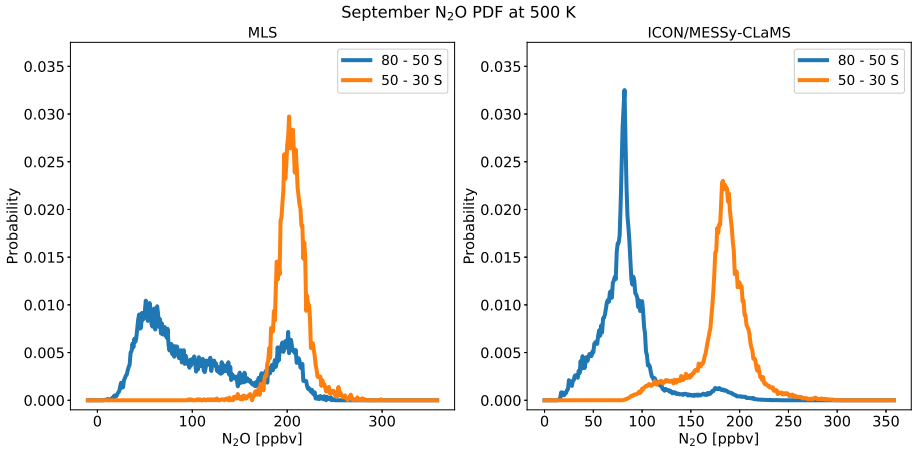

Figure 6: PDF of N_2O versus latitude in 80 to 50 degrees South in blue. PDF in 50 to 30 degrees South in orange. MLS (left panel). ICON/MESSy-CLaMS (right panel): September at potential temperature of 500 K.

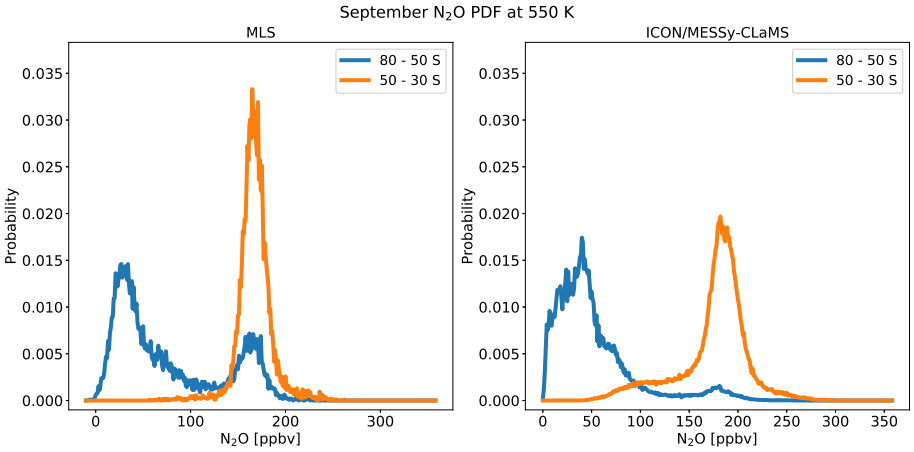

Figure 7: PDF of N_2O versus latitude in 80 to 50 degrees South in blue. PDF in 50 to 30 degrees South in orange. MLS (left panel). ICON/MESSy-CLaMS (right panel): September at potential temperature of 550 K.

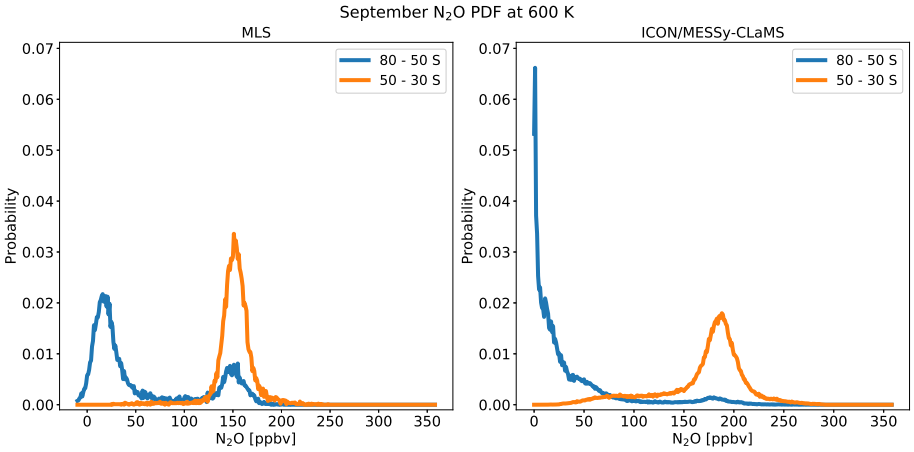

Figure 8: PDF of N_2O versus latitude in 80 to 50 degrees South in blue. PDF in 50 to 30 degrees South in orange. MLS (left panel). ICON/MESSy-CLaMS (right panel): September at potential temperature of 600 K.

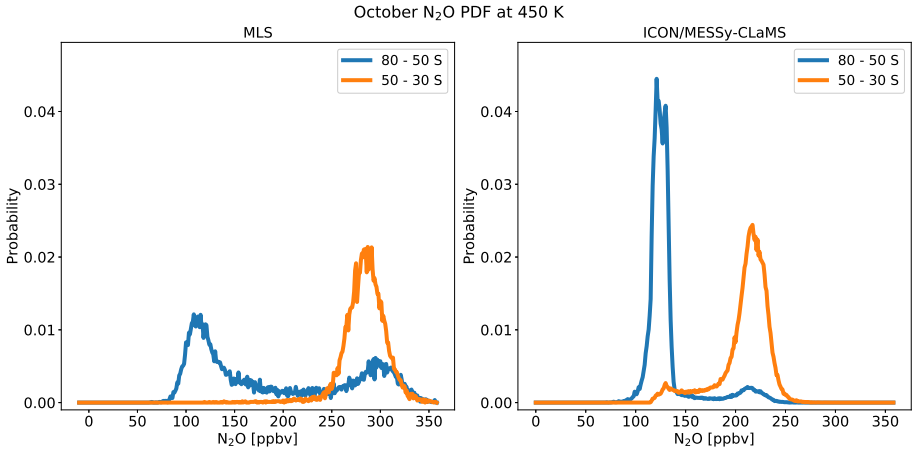

Figure 9: PDF of N_2O versus latitude in 80 to 50 degrees South in blue. PDF in 50 to 30 degrees South in orange. MLS (left panel). ICON/MESSy-CLaMS (right panel): October at potential temperature of 450 K.

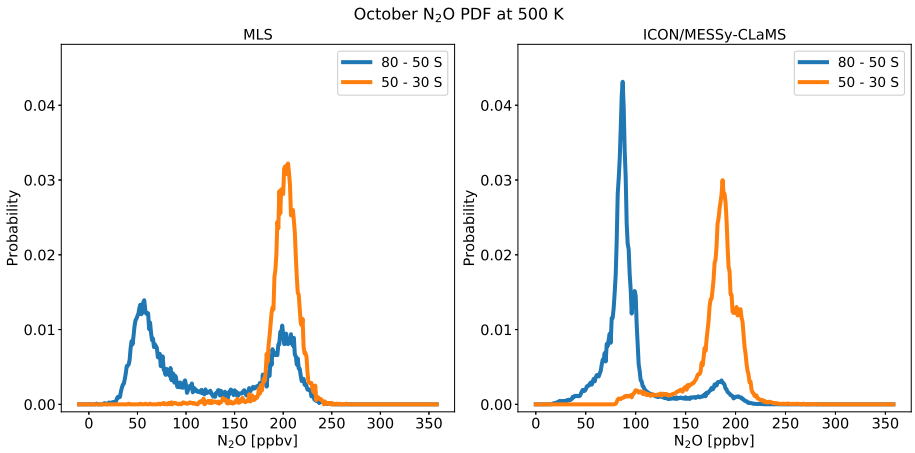

Figure 10: PDF of N_2O versus latitude in 80 to 50 degrees South in blue. PDF in 50 to 30 degrees South in orange. MLS (left panel). ICON/MESSy-CLaMS (right panel): October at potential temperature of 500 K.

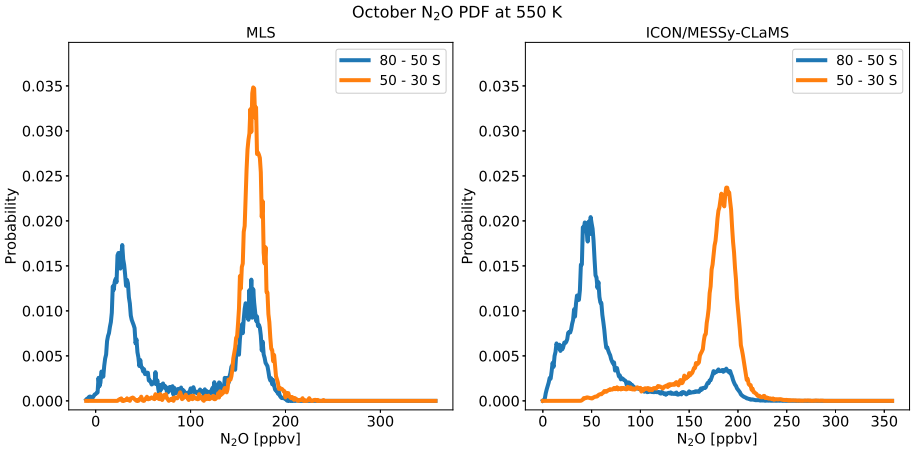

Figure 11: PDF of N_2O versus latitude in 80 to 50 degrees South in blue. PDF in 50 to 30 degrees South in orange. MLS (left panel). ICON/MESSy-CLaMS (right panel): October at potential temperature of 550 K.

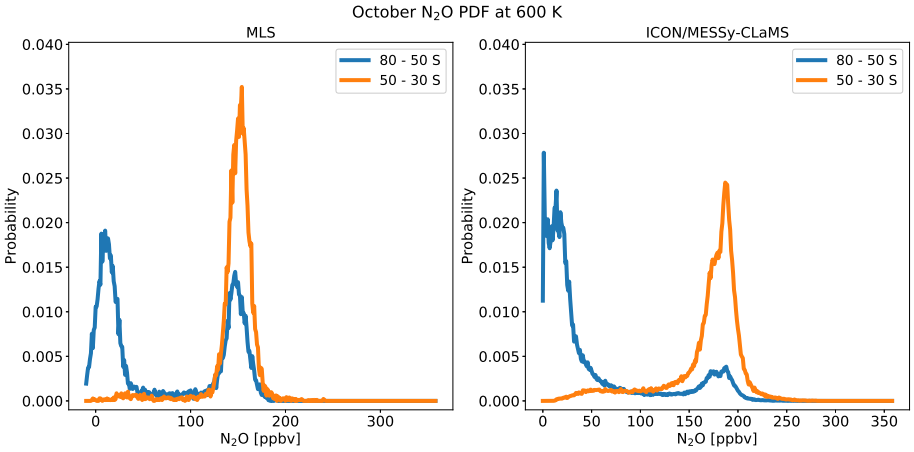

Figure 12: PDF of N_2O versus latitude in 80 to 50 degrees South in blue. PDF in 50 to 30 degrees South in orange. MLS (left panel). ICON/MESSy-CLaMS (right panel): October at potential temperature of 600 K.

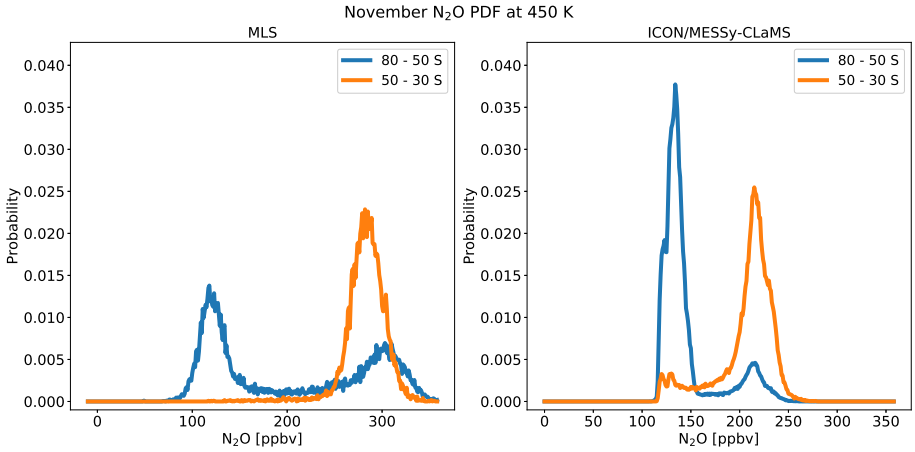

Figure 13: PDF of N_2O versus latitude in 80 to 50 degrees South in blue. PDF in 50 to 30 degrees South in orange. MLS (left panel). ICON/MESSy-CLaMS (right panel): November at potential temperature of 450 K.

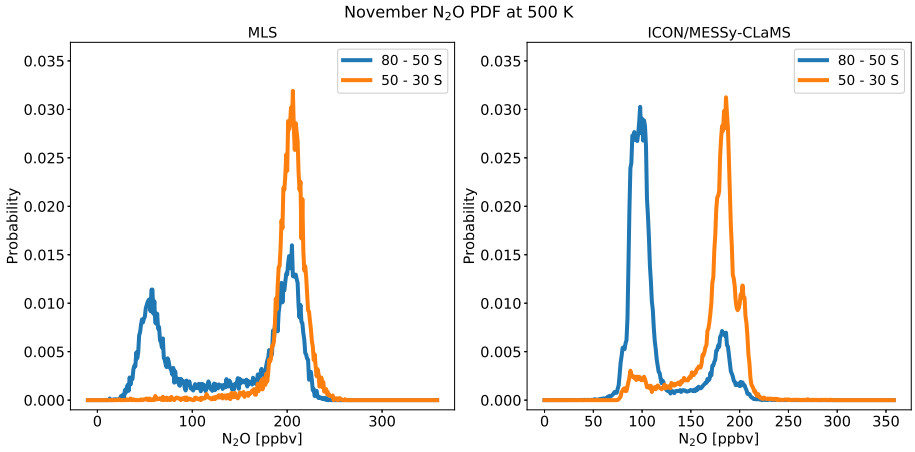

Figure 14: PDF of N_2O versus latitude in 80 to 50 degrees South in blue. PDF in 50 to 30 degrees South in orange. MLS (left panel). ICON/MESSy-CLaMS (right panel): November at potential temperature of 500 K.

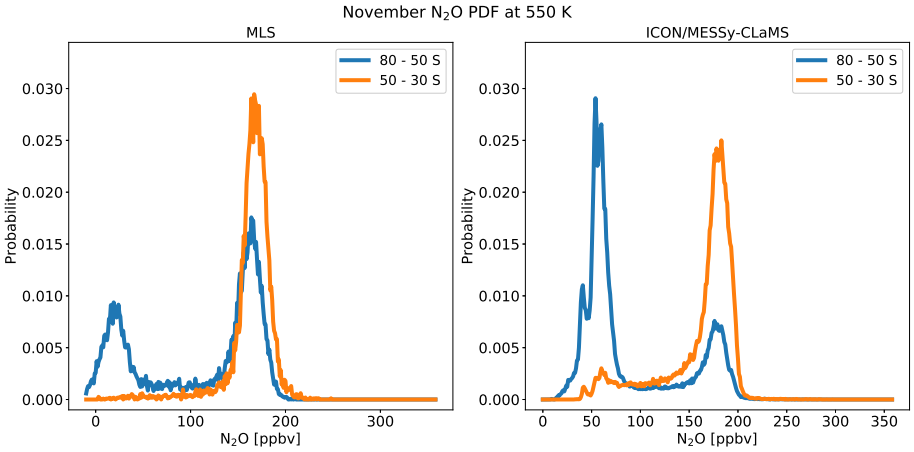

Figure 15: PDF of N_2O versus latitude in 80 to 50 degrees South in blue. PDF in 50 to 30 degrees South in orange. MLS (left panel). ICON/MESSy-CLaMS (right panel): November at potential temperature of 550 K.

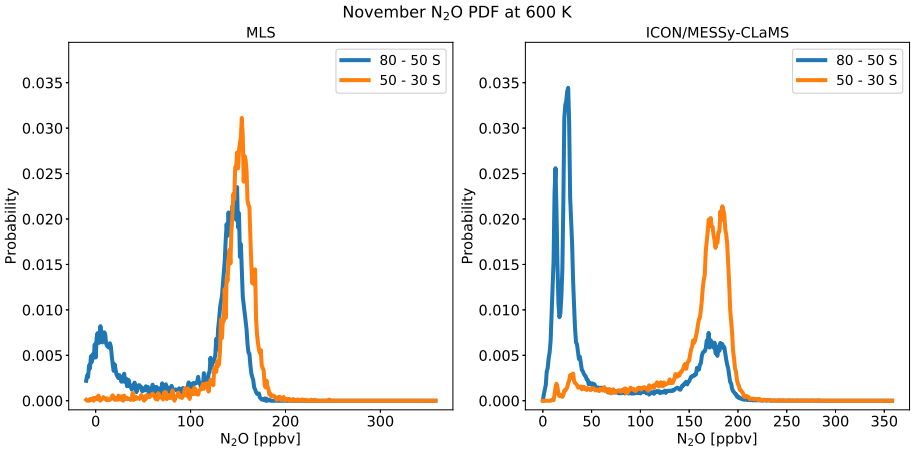

Figure 16: PDF of N_2O versus latitude in 80 to 50 degrees South in blue. PDF in 50 to 30 degrees South in orange. MLS (left panel). ICON/MESSy-CLaMS (right panel): November at potential temperature of 600 K.

Appendix B

First Law of Thermodynamics

$$dq = du + dw \tag{1}$$

First law of thermodynamics (for unit mass): energy supply in form of heat q to air parcel causes internal energy u increase or expansion work w. If we are dealing with a unit mass of a substance, the volume V can be replaced by specific volume α and the work differential can be written as $dw = pd\alpha$. Applying Joules law for an ideal gas u depends only on temperature ($du = C_v dT$). Alternative form of first law of thermodynamics:

$$dq = C_v dT + pd\alpha \tag{2}$$

Consider the Ideal gas law with the definition of the specific volume $1/\alpha = \rho$

$$p = \rho RT \quad \text{or} \quad p\alpha = RT \tag{3}$$

$$d(p\alpha) = pd\alpha + \alpha dp = RdT \tag{4}$$

$$pd\alpha = RdT - \alpha dp \tag{5}$$

Rewrite using 5 above and $C_p = C_v + R$ results in the first law of thermodynamics in an alternative form:

$$dq = C_p dT - \alpha dp \tag{6}$$

How is the First law of thermodynamics related to temperature tendencies? Consider the first law of thermodynamics (6) and write the heat differential as diabatic heating rate J,

$dq = Jdt$:

$$dq = C_p dT - \alpha dp \tag{7}$$

$$Jdt = C_p dT - \alpha dp \tag{8}$$

Divide by dt

$$J = C_p \frac{dT}{dt} - \alpha \frac{dp}{dt} \tag{9}$$

reorder

$$C_p \frac{dT}{dt} = \alpha \frac{dp}{dt} + J \tag{10}$$

Substitute α by ideal gas law and divide by C_p

$$\frac{dT}{dt} = \frac{R}{C_p} \frac{T}{p} \frac{dp}{dt} + \frac{J}{C_p} \tag{11}$$

This is the thermodynamic energy equation. The total temperature tendency consists of two terms. First term on the right hand side contains dynamical temperature tendencies and the second term consists of diabatic heating temperature tendencies.

Thermodynamic energy equation with different vertical coordinate Consider a set of coordinates with a generalized vertical coordinate s introduced by *Kasahara* (1974). The full derivative with respect to time for the vertical coordinate s reads:

$$\frac{d}{dt} = \left(\frac{\partial}{\partial t}\right)_s + \vec{v}\nabla_s + \frac{ds}{dt}\frac{\partial}{\partial s} \tag{12}$$

Note that the suffix with parentheses $(\cdot)_s$ denotes the chosen vertical coordinate system. With **pressure** as generalized **vertical coordinate** $s = p$ the thermodynamic energy equation (11) reads

$$\left(\frac{\partial T}{\partial t}\right)_p + \vec{v}\nabla_p T + \frac{dp}{dt}\frac{\partial T}{\partial p} = \frac{R}{C_p}\frac{T}{p}\frac{dp}{dt} + \frac{J}{C_p} \tag{13}$$

or

$$\left(\frac{\partial T}{\partial t}\right)_p = -\vec{v}\nabla_p T - \frac{dp}{dt}\frac{\partial T}{\partial p} + \frac{R}{C_p}\frac{T}{p}\frac{dp}{dt} + \frac{J}{C_p} \tag{14}$$

Now, we consider the thermodynamic energy equation (11) with **geometrical height** as generalized **vertical coordinate** $s = z$

$$\left(\frac{\partial T}{\partial t}\right)_z + \vec{v}\nabla_z T + \frac{dz}{dt}\frac{\partial T}{\partial z} = \frac{R}{C_p}\frac{T}{p}\frac{dp}{dt} + \frac{J}{C_p} \tag{15}$$

$$\left(\frac{\partial T}{\partial t}\right)_z = -\vec{v}\nabla_z T - \frac{dz}{dt}\frac{\partial T}{\partial z} + \frac{R}{C_p}\frac{T}{p}\frac{dp}{dt} + \frac{J}{C_p} \tag{16}$$

$$\left(\frac{\partial T}{\partial t}\right)_z = -\vec{v}\nabla_z T + \left[\frac{R}{C_p}\frac{T}{p}\frac{dp}{dt} - \frac{dz}{dt}\frac{\partial T}{\partial z}\right] + \frac{J}{C_p} \tag{17}$$

Replace total derivative of dp/dt in z coordinates. For orientation in [] brackets:

$$\left(\frac{\partial T}{\partial t}\right)_z = -\vec{v}\nabla_z T + \frac{R}{C_p}\frac{T}{p}\left[\frac{dp}{dt}\right] - \frac{dz}{dt}\frac{\partial T}{\partial z} + \frac{J}{C_p} \tag{18}$$

$$\left(\frac{\partial T}{\partial t}\right)_z = -\vec{v}\nabla_z T + \frac{R}{C_p}\frac{T}{p}\left[\left(\frac{\partial p}{\partial t}\right)_z + \vec{v}\nabla_z p + \frac{dz}{dt}\frac{\partial p}{\partial z}\right] - \frac{dz}{dt}\frac{\partial T}{\partial z} + \frac{J}{C_p} \tag{19}$$

Multiply brackets with factor

$$\left(\frac{\partial T}{\partial t}\right)_z = -\vec{v}\nabla_z T + \left[\frac{R}{C_p}\frac{T}{p}\left(\frac{\partial p}{\partial t}\right)_z + \frac{R}{C_p}\frac{T}{p}\vec{v}\nabla_z p + \frac{R}{C_p}\frac{T}{p}\frac{dz}{dt}\frac{\partial p}{\partial z}\right] - \frac{dz}{dt}\frac{\partial T}{\partial z} + \frac{J}{C_p} \tag{20}$$

Digression Rewrite pressure with ideal gas law to temperature.

$$\vec{v}\nabla_z p = \vec{v}\nabla_z(\rho R T) = (\rho R)\,\vec{v}\nabla_z T \tag{2.h1}$$

$$\frac{RT}{C_p p}(\rho R) = \frac{RT}{C_p p}\left(\frac{p}{T}\right) = \frac{R}{C_p} \tag{2.h2}$$

$$\frac{RT}{C_p p}\vec{v}\nabla_z p = \frac{R}{C_p}\vec{v}\nabla_z T \tag{2.h3}$$

$$\frac{R}{C_p} - 1 = \frac{R - C_p}{C_p} = \frac{(C_p - C_V) - C_p}{C_p} = \frac{-C_V}{C_p} \tag{2.h4}$$

Continue with (20). Terms ordered

$$\left(\frac{\partial T}{\partial t}\right)_z = -\vec{v}\nabla_z T + \frac{R}{C_p}\frac{T}{p}\vec{v}\nabla_z p + \frac{R}{C_p}\frac{T}{p}\left(\frac{\partial p}{\partial t}\right)_z + \frac{R}{C_p}\frac{T}{p}\frac{dz}{dt}\frac{\partial p}{\partial z} - \frac{dz}{dt}\frac{\partial T}{\partial z} + \frac{J}{C_p} \tag{21}$$

Use 2.h3

$$\left(\frac{\partial T}{\partial t}\right)_z = \left(\frac{R}{C_p} - 1\right)\vec{v}\nabla_z T + \frac{R}{C_p}\frac{T}{p}\left(\frac{\partial p}{\partial t}\right)_z + \left[\frac{R}{C_p}\frac{T}{p}\frac{dz}{dt}\frac{\partial p}{\partial z} - \frac{dz}{dt}\frac{\partial T}{\partial z}\right] + \frac{J}{C_p} \tag{22}$$

Use 2.h4

$$\left(\frac{\partial T}{\partial t}\right)_z = \frac{-C_V}{C_p}\vec{v}\nabla_z T + \frac{R}{C_p}\frac{T}{p}\left(\frac{\partial p}{\partial t}\right)_z + \left[\frac{R}{C_p}\frac{T}{p}\frac{dz}{dt}\frac{\partial p}{\partial z} - \frac{dz}{dt}\frac{\partial T}{\partial z}\right] + \frac{J}{C_p} \tag{23}$$

Rewrite partial differentiation term $\frac{\partial p}{\partial z}$ in [] with the ideal gas law the same way as it was outlined in the digression for ∇ term

$$\left(\frac{\partial T}{\partial t}\right)_z = \frac{-C_V}{C_p}\vec{v}\nabla_z T + \frac{R}{C_p}\frac{T}{p}\left(\frac{\partial p}{\partial t}\right)_z + \left[\frac{R}{C_p}\frac{T}{p}\frac{dz}{dt}\frac{\partial(\rho RT)}{\partial z} - \frac{dz}{dt}\frac{\partial T}{\partial z}\right] + \frac{J}{C_p} \tag{24}$$

$$\left(\frac{\partial T}{\partial t}\right)_z = \frac{-C_V}{C_p}\vec{v}\nabla_z T + \frac{R}{C_p}\frac{T}{p}\left(\frac{\partial p}{\partial t}\right)_z + \left[\frac{R}{C_p}\frac{T}{p}\rho R\frac{dz}{dt}\frac{\partial(T)}{\partial z} - \frac{dz}{dt}\frac{\partial T}{\partial z}\right] + \frac{J}{C_p} \tag{25}$$

$$\left(\frac{\partial T}{\partial t}\right)_z = \frac{-C_V}{C_p}\vec{v}\nabla_z T + \frac{R}{C_p}\frac{T}{p}\left(\frac{\partial p}{\partial t}\right)_z + \left[\left(\frac{R}{C_p}\frac{T}{p}\rho R - 1\right)\frac{dz}{dt}\frac{\partial T}{\partial z}\right] + \frac{J}{C_p} \tag{26}$$

Use 2.h2 and 2.h4 to obtain the thermodynamic energy equation in geometrical height vertical coordinate form:

$$\left(\frac{\partial T}{\partial t}\right)_z = -\frac{C_V}{C_p}\vec{v}\nabla_z T + \frac{R}{C_p}\frac{T}{p}\left(\frac{\partial p}{\partial t}\right)_z - \frac{C_V}{C_p}\frac{dz}{dt}\frac{\partial T}{\partial z} + \frac{J}{C_p} \tag{27}$$

Compare thermodynamic energy equation with pressure as the vertical coordinate

$$\left(\frac{\partial T}{\partial t}\right)_p = -\vec{v}\nabla_p T + \frac{dp}{dt}\frac{R}{C_p}\frac{T}{p} - \frac{dp}{dt}\frac{\partial T}{\partial p} + \frac{J}{C_p} \tag{28}$$

Both equations (27 and 28) consists of terms for: horizontal advection + adiabatic compression - vertical advection + diabatic heating. Independent of the chosen vertical coordinate system, the source term for diabatic temperature tendencies is for both coordinates:

$$\left[\left(\frac{\partial T}{\partial t}\right)_p\right]_{diabatic} = \frac{J}{C_p} \tag{29}$$

The author concludes that the diabatic temperature tendencies is invariant of the chosen vertical coordinate system of the general circulation model. T

$$\left[\left(\frac{\partial T}{\partial t}\right)_z\right]_{diabatic} = \frac{J}{C_p} \tag{30}$$

Derivation of $\dot{\Theta}$ with First law of thermodynamics and definition of Θ In the following the vertical velocity equation for potential temperature is derived with the first law of thermodynamics without a specific vertical coordinate chosen. Consider the first law of thermodynamics (8) and order terms

$$C_p dT - \alpha dp = J dt \tag{31}$$

replace α by ideal gas law

$$C_p dT - R\frac{T}{p} dp = J dt \tag{32}$$

divide by dt

$$C_p \frac{dT}{dt} - R\frac{T}{p}\frac{dp}{dt} = J \tag{33}$$

divide by temperature

$$\frac{C_p}{T}\frac{dT}{dt} - \frac{R}{p}\frac{dp}{dt} = \frac{1}{T}J \tag{34}$$

reform with derivative of logarithm

$$C_p \frac{d\ln(T)}{dt} - R\frac{d\ln(p)}{dt} = \frac{1}{T}J \tag{35}$$

Consider the definition of the potential temperature Θ

$$\Theta = T\left(\frac{p_s}{p}\right)^{R/c_p} \tag{36}$$

Take the logarithm of the equation (36) and use logarithmic identities:

$$C_p \ln(\Theta) = C_p \ln(T) - R\ln(p) + R\ln(p_s) \tag{37}$$

total derivative w.r.t. time and rearrange order

$$C_p \frac{d \ln(T)}{dt} - R \frac{d \ln(p)}{dt} = C_p \frac{d \ln(\Theta)}{dt} \tag{38}$$

Compare equations (35) and (38):

$$C_p \frac{d \ln(\Theta)}{dt} = \frac{1}{T} J \tag{39}$$

Rearranging terms and derivative of logarithm and we obtain $\dot{\Theta}$ without any assumption on the coordinate system. $\frac{1}{C_p}$ is part of the equation due to the form of the first law of thermodynamics.

$$\frac{d(\Theta)}{dt} = \dot{\Theta} = \frac{\Theta}{T} \frac{J}{C_p} \tag{40}$$

We conclude that for $\dot{\Theta}$ only the diabatic heating rate $\frac{J}{C_p}$ is the only relevant component left from the original first law of thermodynamics.

How is $\dot{\Theta}$ related to temperature tendencies? The following section is relevant in the physics package of the general circulation model and only indirect affecting the dynamics due to forcing. Consider the definition of specific heat at constant pressure and at constant volume:

$$C_i = \left(\frac{dq}{dT} \right)_{i=const.} , \tag{41}$$

with i = p, V

$$(dq = C_i dT)_{i=const.} \tag{42}$$

$$(Jdt = C_i dT)_{i=const.} \tag{43}$$

Divide by dt

$$\left(J = C_i \frac{dT}{dt} \right)_{i=const.} \tag{44}$$

For diabatic processes temperature tendencies are equal to $\frac{J}{C_i}$ assuming constant pressure or constant volume, respectively.

$$\frac{J}{C_i} = \left[\left(\frac{dT}{dt}\right)_{i=const.}\right]_{diabatic} \tag{45}$$

As it was stated above diabatic heating is contributing to $\dot{\Theta}$. Temperature tendencies stated below in [] only include diabatic heating temperature tendencies. Insert in (40)

$$\dot{\Theta} = \frac{\Theta}{T}\frac{J}{C_p} \tag{46}$$

$$\dot{\Theta} = \frac{1}{C_p}\frac{\Theta}{T}\frac{C_i}{C_i}J \tag{47}$$

$$\dot{\Theta} = \frac{C_i}{C_p}\frac{\Theta}{T}\frac{J}{C_i} \tag{48}$$

Case $i = p$

$$\dot{\Theta} = \frac{C_p}{C_p}\frac{\Theta}{T}\frac{J}{C_p} \tag{49}$$

Insert (45)

$$\dot{\Theta} = \frac{\Theta}{T}\left[\left(\frac{dT}{dt}\right)_{p=const.}\right]_{diabatic} \tag{50}$$

Case $i = V$

$$\dot{\Theta} = \frac{C_V}{C_p}\frac{\Theta}{T}\frac{J}{C_V} \tag{51}$$

Insert (45)

$$\dot{\Theta} = \frac{C_V}{C_p}\frac{\Theta}{T}\left[\left(\frac{dT}{dt}\right)_{V=const.}\right]_{diabatic} \tag{52}$$

Acknowledgments

Many people have contributed to this work in various ways, and I am grateful for their support. I am thankful for their scientific and personal guidance throughout this thesis. Above all, I would like to express my gratitude to PD Dr. Rolf Müller and Dr. Jens-Uwe Grooß for providing me with the opportunity to write my dissertation in such an interesting subject. The Forschungszentrum Jülich at the Institute of Energy and Climate - Stratosphere (IEK-7) provided professional support and valuable advice, contributing significantly to the success of this thesis. I am grateful to Prof. Dr. Martin Riese for accepting me into the institute, enabling me to gain valuable experience during my time at Jülich. I would also like to thank Prof. Dr. Michael Volk for supervising this thesis at the University of Wuppertal. Additionally, I would like to say a warming thank you to my colleagues at IEK-7, who are an shining example of how great team spirit and good working environment can be exemplified. The colleagues at the JSC Simulation and Data Lab - Climate Science, under the direction of Dr. Lars Hofmann, are not inferior to the colleagues at IEK-7 in this matter. And I would like to thank them just as much for the great time and scientific discussions.